SANDIA REPORT

SAND2005-6833
Unlimited Release
Printed November 2005

Hydrogen Storage in Sodium Aluminum Hydride

E.H. Majzoub, V. Ozolins, K. F. McCarty, R. S. Stumpf, J. L. Herberg, and R. S. Maxwell

Prepared by
Sandia National Laboratories
Albuquerque, New Mexico 87185 and Livermore, California 94550

Sandia is a multiprogram laboratory operated by Sandia Corporation,
a Lockheed Martin Company, for the United States Department of Energy's
National Nuclear Security Administration under Contract DE-AC04-94-AL85000.

Sandia National Laboratories

Issued by Sandia National Laboratories, operated for the United States Department of Energy by Sandia Corporation.

Available to DOE and DOE contractors from
U.S. Department of Energy
Office of Scientific and Technical Information
P.O. Box 62
Oak Ridge, TN 37831

Telephone: (865) 576-8401
Facsimile: (865) 576-5728
E-Mail: reports@adonis.osti.gov
Online ordering: http://www.doe.gov/bridge

Available to the public from
U.S. Department of Commerce
National Technical Information Service
5285 Port Royal Rd
Springfield, VA 22161

Telephone: (800) 553-6847
Facsimile: (703) 605-6900
E-Mail: orders@ntis.fedworld.gov
Online order: http://www.ntis.gov/help/ordermethods.asp?loc=7-4-0#online

SAND2005-6833
Unlimited Release
Printed November 2005

Hydrogen Storage in Sodium Aluminum Hydride

E. H. Majzoub[1], and V. Ozolins[2], and K. F. McCarty, and
R. S. Stumpf
Analytical Materials Science Department
Sandia National Laboratories
Livermore, CA 94551-9403

J. L. Herberg, and R. S. Maxwell
Lawrence Livermore National Laboratories
Livermore, CA 94551

ABSTRACT

Sodium aluminum hydride, $NaAlH_4$, has been studied for use as a hydrogen storage material. The effect of Ti, as a few mol. % dopant in the system to increase kinetics of hydrogen sorption, is studied with respect to changes in lattice structure of the crystal. No Ti substitution is found in the crystal lattice. Electronic structure calculations indicate that the $NaAlH_4$ and Na_3AlH_6 structures are complex-ionic hydrides with Na^+ cations and AlH_4^- and AlH_6^{3-} anions, respectively. Compound formation studies indicate the primary Ti-compound formed when doping the material at 33 at. % is $TiAl_3$, and likely Ti-Al compounds at lower doping rates. A general study of sorption kinetics of $NaAlH_4$, when doped with a variety of Ti-halide compounds, indicates a uniform response with the kinetics similar for all dopants. NMR multiple quantum studies of solution-doped samples indicate solvent interaction with the doped alanate. Raman spectroscopy was used to study the lattice dynamics of $NaAlH_4$, and illustrated the molecular ionic nature of the lattice as a separation of vibrational modes between the AlH_4^- anion-modes and lattice-modes. In-situ Raman measurements indicate a stable AlH_4^- anion that is stable at the melting temperature of $NaAlH_4$, indicating that Ti-dopants must affect the Al-H bond strength.

[1]Corresponding author. Electronic-mail: ehmajzo@sandia.gov
[2]Now at University of California, Los Angeles, Department of Materials Science and Engineering. Los Angeles, CA 90095-1595.

Acknowledgements

This work was funded by the U.S. Department of Energy, Office of Energy Efficiency and Renewable Energy, in the Hydrogen, Fuel Cells & Infrastructure Technologies Program under contract No. DE-AC36-83CH10093, and Sandia National Laboratories through the Laboratory Directed Research and Development program. NMR work was performed under the auspices of the U.S. Department of Energy by University of California, Lawrence Livermore National Laboratory under Contract W-7405-Eng-48.

Executive Summary

Sodium aluminum hydride gained wide attention as a hydorgen storage material after the discovery that adding a few mol. % Ti resulted in *reversible* hydrogen storage [1]. Early efforts to understand the effect of the catalyst focused on the type transition metal used and were generally solution-based or "wet" doping techniques [2]. Studies of mechanically-milled or "dry" doped materials focused on Ti-halide dopant precursors, with results indicating that many dopant precursors, such as $TiCl_2$, $TiCl_3$, TiF_3, $TiBr_4$, and others, are suitable candidates for mechanically-milled samples of activated $NaAlH_4$ [3]. However, the specific mechanim of enhanced kinetics of hydrogen sorption due to Ti, remained a mystery. Although the mechanism has not been determined conclusively, the following work describes experiments and theoretical calculations carefully designed to probe the question.

Chapter 1 investigates the structure of Ti-doped $NaAlH_4$, and Na_3AlH_6, through Rietveld refinements of powdered x-ray and neutron diffraction data. The refinements indicate that no large structural changes occur in $NaAlH_4$ or Na_3AlH_6 upon Ti-doping and hydrogen-cycling of the sample. The calculated electronic structure of $NaAlH_4$ and Na_3AlH_6 illustrates the charge separation between the Na cations and AlH_4, and AlH_6 anions, and the ionic nature of the bonding between these units in the crystal lattices. The resulting structures can be considered "complex ionic" crystals. The Al-H bonding in the anions is polar-covalent. This work is published in reference [4].

Sodium alanate samples can be doped with transition metals by many methods, for example, mechanical milling (dry) or solution methods described above. In an effort to understand where the Ti is located in $NaAlH_4$, crystals were grown in tetrahydrofuran (THF) solution in which Ti was present as a dopant, in order to determine the solubility of Ti in the crystal lattice. In addition, an attempt was made to characterize any resulting Ti-compounds, with x-ray diffraction and NMR, that formed from Ti not incorporated into the crystal lattice of $NaAlH_4$. The resulting Ti compounds formed from these different doping techniques are addressed in Chapter 2. Dry doping techniques mainly result in the formation of $TiAl_3$, while solution doping in THF resulted in an unknown Ti-Al compound of nanometer scale dimensions. This work is published in reference [5].

Ti-doped sodium alanate is known to desorb hydrogen at temperatures as low as ambient, and appreciable rates are easily obtained at temperatures of 90°C. These temperatures are well below the melting point of pure $NaAlH_4$ at 180°C, suggesting that the processes that destabilize the crystal lattice, and hence result in hydrogen desorption, may be addressed through an understanding of the lattice vibrational modes in the crystal. Macroscopic crystals of $NaAlH_4$ of millimeter dimension were grown and both isothermal polarized Raman and in-situ temperature dependent powder Raman spectra were collected. Chapter 3 discusses the experimentally determined symmetry and frequencies of the vibrational modes of the pure crystal.

Calculational results detail the mode symmetries, and also the degree of anharmonicity of the lattice through a computation of the Gruniesen parameters. The results of this work illustrate that even at the melting temperature of the un-doped $NaAlH_4$ crystal, the AlH_4 anions are quite stable, with no hydrogen desorption, thus constraining the possible explanations of the mechanism of the transition metal "dopants". This work is published in reference [6].

Large scale production of Ti-doped sodium alanate through mechanical-milling of powders is likely cost prohibitive compared to solution-doping techinques. Chapter 4 continues the investigation of the solution doped samples through multiple quantum nuclear magnetic resonance techniques (MQ NMR). The results indicate that the solution used for doping is very important in determining the compounds formed, especially with transition metals in solution, when the solvent molecules are strongly polar. This information is very important when considering scale-up of production techniques. This work is published in reference [7].

Bibliography

[1] B. Bogdanovic and M. Schwickardi. Ti-doped alkali metal aluminium hydrides as potential novel reversible hydrogen storage materials. *Journal of Alloys and Compounds*, 253-254(1-2):1 – 9, May 1997.

[2] B. Bogdanovic, R.A. Brand, A. Marjanovic, M. Schwickardi, and J. Tolle. Metal-doped sodium aluminium hydrides as potential new hydrogen storage materials. *J. Al. Comp.*, 302(1-2):36 – 58, April 2000.

[3] E.H. Majzoub and K.J. Gross. Titanium-halide catalyst-precursors in sodium aluminum hydrides. *Journal of Alloys and Compounds*, 356-357:363 – 7, August 2003.

[4] V. Ozolins, E.H. Majzoub, and T.J. Udovic. Electronic structure and rietveld refinement parameters of ti-doped sodium alanates. *J. Al. Comp.*, 375:1 – 10, 7 2004.

[5] E.H. Majzoub, J.L. Herberg, R. Stumpf, S. Spangler, and R.S. Maxwell. Xrd and nmr investigation of ti-compound formation in solution-doping of sodium aluminum hydrides: solubility of ti in naalh4 crystals grown in thf. *Journal of Alloys and Compounds*, 394:265 – 270, 5 2005. Elsevier B.V.

[6] E. H. Majzoub, K. F. McCarty, and V. Ozolins. Lattice dynamics of naalh4 from high-temperature single-crystal raman scattering and ab initio calculations: Evidence of highly stable alh4- anions. *PHYSICAL REVIEW B*, 71(2):024118 –, JAN 2005.

[7] J.L. Herberg, E.H. Majzoub, and R.S. Maxwell. ^{27}al and ^{1}h mas nmr and ^{27}al multiple quantum studies of ti-doped $naalh_4$. *Journal of Alloys and Compounds*, October 2005. In press.

This page intentionally left blank

Contents

List of Figures

List of Tables

Chapter 1

Electronic structure and Rietveld refinement parameters of Ti-doped sodium alanates

V. Ozoliņš[1]
Department of Materials Science and Engineering
University of California, Los Angeles
Los Angeles, CA 90095-1595

E.H. Majzoub[2]
Sandia National Laboratories,
P.O. Box 969, Livermore, CA 94551

T.J. Udovic
NIST Center for Neutron Research
National Institute of Standards and Technology
Gaithersburg, MD 20899-8562

Abstract

The structure of Ti-doped sodium aluminum deuteride has been determined using Rietveld refinement of x-ray and neutron powder diffraction data and compared to values for undoped $NaAlD_4$ and $NaAlH_4$. The refined lattice parameters for the tetragonal $NaAlD_4$ structure are found to be a=5.010 Å and c=11.323 Å, while those of the monoclinic Na_3AlD_6 structure are a=5.402 Å, b=5.507 Å, c=7.725 Å, and β=89.491°. Results of *ab initio* calculations of the lattice parameters are within a few per cent of the Rietveld-refined values. The generalized gradient approximation (GGA) is found to produce signif-

[1]Corresponding author. Tel.: +1-310-267-5538; fax: +1-310-206-7353. *E-mail address:* vidvuds@seas.ucla.edu

[2]Tel.: +1-925-294-2498; fax: +1-925-294-3410. *E-mail address:* ehmajzo@sandia.gov

icantly better agreement with the experimental data than the local-density approximation (LDA), which is attributed to a very inhomogeneous distribution of electronic density in the alanates. The Rietveld refinement, LDA, and GGA results for the Al-H bond length in $NaAlD_4$ are 1.626, 1.634, and 1.631 Å, respectively. Refined values of the Al-H bond lengths in Na_3AlD_6, are in agreement within 2 % of earlier work on undoped Na_3AlD_6. The calculated GGA formation energies for the decomposition reactions of $NaAlD_4$ and Na_3AlD_6 are 33.5 and 49.9 kJ per mole of H_2, respectively. The corresponding LDA values are significantly higher: 44.6 and 70.3 kJ per mole of H_2. Comparison with the experimental enthalpy data suggests that the GGA results are in a very good agreement with the measured ΔH. Detailed theoretical analyses of the electronic band structure, valence charge density distribution, and lattice bonding properties are given.

Keywords: A. hydrogen storage materials, B. mechanical alloying, C. x-ray diffraction, neutron diffraction, structural modeling, Rietveld refinement D. electronic band structures, crystal bonding

1.1 Introduction

Recent advances in achieving reversible hydrogen storage in light-metal hydrides have sparked a renewed interest in these materials as storage media for future hydrogen-powered devices. In particular $NaAlH_4$, containing 7.4 wt. % H, has proven to be a reversible hydrogen absorption/desorption material with about 4 wt. % hydrogen available [1]. Although much research has been done to optimize the kinetics of this reaction, there are still many unanswered questions regarding the physical mechanism of enhanced kinetics upon doping with Ti [2, 3, 4, 5, 6].

Sodium aluminum tetrahydride decomposes in two steps, first into the hexahydride Na_3AlH_6, which further decomposes into NaH as follows:

$$NaAlH_4 \rightleftharpoons \frac{1}{3}Na_3AlH_6 + \frac{2}{3}Al + H_2, \tag{1.1}$$

$$Na_3AlH_6 \rightleftharpoons 3\ NaH + Al + \frac{3}{2}H_2. \tag{1.2}$$

Earlier single crystal x-ray diffraction studies [7, 8] have determined that the tetrahydride, $NaAlH_4$, has a body-centered tetragonal unit cell with the space group $I4_1/a$. The lattice parameters were obtained by Bel'skii *et al.* [7] and Laugher *et al.* [8], who found a=5.021(1) Å and c=11.346(2) Å, and a=5.020(2) Å and c=11.330(3) Å, respectively. A neutron powder diffraction refinement of the hexahydride Na_3AlH_6 by Rönnebro *et al.* [14] found a monoclinic unit cell with the space group $P2_1/n$ and lattice parameters of a=5.390(2) Å, b=5.514(2) Å, c=7.725(3) Å, and β=89.863°.

While the preceding work was performed on single crystals of $NaAlH_4$ and powders of Na_3AlD_6, it is of great interest to study the structures of phases present in

Ti-doped alanates which show enhanced kinetics for hydrogen adsorption and desorption. Our interest is motivated by the fact that Ti-doping is essential for achieving reversible hydrogen storage [9]. Determination of the type of phases present and their structure is the necessary first step for understanding the mechanism by which Ti doping increases the reaction kinetics for Eqs. (3.1) and (3.2).

1.2 Experimental details

Ti-doped $NaAlD_4$ material was prepared from $TiCl_3$, Na (99.99%) and 20 μm Al (99.99%) powder purchased from *Sigma-Aldrich* using a direct synthesis method [11]. A 7 g mixture of 1:1:0.04 molar ratio of Na:Al:$TiCl_3$ was mechanically milled in a *SPEX* 8000 high energy mill, using a WC milling pod and 6-9 25 g WC balls. The sample was transferred to a stainless-steel sample vessel and connected to a pressure and temperature-controlled manifold. All steps for sample preparation and transfer into the reactor vessel occurred inside an Ar glove box with oxygen levels below 3 ppm.

Absorption and desorption of deuterium (99.9%) were determined from pressure measurements in a calibrated fixed-volume apparatus. The sample was placed in a 15 mm diameter 316SS vessel of approximately 12 cc volume with a 1 mm diameter internal thermocouple well for rapid temperature response. The sample was held in place on the top and the bottom with *Fiberfax* glass fiber. Absorption measurements were made using a calibrated volume of 120 cc at pressures around 10 MPa. Absorption pressures were measured using a *Teledyne Taber* model 206 piezoelectric transducer with a resolution of 10^{-2} MPa. Measured values of (mols H)/(mols Al) have a resolution of about ± 0.2. The volume used for the desorption measurements was about 1040 cc, and the pressure was measured using a *Baratron* capacitance manometer with a resolution of 10^{-7} MPa. The sample temperature was regulated with an *Omega* model CN76000 PID controller connected to heating tape wrapped around the exterior of the SS vessel. The temperature of the sample interior was measured using a thermocouple well. Typical absorptions parameters were 120°C and 8.5 MPa hydrogen overpressure. Desorptions were measured in the 1040 cc volume initially evacuated to 1 torr.

During the first absorption, the sample was taken to a temperature of 250°C and a pressure of 8 MPa in order to form the NaD required for the formation of $NaAlD_4$. The amount of hydrogen absorbed during the first absorption corresponded to the amount needed for formation of NaD and no hexadeuteride or tetradeuteride were formed. The sample was cooled to room temperature, and the manifold was evacuated and prepared for a desorption measurement. No desorption of deuterium was observed up to a temperature of 160°C. The second absorption cycle resulted in no observed pressure drop and the sample was removed from the vessel and mechanically milled for 30 min to redistribute the material for further absorptions. The third and fourth absorptions showed deuterium absorptions corresponding to a mo-

lar ratio of D/Al of about 1.8. A molar ratio of D/Al=3 is required on absorption to form $NaAlD_4$ from NaD and Al.

The sample was characterized for hydride-phase content following absorption and desorption cycles using x-ray diffraction with Cu-K_α radiation on a *Scintag* XDS-2000 using Bragg-Brentano geometry. A sample of about 0.2 g was placed between two Mylar films sealed at the edges to prevent air exposure. The count time for each step of 0.02° 2θ was 1 second.

Neutron powder diffraction was performed at the NIST Center for Neutron Research of the National Institute of Standards and Technology using the high-resolution, 32-counter, BT-1 diffractometer. A 2.8 g sample of the absorbed material was sealed in a 1.27 cm diameter vanadium can under He. The measurement used a 15' in-pile Soller collimator and Cu(311) monochromator producing a neutron wavelength of 1.540 Å. Sample data was binned into 0.05° 2θ increments. The data was taken at 295 K.

1.3 Rietveld refinement

A combined Rietveld refinement using neutron and x-ray powder diffraction data was performed with SIMREF 2.6 [12]. The results are shown in Figs. 1.2 and ??. Peak shapes of the x-ray data were fit using the pseudo-Voigt profile containing a mixture of Gaussian and Lorentzian shapes. Profiles for the neutron data set were fit to pure Gaussian. Refinement of the diffraction data for deuterium atom positions of $NaAlD_4$ was complicated due to the four phases present in the sample, the tetra-deuteride $NaAlD_4$, the hexa-deuteride Na_3AlD_6, NaCl, and Al. Due to the small level of Ti-doping (4 at. %), the presence of Ti-Al compounds could not be conclusively determined [13] and no attempt was made to include any Ti-Al phases in the refinements. To simplify the refinement of the tetra-deuteride, the initial atom positions of the hexa-deuteride were fixed to those determined from the dual phase refinement performed by Rönnebro *et al.* [14], which included only NaD as an impurity phase. The atom positions and lattice parameters were then refined for the hexa-deuteride phase independently of the tetra-deuteride. The tetra-hydride phase parameters were then refined once more. The NaCl present in the sample was used as an internal lattice parameter standard. The pattern zero was adjusted so that the NaCl lattice parameter $a = 5.6402$ Å. Lattice parameters of the remaining phases were refined while holding the NaCl parameter and pattern zero fixed.

Isotropic thermal parameters, B_{iso}, were used for each atom to describe the drop in intensity at higher momentum transfer due to the Debye-Waller factor, $\exp(-2\pi^2 B_{\text{iso}} k^2)$. A negative whole-pattern temperature factor of $B_{\text{iso}} = -0.7$ Å^2 could correct for the low peak intensities at lower k values in the x-ray data, suggesting that surface roughness or absorption effects may be important [15]. This temperature factor was not included in the I_{calc} pattern in Figure 1.2. Refined occupancies for the tetra and hexa-deuterides never rose above 1.1 and those ris-

ing above unity were set at 1. The definition of the residuals R_p, R_{wp}, R_e, and R_{Bragg}, can be found in the SIMREF technical manual [12]. The number of data points and parameters were N, and P, respectively. The weights for each data point, y_i^{obs}, were calculated as $w_i = 1/\sigma_i^2$, where the σ_i were the estimated standard deviations of the observed data points. The "goodness-of-fit" is defined as, $S = [\chi^2/(N-P)]^{1/2} = R_{wp}/R_e$ and is typically less than 4 for a crystallographically significant fit. The refinement performed for this four-phase system resulted in $S = 3.89$. The Bragg factors, R_{Bragg}, for each phase and the residuals for each data set are listed in Table 2.2. The largest discrepancy is clearly in the x-ray fit for the hexa-deuteride, with $R_{Bragg} = 46\%$. This phase has several hundred calculated reflections in the x-ray data in the ranges of 2θ collected. This complicates the fit considerably and results in relatively poor R_{Bragg} factors for the other phases present in the x-ray data. Also, due to the air sensitivity of the powder samples, for x-ray diffraction they were sandwiched between two pieces of mylar and suspended in a circular holder. The resulting surface exposed to the x-ray beam was not completely flat, which could contribue to peak shifting due to the small variable in the sample height. However, our interest is primarily in the tetra-deuteride phase with an R_{Bragg} factor for the neutron fit of 5%. The overall residuals for the neutron data set are $R_p = 3.6\%$ and $R_{wp} = 4.5\%$, below the generally accepted value of 10% required for a good fit. The Durbin-Watson statistical values $d = 0.538$, and $Q = 1.9282$ [16], indicate a positive serial correlation for successive values of the residuals for $d < Q < 2$. The parameter Q for a significance level of 0.1%, as defined in SIMREF, is $Q = 2[(N-1)/(N-P) - 3.0902/\sqrt{N-P}]$. In addition, the first-principles calculations below, which show good agreement with the refined values of the atom positions in the tetra and hexa-deuteride [see Table 1.2], further reinforce our confidence in the fit to the data.

Table 1.1: Refinement residuals for the four phase refinement of $NaAlD_4$, Na_3AlD_6, Al, and NaCl.

Phase R_{Bragg} Factors				
Data Set	$NaAlD_4$	Na_3AlD_6	Al	NaCl
x-ray	0.214	0.460	0.109	0.170
Neutron	0.050	0.145	0.073	0.060
Total	0.063	0.149	0.093	0.080

Overall Residuals					
Data Set	R_p	R_{wp}	R_{exp}	$(N-P)$	S
x-ray	0.144	0.183	0.094	4575	1.94
Neutron	0.036	0.045	0.008	2840	5.78
Total	0.052	0.049	0.013	7416	3.89

Table 1.2: Rietveld refinement results for the four-phase mixture of $NaAlD_4$, Na_3AlH_6, Al, and NaCl. Numbers in parenthesis indicate refinement standard deviations only. Lattice parameter accuracy is estimated to be ± 0.001 Å.

	Site	x	y	z	Occupancy	B_{iso}
$NaAlH_4$ $I4_1/a$ $a = 5.0099$ $c = 11.3228$ [Å]						
Al	4(b)	0	1/4	5/8	0.9621(8)	1.65(1)
Na	4(a)	0	1/4	1/8	0.9432(9)	2.07(1)
D	16(f)	0.26214(3)	0.61750(3)	0.04682(2)	1.0061(2)	2.623(2)
Na_3AlH_6 $P2_1/n$ $a = 5.4018$ $b = 5.5074$ $c = 7.7251$ [Å] $\beta = 89.491$ [°]						
Al	2(a)	0	0	0	1.0	4.3(1)
Na	2(b)	0	0	0.5	0.915(6)	8.2(2)
Na	4(e)	-0.0151(4)	0.4416(4)	0.2415(4)	0.969(3)	0.22(4)
D1	4(e)	0.0918(3)	0.0352(3)	0.2207(2)	1.0	4.09(5)
D2	4(e)	0.2220(4)	0.3283(2)	0.5454(2)	0.999(2)	0.33(2)
D3	4(e)	0.1649(3)	0.2689(3)	0.9500(2)	1.005(3)	2.18(3)
Aluminum $Fm\bar{3}m$ $a = 4.0497$ [Å]						
Al	4(a)	0	0	0	1.0	0.801(8)
NaCl $Fm\bar{3}m$ $a = 5.6402$ [Å]						
Na	4(b)	0.5	0.5	0.5	1.0	1.424(7)
Cl	4(a)	0	0	0	1.0	1.67(2)

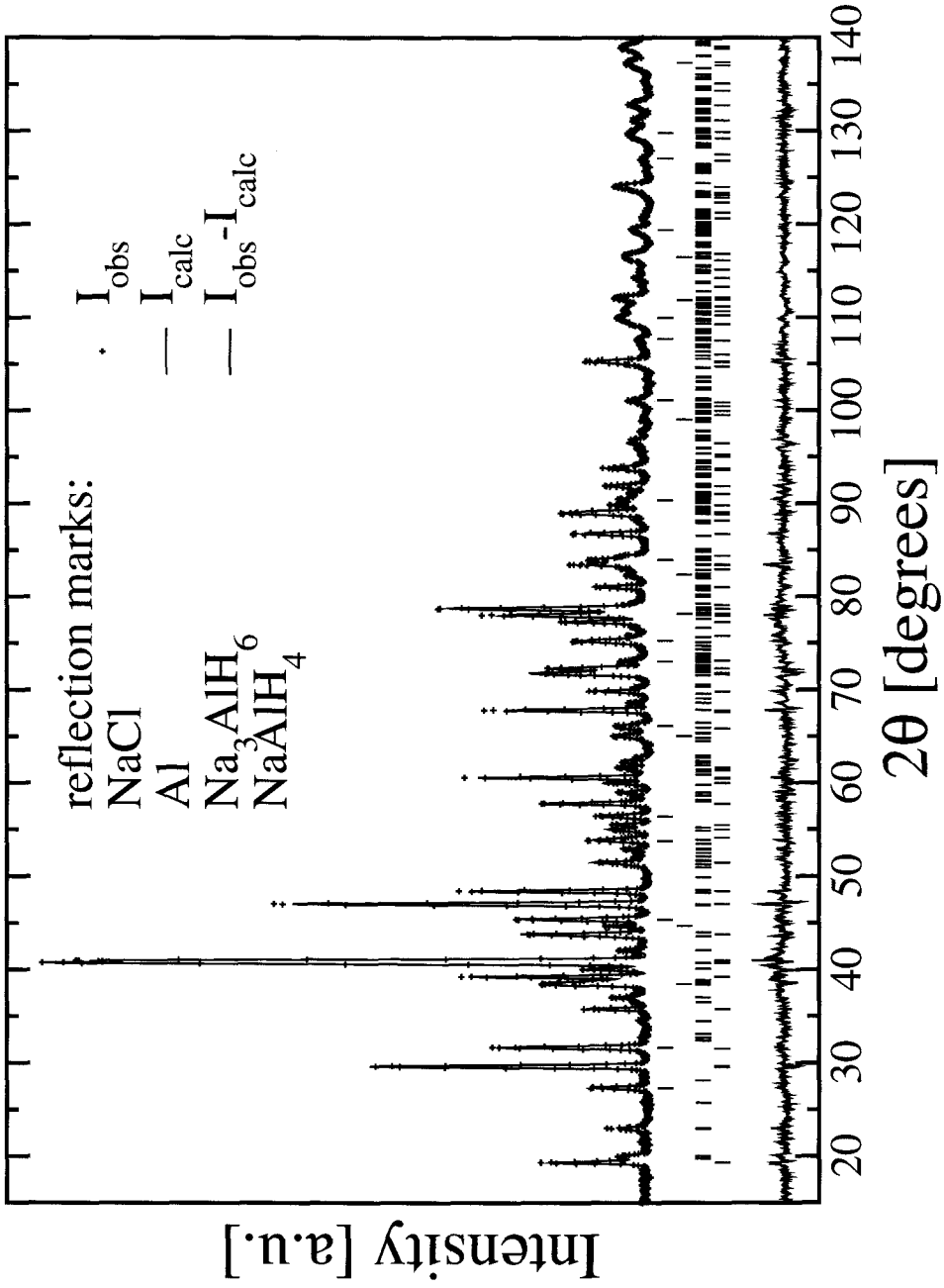

Figure 1.1: Rietveld refinement results of powder neutron diffraction of a phase mixture of $NaAlD_4$, Na_3AlD_6, NaCl, and Al. The difference curve between the observed data (+) and calculated data (—) is shown at the bottom of the panel (—). The calculated reflection locations for each phase are indicated by vertical lines.

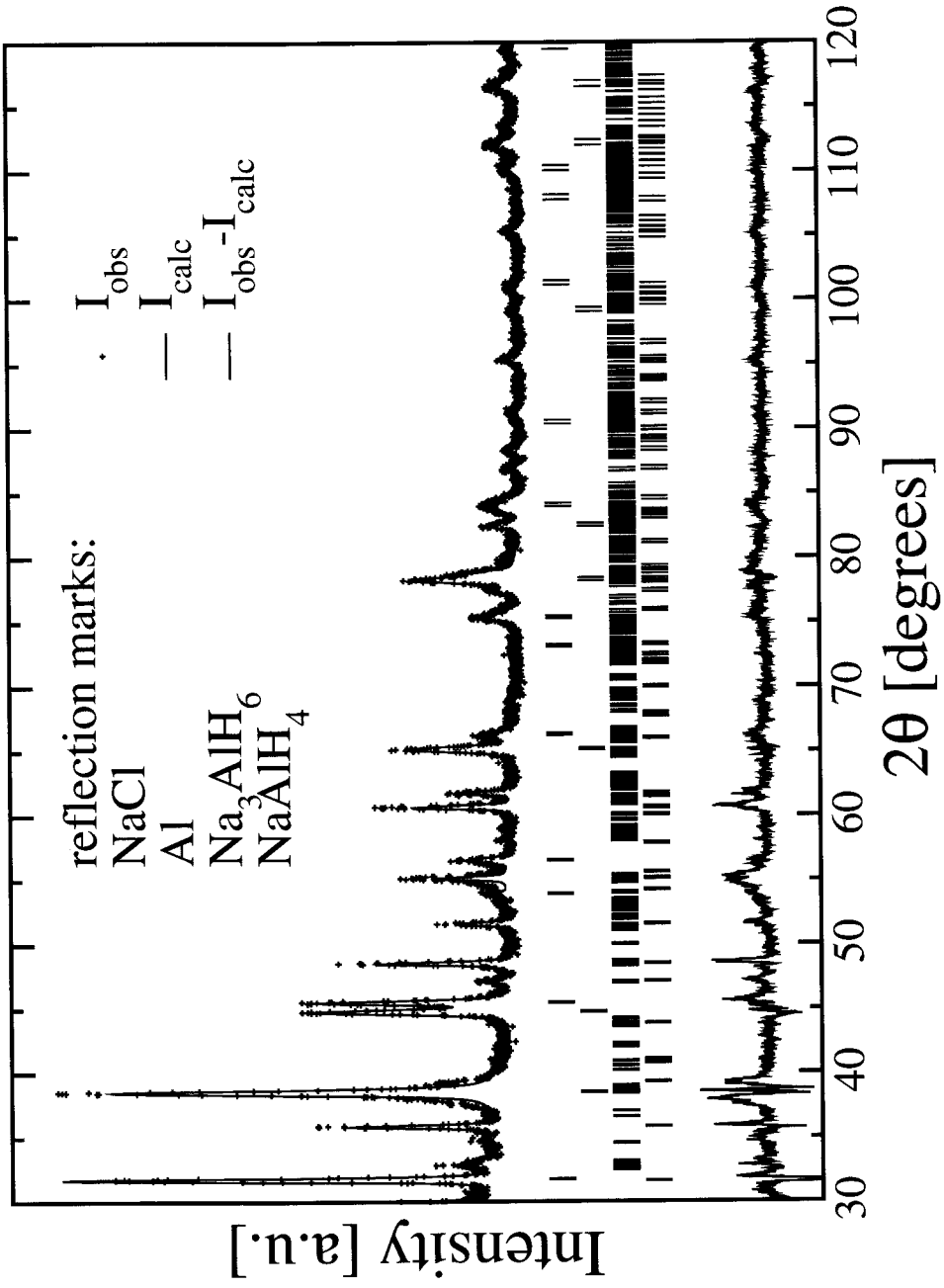

Figure 1.2: Rietveld refinement results of powder x-ray diffraction of a phase mixture of $NaAlD_4$, Na_3AlD_6, NaCl, and Al. The difference curve between the observed data (+) and calculated data (—) is shown at the bottom of the panel (—). The calculated reflection locations for each phase are indicated by vertical lines.

1.4 *Ab initio* Calculations

First-principles electron-structure calculations were performed using the Vienna Ab-Initio Simulation Package (VASP) developed at at the Institut für Material-physik of the Universität Wien [17, 18]. Electronic wave functions and valence charge density were expanded in the basis of plane waves with a well-converged cutoff energy of 436.8 eV. The sharply localized core states of Al and Na were eliminated and plane wave convergence accelerated using ultrasoft Vanderbilt pseudopotentials [20]. Due to their extended nature, Na $2p$ semicore states were explicitly included in our calculation along with the H $1s$, Al $3s$ and $3p$, and Na $3s$ valence electrons. For Al, the frozen core correction [21] was used to account for the nonlinearity of the exchange-correlation functional. Both the popular local-density approximation (LDA), as parametrized by Perdew and Zunger [22] and the generalized gradient approximation of Perdew and Wang [23] (GGA-PW91) were used to represent electronic exchange-correlation effects. Brillouin zone integrals were performed over regular Monkhorst-Pack [24] grids with $12 \times 12 \times 8$ and $12 \times 12 \times 8$ k-points for the $NaAlH_4$ and Na_3AlH_6 structures, respectively. During the calculation, exact quantum-mechanical forces and stresses were used to perform a full structural optimization of the atomic positions and unit cell vectors. The calculated geometries are given in Table 1.3.

Table 1.4 lists the calculated cohesive (atomization) energies of all compound phases involved in the decomposition reactions Eqs. (3.1) and (3.2). These energies were obtained by subtracting the energies of individual isolated atoms from the total energy of the crystal with structurally optimized lattice parameters and atomic positions. Energies of atoms were also obtained using the VASP code by considering an atom in a large cubic box. To ensure cancellation of systematic errors, we used the same plane wave cutoff energy and the same parameterizations of the exchange-correlation functional (LDA or GGA) as for the bulk crystals. The cohesive energies in Table 1.4 have been used to evaluate the internal energy changes ΔE in reactions Eqs. (3.1) and (3.2). These formation *energies* are given in Table 1.5 together with the experimental data for the *enthalpies* ΔH from Bogdanovic *et al.* [1].

1.5 Structure and Thermodynamics

The lattice parameters and atomic coordinates for each phase obtained through the Rietveld refinement are indicated in Table 1.2. The lattice parameters for Ti-doped $NaAlD_4$ are found to be a=5.010 Å and c=11.323 Å. These values are within 0.2 % of those obtained by Bel'skii and Laugher for $NaAlH_4$, and to within 0.1 % of values for undoped $NaAlD_4$ by Hauback *et al.* [28] suggesting that no significant crystal structure changes take place due to 4 at.% Ti doping. The lattice parameter changes may be attributed to our sample being deuteride rather than hydride, as the saline deuterides also tend to have about 0.2 % smaller lattice parameters than

Table 1.3: Calculated atom positions and unit cell dimensions in $NaAlH_4$ and Na_3AlH_6.

Atom	Site	x	y	z	$d(\mathrm{Al}-\mathrm{H})$ [Å]
		LDA results			
$NaAlH_4$ $I4_1/a$ $a = 4.83$ $c = 10.56$ [Å]					
Al	4(b)	0	1/4	5/8	
Na	4(a)	0	1/4	1/8	
H	16(f)	0.2626	0.5967	0.0400	1.63
Na_3AlH_6 $P2_1/n$ $a = 5.21$ $b = 5.42$ $c = 7.50$ [Å] $\beta = 89.86$ [°]					
Al	2(a)	0	0	0	
Na	2(b)	0	0	1/2	
Na	4(e)	-0.0108	0.4496	0.2522	
H1	4(e)	0.1030	0.0481	0.2196	1.75
H2	4(e)	0.2230	0.3305	0.5463	1.75
H3	4(e)	0.1605	0.2728	0.9367	1.76
		GGA-PW91 results			
$NaAlH_4$ $I4_1/a$ $a = 4.99$ $c = 11.07$ [Å]					
Al	4(b)	0	1/4	5/8	
Na	4(a)	0	1/4	1/8	
H	16(f)	0.2662	0.6084	0.0442	1.63
Na_3AlH_6 $P2_1/n$ $a = 5.32$ $b = 5.56$ $c = 7.72$ [Å] $\beta = 89.72$ [°]					
Al	2(a)	0	0	0	
Na	2(b)	0	0	1/2	
Na	4(e)	-0.0184	0.4460	0.2502	
H1	4(e)	0.1014	0.0454	0.2153	1.77
H2	4(e)	0.2290	0.3313	0.5458	1.76
H3	4(e)	0.1603	0.2671	0.9372	1.78

Table 1.4: Calculated cohesive energies E_c, of the hydrogen compound phases in Eqs. (3.1) and (3.2). All values are given in eV per formula unit.

Compound	LDA	GGA-PW91	Expt.
$NaAlH_4$	16.562	14.780	
Na_3AlH_6	25.464	22.576	
NaH	4.318	3.813	
Al	4.052	3.514	3.39
H_2	4.911	4.566	4.49

Table 1.5: Change in the internal energy for the decomposition reactions Eqs. (3.1) and (3.2). ΔE_{LDA} and ΔE_{GGA} represent energies calculated from the static-lattice cohesive energies E_c given in Table 1.4 using the LDA and GGA, respectively. All results are given in kJ/mol.

	ΔE_{LDA}	ΔE_{GGA}	ΔH_{exp} (Ref. [1])	ΔH_{exp} (Ref. [26])
ΔE [Eq. (1)]	44.6	33.5	37	35
ΔE [Eq. (2)]	70.3	49.9	47	48

the hydrides [27].

The Rietveld refinement results for the Al-D bond length in $NaAlD_4$ are 1.626 Å, while the LDA and GGA results for the Al-H length were 1.634, and 1.631 Å, respectively. The single crystal refinement of the hydrogen atom positions performed by Lauher, *et al.* [8] gave an Al-H bond distance of 1.532(7) Å, and the refinement by Bel'skii *et al.* gave 1.61(4) Å [7]. Our Al-D bond length is identical to that found by Hauback *et al.* [28] for undoped $NaAlD_4$.

Rietveld refined values for the Al-H bond distances for the hexa-deuteride are 1.786, 1.809, and 1.771 Å, respectively, for each of the deuterium atom positions (D1-D3) listed in Table 1.2. The differences between the atomic coordinates and lattice parameters of this work, compared to the refined values of Rönnebro, et. al [14] were less than 2 % for each parameter. Theoretical calculations give Al-H bond lengths for each of the hydrogen atom positions (H1-H3) listed in Table 1.3 of 1.75, 1.75, and 1.76 Å using the LDA, and 1.77, 1.76, 1.78 Å using the GGA.

Comparison of the Rietveld refinement data with the results of theoretical calculations shows that the generalized gradient approximation (GGA-PW91) is fairly successful in reproducing lattice geometries of sodium alanates. Indeed, the predicted a and c lattice parameters of $NaAlH_4$ are only 0.4 % and 2.2 % smaller than the values obtained through the Rietveld refinement. Comparably good agreement has also been obtained for the Na_3AlH_6 lattice parameters, which deviate by only 1.5 %, −1.0 %, and −0.1 %. Nevertheless, the 2.2 % discrepancy (or 0.25 Å) in the c-parameter of $NaAlH_4$ is a bit larger than usual for covalently bonded compounds, pointing to a possibility that lattice vibrations, neglected in a static geometry optimization, may contribute to expansion along the c-axis. Indeed, due to the light mass of hydrogen, the vibrational amplitudes and frequencies are very high (to be discussed in an upcoming publication [25]). This may directly affect the lattice geometry via anharmonic effects. On the other hand, it is also possible that sodium alanates belong to a particularly complicated class of materials and the error in the predicted c-parameter is entirely due to the deficiencies of approximate density functionals like LDA or GGA. Finally, we note that the agreement between the Rietveld-refined and first-principles-calculated bond lengths is about the same as the agreement for lattice parameters. The largest discrepancy with the results of Rietveld refinement is found to be almost 3 % for the Al-H bond length in Na_3AlD_6, which could be caused either by the approximate nature of the GGA or by the failure to account for vibrational effects in the theoretical calculation.

The data in Table 1.3 shows that the popular local-density approximation (LDA) seriously underestimates the lattice parameters of both $NaAlH_4$ and Na_3AlH_6. The largest error is again observed for the c-parameter of the $NaAlH_4$ structure, which differs from the experimental value by 0.76 Å or 6.7 %. Errors in the other lattice parameters are smaller, but still appreciable. This is a well-known deficiency of the LDA, which has been attributed to the neglect of electronic exchange-correlation effects associated with charge inhomogeneities. The latter are expected to be rel-

atively small in close-packed metallic systems with nearly free-electron-like charge distribution, but they cannot be expected to be small in alanates with covalent Al-H bonds. The GGA is specifically constructed to take into account contributions to the exchange-correlation from electronic charge density gradients, and therefore it does a much better job of predicting the equilibrium geometries, as evidenced by the data in Table 1.3.

From the calculated cohesive binding energies in Table 1.4, one can obtain the formation energies corresponding to Eqs. (3.1) and (3.2). These data are given in Table 1.5 for both the LDA and GGA functionals. The experimental *enthalpy* data are given in the last two columns of Table 1.5. The difference between our calculated formation energies and the measured enthalpies is given by a sum of several contributions: the lattice vibrational energy of ions, vibrational, rotational and kinetic energies of H_2 molecules, and the pV term in the definition of the enthalpy ($H = E+pV$). For hydrogen desorption reactions, the largest contribution to pV is that of the gas of H_2 molecules, which is approximately given by the ideal-gas equation-of-state, $pV = Nk_BT$. Since the energy of atomic vibrations is also on the order of a few k_BT, an accurate calculation of the enthalpy necessarily requires the knowledge of crystal lattice vibrations and of the associated vibrational energies. Such a study is beyond the scope of this paper and will be presented elsewhere [25]. If one assumes that the thermal energies cancel out on both sides of Eqs. (3.1) and (3.2), the enthalpy change is approximately given by the internal energy change. It is seen that the GGA predicts values of ΔE that are in a very good agreement with the enthalpy data determined from plateau measurements in Refs. [26, 1]. In contrast, the LDA gives consistently higher values of ΔE, indicating that it overbinds the alanate compounds relative to the end products sodium monohydride, bulk aluminum, and molecular hydrogen. These results seem to suggest that enthalpy contributions beyond the static internal energy indeed cancel out on both sides of Eqs. (3.1) and (3.2).

1.6 Electronic Structure and Bonding

1.6.1 $NaAlH_4$

The established chemical intuition about the nature of bonding in alanates suggests that $NaAlH_4$ is an ionic crystal formed by positively charged Na^+ ions and negatively charged AlH_4^- groups. Within the AlH_4^- group the bonding is expected to be polar covalent, since the Pauling electronegativity of H (+2.1) is substantially higher than that of Al (+1.5). Furthermore, the tetrahedral structure of the AlH_4^- group suggests that the bond is formed between sp^3 hybridized orbitals on Al and s orbitals on H atoms. The valence band structure of $NaAlH_4$ then should be thought of as arising from an overlap of molecular-type orbitals centered on the AlH_4^- units, while the role played by sodium is to donate an electron to the AlH_4^- group and provide

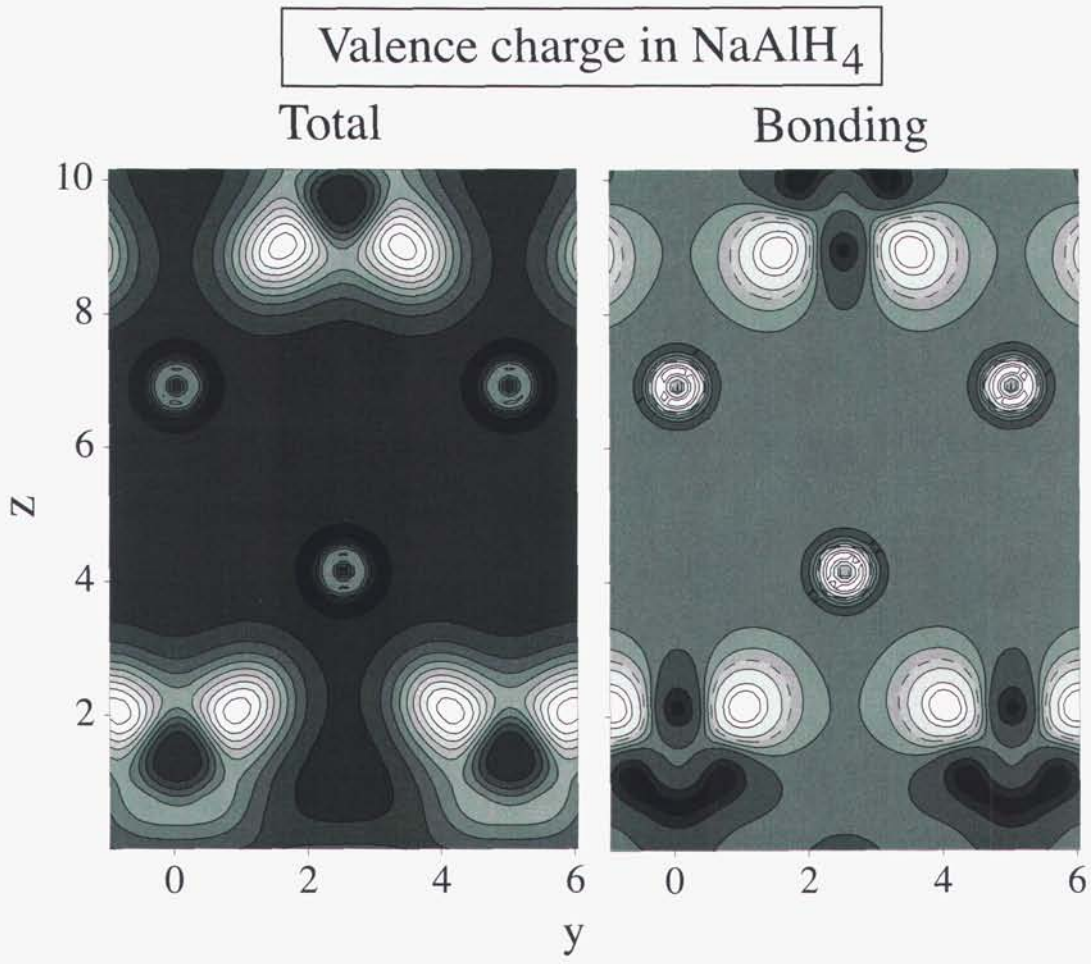

Figure 1.3: *Left:* Valence charge density of $NaAlH_4$ in the plane parallel to the y and z axes and going through the Na and Al positions. Na ions are positioned at approximately $(2.6, 4.2)$, $(0, 6.9)$, and $(5.0, 6.9)$, while Al ions are at $(0, 1.4)$, $(5, 1.4)$, and $(2.5, 9.6)$. Hydrogen ions are outside the plane of the plot at the center of the charge density maxima, shown in white. The highest density contour corresponds to 45 electrons/Å^3, and the spacing between successive contour levels is 5 electrons/Å^3. *Right:* Bonding charge density $\rho_{\rm bond}$, defined as a difference between the self-consistent valence charge density (shown on the left) and the charge density obtained by overlapping free-atom charges, $\rho_{\rm bond} = \rho_{\rm val} - \rho_{\rm overlap}$. Zero level is shown by a dashed line; the contour spacing is 2 electrons/Å^3. Charge transfer from Al and Na to H ions is evident.

an electrostatic stabilization of the lattice. Analysis of the valence charge density, presented in Fig. 1.3, supports this intuitive interpretation. Indeed, the electronic charge is overwhelmingly concentrated in the vicinity of H atoms and drops to very low values in the space between neighboring AlH_4 units. It is also evident that most of the charge is concentrated around H ions, and almost none is found near Na (small rings of increased density are due to crystal field-induced rearrangement of Na semicore p charge). The right panel of Fig. 1.3 shows the so-called bonding charge density, given by the difference between the self-consistently calculated valence charge and that obtained by overlapping free-atom charge densities. Positive values, shown in light colors in Fig. 1.3, correspond to charge being transfered to H ions, while dark greys around Na and Al atoms prove that electrons are stripped away from those regions. These observations demonstrate that the main function of Na is to donate its valence electron and to participate in electrostatic stabilization of the lattice. We return to the role of the electrostatic energy below in Sec. 1.6.3. It is also apparent from Fig. 1.3 that Al atoms have given up their valence electrons to the surrounding more electronegative H^- ions, an observation that confirms the hypothesis that Al-H bonds are of polar covalent nature.

The electronic structure of $NaAlH_4$ can be conveniently understood in terms of the energy levels of a negatively charged tetrahedral AlH_4^- unit, which we explain first. Using the VASP code, we obtained self-consistent ground state energy levels of AlH_4^-, embedded in a uniform positive background charge, representing the charge compensation effect due to Na^+ ions. Al-H bondlengths in the AlH_4^- unit were relaxed using calculated quantum mechanical forces. The equilibrium Al-H bond length was found to be $r_{Al-H} = 1.64$ Å, which is very close to the Al-H bond observed in bulk $NaAlH_4$. The calculated energy levels are shown in Fig. 1.4 together with symmetry designations of the corresponding irreps of the T_d point group. We find that the lowest level has the A_1 symmetry, which can be thought of as a symmetric combination of H-centered 1s orbitals. It is followed by a triply degenerate HOMO level of T_2 symmetry, which from the symmetry perspective behaves like an Al-centered p orbital. In fact, it is predominantly a linear combination of H $1s$ orbitals with some admixture of Al p-character, as can be easily seen from the charge density plot in Fig. 1.3. The LUMO state is an A_1 singlet positioned 3.5 eV above the T_2 level whose charge density has an appreciable weight on the Al atom, suggesting that it is derived from Al $3s$ states.

The energy diagram in Fig. 1.4 provides a convenient scheme for interpreting the calculated electronic band structure of $NaAlH_4$, shown in Fig. 1.5. The unit cell of $NaAlH_4$ contains two formula units; therefore, the number of energy bands is doubled with respect to AlH_4^-. Tetragonal symmetry of $NaAlH_4$ leads to a slight distortion of the AlH_4 tetrahedra. This distortion together with crystal-field effects split the degeneracy of the triply degenerate T_2 levels of AlH_4^-. Overlap between molecular orbitals (MO) on neighboring AlH_4^- units splits the A_1 level at the $\mathbf{k} = 0$ point into two, separated by approximately 3 eV. Overlap descreases with increasing

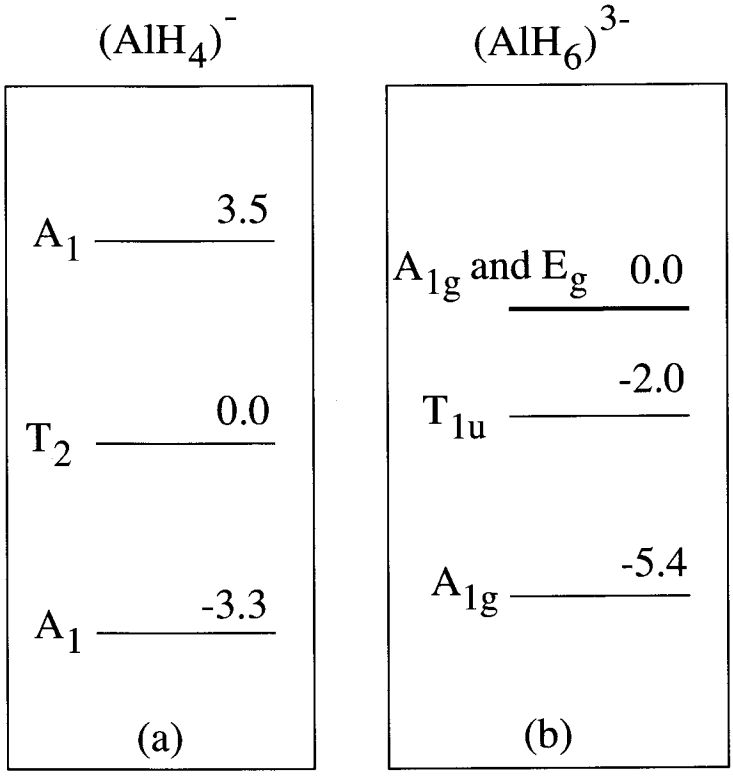

Figure 1.4: Diagram of energy levels for (a) a negatively charged tetrahedral AlH_4^- unit of T_d symmetry and (b) a triply charged octahedral AlH_6^{3-} cluster of O_h symmetry. Both clusters were embedded in a compensating background of positive charge, and the Al-H bondlengths were relaxed using the VASP code. Standard symmetry designations for the irreducible representations of T_d and O_h point groups have been adopted. A, E, and T label one-, two-, and three-dimensional irreps, respectively.

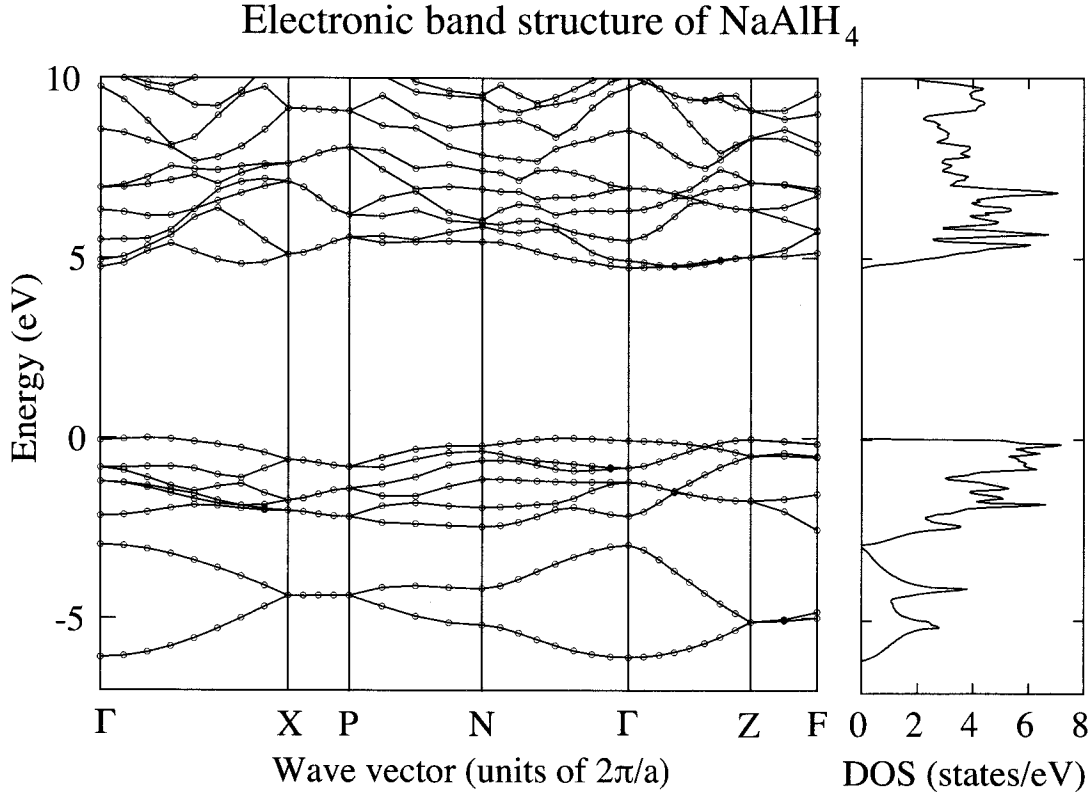

Figure 1.5: Electronic band structure of $NaAlH_4$. Special points are defined as $X = [\frac{1}{2}\frac{1}{2}0]$, $P = [\frac{1}{2}\frac{1}{2}\frac{1}{2}]$, $N = [\frac{1}{2}0\frac{1}{2}]$, $Z = [001]$, and $F = [\frac{1}{2}01]$ in units of $2\pi/a$ and $2pi/c$. Points are directly calculated eigenvalues, while the lines are interpolations that serve as guides to the eye.

$\mathbf{k}$, which is reflected in zero splitting between the two lowest valence bands near the zone boundary X and Z points. Furthermore, the overlap between neighboring A_1 and T_2 MOs appears to be small, presumably due to destructive interference caused by different symmetry properties of these MOs. The upper part of the VB consists of six bands originating from the triply degenerate T_2 states of the AlH_4^- cluster. These bands have a rather flat dispersion. The valence band maximum (VBM) lies at approximately $\mathbf{q} = [\frac{1}{4}00]$, although the energy of the Γ-point is only 50 meV below the VBM. Inspection of the calculated eigenvalues shows that there are many branches with comparable energies along other directions as well. Overall, the flatness of the $NaAlH_4$ top valence band (VB) suggests that wave function overlap between the occupied MOs on neighboring AlH_4^- units is small. Small overlap manifests itself in low hopping probabilities, resulting in heavy effective masses and low hole mobilities. $NaAlH_4$ is predicted to be an insulator with an indirect energy gap of 4.8 eV, comparable to the HOMO-LUMO gap of AlH_4^-, 3.5 eV [see Fig. 1.4(a)]. The conduction band minimum (CBM) is at the center of the Brillouin zone, $\mathbf{k} = 0$. This state is localized on the AlH_4 unit and has an appreciable charge density on the Al atom, suggesting a parentage from the LUMO A_1 state of AlH_4^-. The band dispersion around the CBM is highly anisotropic, with the effective mass being higher along $\Gamma - X$ than along the tetragonal z-direction ($\Gamma - Z$). Consequently, conduction band electron mobility is predicted to be higher in the direction perpendicular to the tetragonal axis (note, however, that the mobility is also influenced by electron-phonon and defect scattering rates, which have not been considered here). At any rate, charges are expected to be more mobile in n-doped samples than in p-doped ones, which may have implications for transformation kinetics between the $NaAlH_4$ and Na_3AlH_6 phases if the rate is limited by charge transfer.

1.6.2 Na_3AlH_6

Just like in $NaAlH_4$, the valence charge density in Na_3AlH_6, shown in Fig. 1.6, is mainly concentrated around H atoms. It also seems natural to interpret the electronic structure of Na_3AlH_6 in terms of the electronic states of an octahedral AlH_6^{3-} unit. However, the energy level diagram for an O_h-symmetric AlH_6^{3-}, embedded in a positive charge-compensating background, is more complex [see Fig. 1.4(b)]. The lowest occupied MO is a completely symmetric A_{1g} state, formed by a linear combination of s orbitals on H sites. It is followed by a triply degenerate T_{1u} state; physically, it corresponds to a combination of H $1s$ functions of the following type: $\frac{1}{\sqrt{2}}[\psi_{1s}(x-a) - \psi_{1s}(x+a)]$, and correspondingly for y and z. Higher up, a singlet A_{1g} level and a doubly degenerate E_g level are found to be very close in energy. In fact, it was impossible to achieve self-consistency assuming integer occupation numbers, since they oscillated between 0 and 1 as the order of these states reversed depending upon which level was occupied. Use of fractional occupation numbers with a Fermi-Dirac distribution corresponding to $T = 20$ meV was required to damp

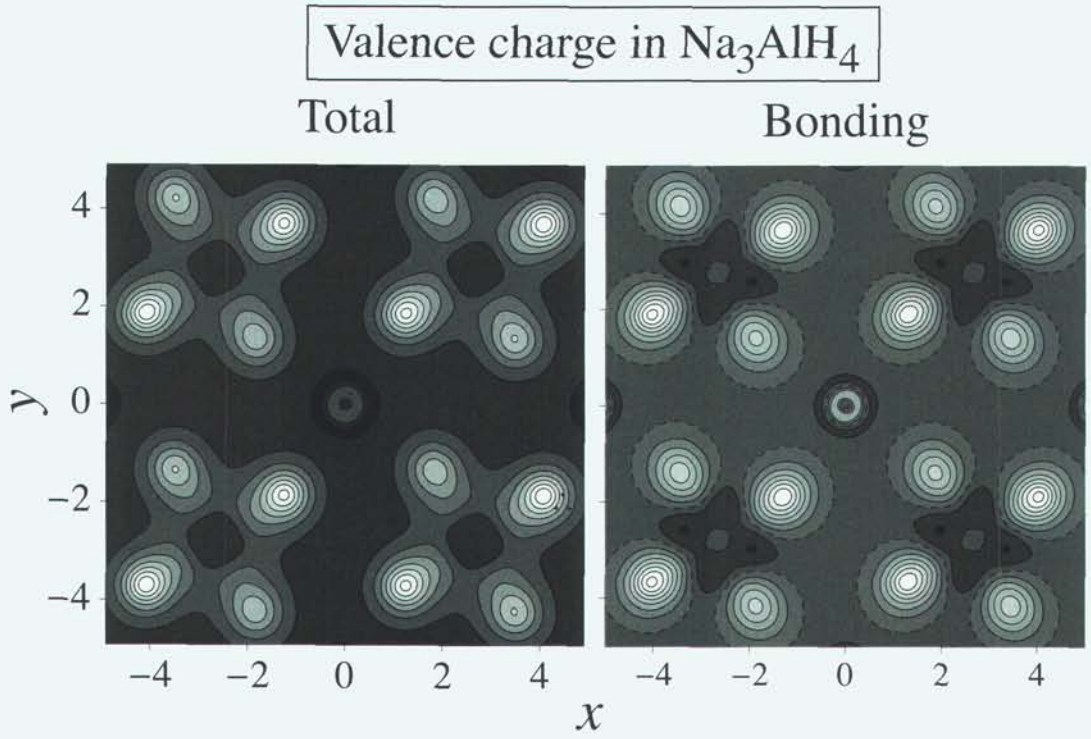

Figure 1.6: *Left:* Valence charge density of Na_3AlH_6 in the plane defined a and b latice vectors and going through Al and Na atoms at 2(a) and 2(b) sites, respectively. The highest density contour corresponds to 175 electrons/Å^3, and the spacing between successive contour levels is 25 electrons/Å^3. *Right:* Bonding charge density $\rho_{\rm bond}$, defined as a difference between the self-consistent valence charge density (shown on the left) and the charge density obtained by overlapping free-atom charges, $\rho_{\rm bond} = \rho_{\rm val} - \rho_{\rm overlap}$. Zero level is shown by a dashed line; the contour spacing is 8 electrons/Å^3. Like in Fig. 1.3, charge transfer from Al and Na to H ions is evident.

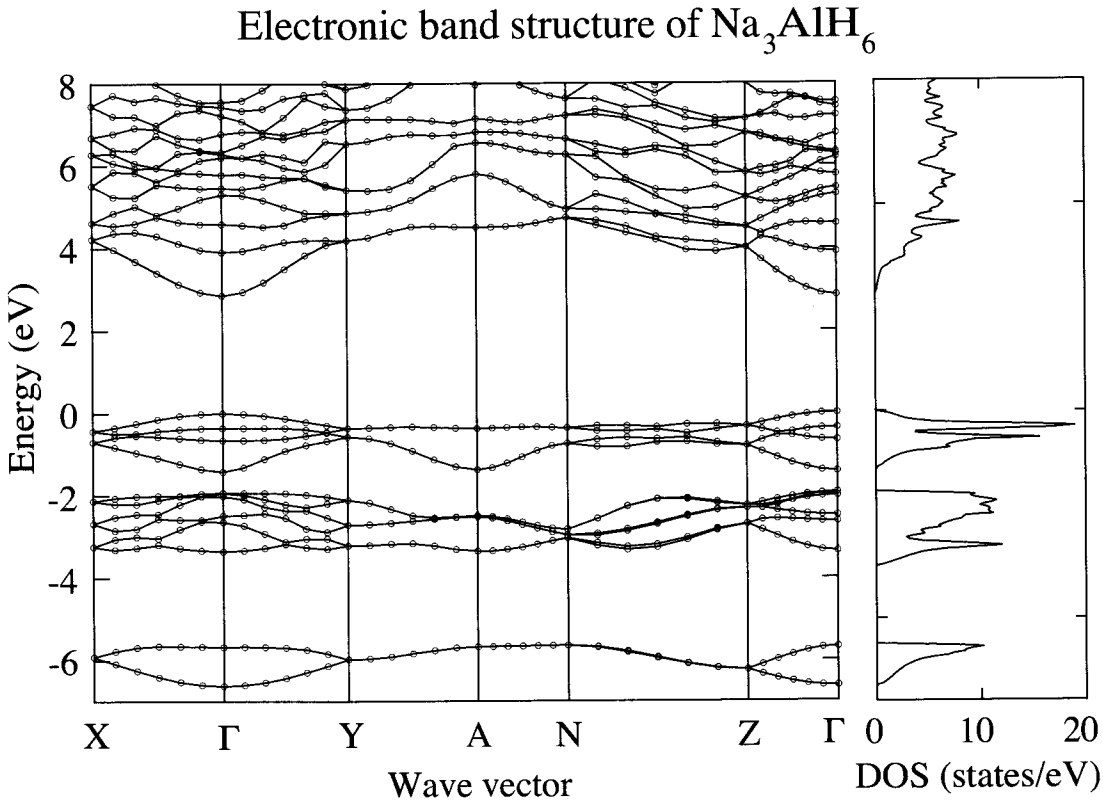

Figure 1.7: Electronic band structure of Na_3AlH_6. Special points are defined as $X = [\frac{1}{2}00]$, $Y = [0\frac{1}{2}0]$, $A = [\frac{1}{2}\frac{1}{2}0]$, $N = [\frac{1}{2}\frac{1}{2}\frac{1}{2}]$, and $Z = [00\frac{1}{2}]$ in units of the reciprocal lattice basis vectors. Points are directly calculated eigenvalues, while the lines are interpolations that serve as guides to the eye.

out these oscillations. Presence of degenerate states at the Fermi level causes the cluster to undergo a symmetry-breaking Jan-Teller distortion if the O_h symmetry constraints are removed. For an isolated AlH_6^{3-} cluster this distortion results in a huge rearrangement of H atoms, which destroys any resemblance to an octahedron. In Na_3AlH_6, well-defined octahedral AlH_6 units exist, which raises the question of which physical effects are responsible for their stabilization. There are two obvious possibilities. First, the local site symmetry in Na_3AlH_6 is much lower than O_h, leading to a sizeable distortion of the AlH_6 octahedron. It is intuitively appealing to think that this structural distortion could remove the degeneracy at the Fermi level and stabilize the structure. Indeed, if the energy levels of AlH_6^{3-} are recalculated using the H positions from Na_3AlH_6, one finds that the degeneracy between A_{1g} and E_g levels is lifted and a well-defined HOMO-LUMO gap of approximately 2 eV is opened. Second, electrostatic interactions with Na^+ ions and other AlH_6^{3-} units also play a key role in stabilizing the octahedral structure of AlH_6 groups.

The band structure of Na_3AlH_6 is shown in Fig. 1.7. It is characterized by two low-lying bands originating from the A_{1g} level of AlH_6^{3-}, followed by a six-band complex derived from the triply degenerate T_{2g} states. Finally, the top two-band complex can be traced back to the A_{1g} and E_g states in Fig. 1.4. Overall, the energy bands of Na_3AlH_6 are much flatter than those of $NaAlH_4$, which is a reflection of the much larger separation between the AlH_6 units in the latter. The material is predicted to be a direct-gap insulator with an energy gap of 2.5 eV. The effective mass of holes is predicted to be significantly higher than the effective mass of conduction band electrons. Therefore, the carrier mobility will be higher in n-doped than in p-doped materials. Just like in $NaAlH_4$, the CBM state has its charge density near the Al atom, i.e. it too is quasi-localized on the AlH_6 group.

1.6.3 Electrostatic interactions

Understanding of the factors that determine crystal binding energies of hydrogen-light-metal compounds is useful for developing new materials with thermodynamic properties that are tailored for room-temperature hydrogen storage and extraction. Due to their highly ionic nature, electrostatic energy plays a major role in determining the structural stability of $NaAlH_4$ and Na_3AlH_6. In what follows, we point out an interesting analogy with a simple electrostatic alloy model on a fixed face-centered cubic lattice (fcc). This analogy provides interesting insight into how the electrostatic energy influences structural preferences of alanates. First, the charge density plots in Figs. 1.3 and 1.6 suggest that both alanates can be thought of as composed of positively charged Na^+ ions and negatively charged clusters of AlH_{3+n}^{n-} (where $n = 1$ or 3 for $NaAlH_4$ or Na_3AlH_6, respectively). Furthermore, within the AlH_{3+n}^{n-} clusters most of the electronic charge is concentrated around H ions, while Al is largely stripped of its valence electrons. This suggests that electrostatic interactions contribute significantly to the overall binding energies of $NaAlH_4$ and

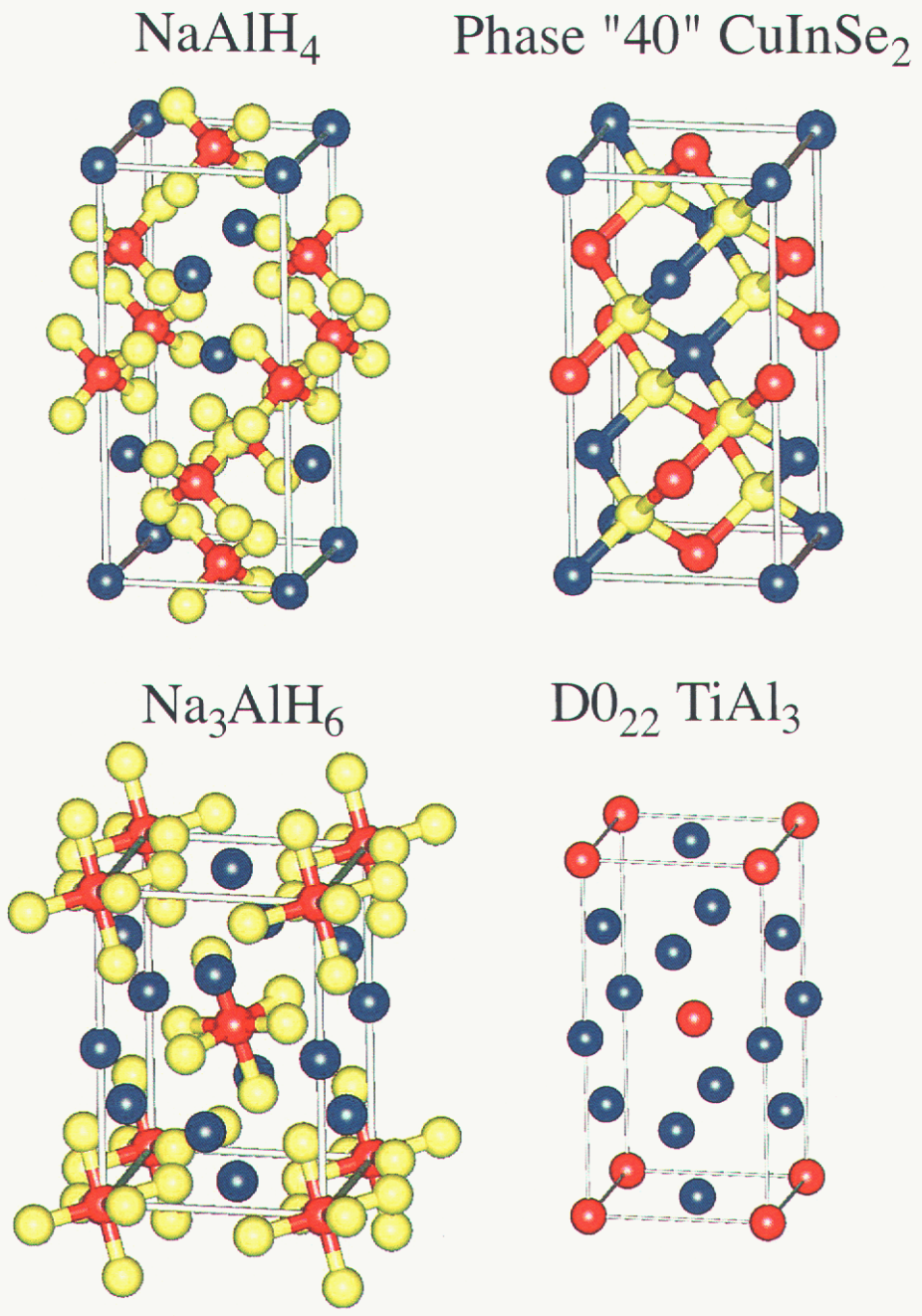

Figure 1.8: Crystal structures of $NaAlH_4$ (top left) and Na_3AlH_6 (bottom left), compared with the ordered chalcopyrite (top right, prototype $CuInSe_2$) and $D0_{22}$ (bottom right, prototype $TiAl_3$) phases. Notice that the red and blue ions occupy the vertices of an fcc lattice in all four structures shown, and their arrangement is the same in $NaAlH_4$ and chalcopyrite, and Na_3AlH_6 and $D0_{22}$, respectively. For both $NaAlH_4$ and Na_3AlH_6, origin has been shifted away from the high-symmetry positions adopted in Tables 1.2 and 1.3 to emphasize similarity with the fcc-based structures on the right.

Na_3AlH_6. Second, examination of crystal structures of $NaAlH_4$ and Na_3AlH_6, (see Fig. 1.8) shows that in both compounds Al and Na ions occupy the vertices of a lattice that is a slightly distorted form of fcc. In other words, there is a one-to-one correspondence between the fcc sites and Na and Al sites in alanates. In alanates, ions are displaced from the ideal fcc sites and the unit cell is distorted according to the lower non-cubic symmetry group of the compound, determined by the arrangement of Al and Na atoms and by the orientation of AlH_m units. Thus, both alanates can be thought of as binary fcc-based AB_n compounds, where A =AlH_{3+n}^{n-}, B=Na^+, and $n = 1$ ($n = 3$) for $NaAlH_4$ (Na_3AlH_6), held together by long-range electrostatic interactions and hard-core repulsion at short distances. The ground states of fcc-based electrostatic alloy models as functions of n are well known.[29] The lowest energy state at the 50-50 composition, corresponding to $n = 1$, is a tetragonal structure known as phase "40" (prototype structure is zincblende-based chalcopyrite compound $CuInSe_2$), while at the 25-75 composition the lowest electrostatic energy is achieved in the tetragonal $D0_{22}$ structure (prototype $TiAl_3$). It is predicted that $D0_{22}$ and "40" are the only ground states of an fcc-based alloy with purely electrostatic interactions.[29] Inspection of the Na and Al positions in Fig. 1.8 shows that their arrangement in $NaAlH_4$ is the same as that of the cations in the chalcopyrite structure, while in Na_3AlH_6 it is the same as in the $D0_{22}$ structure!

The preceding analysis points to the dominance of lattice electrostatics in selecting the most favorable arrangement of AlH_m groups and Na ions. However, it still leaves open the questions of why do AlH_n and Na arrange on the sites of an fcc-like lattice? For instance, it is well known that the Madelung energies of CsCl- and NaCl-type structures are lower than those of any others; this is confirmed by the fact that many binary ionic compounds adopt one of these simple (non-fcc based) structures. The chalcopyrite structure is encountered in many ternary semiconductors, but the structurally isomorphic phase "40", obtainable from the chalcopyrite structure by removing all anions, is almost never encountered in simple fcc-based alloys. We propose that the crystal structures of $NaAlH_4$ and Na_3AlH_6 may be a consequence of the nonspherical nature of the AlH_4 unit, which makes it energetically preferable to position H^- ions in the vicinity of Na^+. This is efficiently achieved in $NaAlH_4$, while the six-fold coordination of NaCl and eight-fold coordination of CsCl may be incompatible with the tetrahedral structure of AlH_4. However, the full quantum-mechanical energy represents a delicate balance between many kinds of bonding ineractions, and these considerations should be taken with a good measure of caution.

1.7 Conclusions

A Rietveld refinement was performed on a phase mixture of Ti-doped $NaAlD_4$ and Na_3AlD_6 and compared to previously reported structural refinements of undoped single crystal $NaAlH_4$ and powdered Na_3AlD_6 and $NaAlD_4$. Refined deuterium

atom positions put the Al-D bond length 1–2 % larger than the Al-H bond length reported previously with no other significant changes from the $NaAlH_4$ crystal structure. Results of first principles calculations for $NaAlH_4$ were compared to refined experimental data for $NaAlD_4$. The lattice geometries and reaction enthalpies determined using the generalized gradient approximation reflect the experimentally determined values more accurately than the ones obtained using the local-density approximation. The valence bands of $NaAlH_4$ (Na_3AlH_6) are found to be formed by overlapping MOs of charged AlH_4^- (AlH_6^{3-}) clusters of T_d (O_h) symmetry. Both compounds exhibit very flat valence bands and substantial band gaps of 4.8 and 2.5 eV, respectively. Effective masses of the conduction band states are predicted to be substantially lower than those of the valence band, pointing to faster charge transport in n-doped alanates. Bonding in both alanates is of polar covalent type with most of the electronic charge on H ions. Na atoms are almost entirely stripped of their valence $3s$ electrons. We also point out an interesting analogy between the crystal structures of $NaAlH_4$ and Na_3AlH_6 and the ground states of an electrostatic alloy model on an fcc lattice, which allows us to rationalize the crystal structure of $NaAlH_4$ (Na_3AlH_6) in terms of electrostatic interactions between charged AlH_4^- (AlH_6^{3-}) groups and Na^+ ions.

1.8 Acknowledgments

This work was funded by the U.S. Department of Energy, Office of Power Technologies, Hydrogen Program Office under contract No. DE-AC36-83CH10093. The authors thank Andrés Orozco for preparation of the pre-deuterated material.

Bibliography

[1] B. Bogdanovic, R.A. Brand, A. Marjanovic, M. Schwickardi, and J. Tolle. *J. Al. Comp.*, 302(1-2):36 – 58, April 2000.

[2] G. Sandrock, K. Gross, G. Thomas, C. Jensen, D. Meeker, and S. Takara. *J. Al. Comp.*, 330-332:696 – 701, January 2002.

[3] A. Zaluska, L. Zaluski, and J.O. Strom-Olsen. *Journal of Alloys and Compounds*, 298(1-2):125 – 34, February 2000.

[4] C.M. Jensen, R. Zidan, N. Mariels, A. Hee, and C. Hagen. *Int. J. Hyd. En.*, 24(5):461 – 5, May 1999.

[5] Dalin Sun, T. Kiyobayashi, H.T. Takeshita, N. Kuriyama, and C.M. Jensen. *J. Al. Comp.*, 337:L8 – 11, May 2002.

[6] K.J. Gross, E.H. Majzoub. *Proceedings of the International Symposium on Metal Hydrogen Systems*, Annecy, France, 2-6 Sept. 2002, Submitted Sept. 2002.

[7] V.K. Bel'skii, B.M. Bulychev, and A.V. Golubeva. *Russ. J. Inorg. Chem.*, 28(10):1528, 1983.

[8] J.W. Lauher, D. Dougherty, and P.J. Herley. *Acta Cryst.*, B35(pt.6):1454 – 6, June 1979.

[9] B. Bogdanovic, M. Schwickardi. *J. Al. Comp.*, 253-254, 1997.

[10] B. Bogdanovic, M. Felderhoff, M. Germann, M. Härtel, A. Pommerin, F. Schüth, C. Weidenthaler. *J. Al. Comp.*, 350, 2003.

[11] K.J Gross and E.H. Majzoub. Direct synthesis of light-weight catalyzed hydride for hydrogen storage. United States patent application submitted 2002.

[12] H. Ritter, J. Ihringer, J.K. Maichle, and W. Prandl, *Simultaneous Structure Refinement with Multiple Powder Diffraction Data Sets.* Institute für Kristallographie der Universität Tübingen, Charlottenstr. 33, D-72070 Tübingen, 1998. Version 2.6.

[13] E.H. Majzoub, K.J. Gross. *Proceedings of the International Symposium on Metal Hydrogen Systems*, Annecy, France, 2-6 Sept. 2002, Submitted Sept. 2002.

[14] E. Rönnebro, D. Noreus, K. Kadir, A. Reiser, and B. Bogdanovic. *J. Al. Comp.*, 299(1-2):101 – 6, March 2000.

[15] A.C. Larson and R.B. von Dreele, *General Structural Analysis System Technical Manual.* Los Alamos National Laboratory, 2000 Report No. LAUR 86-748

[16] R.J. Hill and H.D. Flack, J. Appl. Cryst. **20**, 356-361 (1987); R.J. Hill and C.J. Howard, J. Appl. Cryst. **20**, 467-474 (1987).

[17] G. Kresse and J. Hafner, Phys. Rev. B **47**, 558 (1993); J. Phys. Condens. Matter **6**, 8245 (1994).

[18] G. Kresse and J. Furthmüller, Comput. Mater. Sci. **6**, 15 (1996); Phys. Rev. B **54**, 11169 (1996).

[19] G. Kresse, Ph. D. Thesis, Technische Universität Wien 1993.

[20] D. Vanderbilt, Phys. Rev. B **41**, 7892 (1990).

[21] S. Louie, S. Froyen, and M. L. Cohen, Phys. Rev. B **26**, 1738 (1982).

[22] J. P. Perdew and A. Zunger Phys. Rev. B **23**, 5048 (1980).

[23] J. P. Perdew, in *"Electronic Structure of Solids 1991"*, edited by P. Ziesche and H. Eschrig (Akademie Verlag, Berlin, 1991), Vol. 11.

[24] H. J. Monkhorst and J. D. Pack. Special points for Brillouin-zone integrations. *Physical Review B* **13**, 5188-5192 (1976).

[25] V. Ozoliņš, E. Majzoub, and T. Udovic, unpublished (2002).

[26] G.J. Thomas, S.E. Guthrie, K.J. Gross. *Proceedings of the 1999 DOE Hydrogen Program Annual Peer Review*, NREL/CP-570-26938.

[27] W.M. Mueller, J.P. Blackledge, G.G. Libowitz. *Metal Hydrides*, Chapter 6, Academic Press, New York and London, 1968.

[28] B.C. Hauback, H.W. Brinks, C.M. Jensen, K. Murphy, A.J. Maeland. *J. Al. Comp.*, in press.

[29] C. Wolverton and A. Zunger, Phys. Rev. B **51**, 6876 (1995).

Chapter 2

XRD and NMR investigation of Ti-compound formation in solution-doping of sodium aluminum hydrides: Solubility of Ti in $NaAlH_4$ crystals grown in THF.

E.H. Majzoub[a1], R. Stumpf[a], S. Spangler[a]
[a]Sandia National Laboratories
P.O. Box 969, Livermore, CA, 94551 USA

J.L. Herberg[b], R.S. Maxwell[b]
[b]Lawrence Livermore National Laboratories
P.O. Box 808, Livermore, CA, 94551 USA

Abstract

Sodium aluminum hydrides have gained attention due to their high hydrogen weight percent (5.5% ideal) compared to interstitial hydrides, and as a model for hydrides with even higher hydrogen weight fraction. The purpose of this paper is to investigate the Ti-compounds that are formed under solution-doping techniques, such as wet doping in solvents such as tetrahydrofuran (THF). Compound formation in Ti-doped sodium aluminum hydrides is investigated using x-ray diffraction (XRD) and magic angle spinning (MAS) nuclear magnetic resonance (NMR). We present lattice parameter measurements of crushed single crystals, which were exposed to Ti during growth. Rietveld refinements indicate no lattice parameter change and thus

no solubility for Ti in $NaAlH_4$ by this method of exposure. In addition, x-ray diffraction data indicate that no Ti substitutes in NaH, the final decomposition product for the alanate. Reaction products of completely reacted (33.3 at. %-doped) samples that were solvent-mixed or mechanically milled are investigated. Formation of $TiAl_3$ is observed in mechanically milled materials, but not solution mixed samples, where bonding to THF likely stabilizes Ti-based nano-clusters. The Ti in these clusters is activated by mechanical milling.

2.1 Introduction

The decomposition of sodium alanate was first shown to be kinetically enhanced and reversible by Bogdanovic and coworkers by the addition of Ti-dopant [1, 2]. The decomposition proceeds as

$$NaAlH_4 \rightarrow \frac{1}{3}Na_3AlH_6 + \frac{2}{3}Al + H_2 \rightarrow NaH + Al + \frac{3}{2}H_2 \quad , \tag{2.1}$$

where the aluminum is known to agglomerate into bulk form, which is easily visible in x-ray diffraction of decomposed material. The rate of these reactions is enhanced by several orders of magnitude by the addition of a Ti-dopant, which lowers the activation energy of the absorption and desorption processes [3]. However, the way in which the Ti-dopant works is still not understood [4, 5]. The location of dopant Ti in sodium alanate has become the leading question in the study of this complex-hydride system. Identifying the compounds in which the Ti is located after the doping procedure may help to explain the enhanced reaction kinetics.

There is some evidence to suggest that Ti may substitute in the alanate structure resulting in lattice parameter changes upon doping through mechanical milling [6]; however, the absence of a lattice parameter standard in this study casts doubt on the validity of the results obtained. In addition, others have been unable to produce similar results [5]. Upon heating and decomposition of Ti-doped samples, a shoulder in the x-ray spectrum is observed in prominent aluminum reflections, and has been interpreted as Ti incorporation into bulk Al [7]. This suggests, with the Ti-Al binary phase diagram and the fact that Ti-Al line compounds have favorable formation energies, that Ti-Al compounds are likely to form in this system [4].

There is a striking difference in hydrogen sorption rates when doping through different techniques. For example, mechanically milling Ti-halide dopants with $NaAlH_4$ powder results in rapid initial kinetics, while the same milling with TiH_2, or $TiAl_3$ as a dopant results in very slow initial kinetics. However, it has been shown that samples prepared through mechanical milling of $NaAlH_4$ and TiH_2 show hydrogen absorption rates that increase upon cycling from extremely poor, to rates comparable to doping with Ti-halides [8]. Doping with Ti nano-clusters has been demonstrated and results in faster absorption reaction kinetics than doping with Ti-halides [9, 10].

The Ti nano-clusters in the work of Fichtner, *et al..*, and Bogdanovic, *et al..*, were prepared in solutions of tetrahydrofuran (THF).

In this paper, we (1) demonstrate that no lattice parameter changes are seen in $NaAlH_4$ crystals grown in saturated solutions of THF, (2) show that lattice parameter changes seen in NaH, when doping with TiF_3 are due to flourine substitution in the NaH lattice, and (3) indicate the differences between some of the compounds formed in solvent-free production of active materials, and those prepared through $TiCl_3$ doping in THF. Samples prepared by doping in THF did not show hydrogen sorption activity unless mechanically milled. This information may help to indicate the nature of the compounds which are active by different doping procedures.

Growth of large crystals (of order 0.5 mm) of $NaAlH_4$ was performed for our x-ray study because small changes in structure factors are more likely to be observable in well ordered crystals as opposed to the more pragmatic mechanically milled materials. In addition, mechanical milling is known to produce metastable structures, and we were interested in determining ground state structures of Ti substitution defects, if they were present.

2.2 Experimental Details

The samples prepared for this work are listed in Table (4.1). Single crystal samples of $NaAlH_4$ were grown by solvent evaporation from *Sigma Aldrich* 1 M solutions of $NaAlH_4$ in THF. These samples are referred to as "pure-$NaAlH_4$", or (S_1). *NIST* powdered silicon was added as lattice constant standard for x-ray diffraction refinements. Samples referred to as "Ti-exposed," or (S_2), were prepared like the pure single crystals, but with $TiCl_3$ added to the solution. The $TiCl_3$ was added at 4 at. %, with respect to the amount of alanate in solution, before the solvent evaporation. The single crystal samples were crushed by hand in a mortar and pestle for diffraction and NMR spectra. Alternatively to (S_2) samples, rapidly dried 4 at. % doped samples, prepared in THF, resulted in fine powders and are referred to as (S_{3a}). Samples of (S_{3a}) were also mechanically milled for some sorption experiments, and are referred to as (S_{3b}).

In addition, 33.3 at. % doped samples ($3\,NaAlH_4 + TiCl_3$) were prepared. This ratio was chosen so that all of the alanate would be consumed leading to larger quantities of reaction products. Samples prepared for study are referred to as 33.3 at. % doped "solvent" (S_4) and "solvent-free" (S_5). The solvent-free samples were prepared by mechanical milling of $NaAlH_4$ powder and $TiCl_3$ powder in a SPEX mill as described elsewhere [4]. The solution-mixed samples were prepared in THF in an argon-filled dry box by the addition of 0.257 g of $TiCl_3$ to 5 cc of 1 M $NaAlH_4$ in THF, which was allowed to evaporate at room temperature in an argon dry box.

X-ray diffraction was performed using Cu-K_α radiation on a *Scintag* XDS-2000 using Bragg-Brentano geometry and airless sample holders, using a step size of 0.02 ° 2θ, and a count time of 0.5 s. X-ray fluorescence spectra were collected on a KEVEX

Sample	Solvent	Dopant	at. %	Form	Milled	Phases Present
S_1	THF	none	0	crushed crystal	no	$NaAlH_4$
S_2	THF	$TiCl_3$	4	crushed crystal	no	$NaAlH_4$
S_{3a}	THF	$TiCl_3$	4	fine powder	no	$NaAlH_4$, Na_3AlH_6, Al, NaCl
S_{3b}	THF	$TiCl_3$	4	fine powder	yes	not examined
S_4	THF	$TiCl_3$	33	fine powder	no	Al, Al_2O_3, NaCl
S_5	none	$TiCl_3$	33	fine powder	yes	Al, $TiAl_3$, NaCl

Table 2.1: Samples used in this work.

Omicron using a Cu x-ray source operated at 50 kV and 1 mA, with a 50 μm aperture and 100 sec collection time.

Hydrogen sorption experiments were performed on sample sizes of about 2 g, which were transferred to a sealed stainless-steel sample vessel and connected to a pressure, and temperature-controlled hydrogen manifold. All steps for sample preparation and transfer into the reactor vessel occurred inside an Ar glove box with oxygen levels below 3 ppm.

MAS NMR measurements were performed on a Bruker Avance 400WB spectrometer with a magnetic field of 9.4 T. This gives a resonance frequency of 104.25 MHz for ^{27}Al (spin $\frac{5}{2}$) and 105.84 MHz for ^{23}Na (spin $\frac{3}{2}$). The samples were packed in 4 mm MAS rotors inside an Ar glove box with oxygen levels below 3 ppm. Spinning rates of 9 kHz and 12 kHz were used. The Free Induction Decay (FID) spectra were taken with a single excitation pulse. For both ^{27}Al and ^{23}Na NMR, a short pulse and small flip angle was used (^{27}Al MAS NMR with a 8 degree pulse width of 0.2 μs and ^{23}Na MAS NMR with a 8 degree pulse width of 0.2 μs). The ^{27}Al spectra were referenced to aqueous solutions of $Al(NO_3)_3$ and ^{23}Na was referenced to aqueous solutions of $NaNO_3$.

2.3 Rietveld Refinements of pure and Ti-exposed $NaAlH_4$

The lattice parameters of undoped and 4 at. % Ti-exposed single crystals, samples (S_1) and (S_2), were determined by Rietveld refinement of x-ray diffraction from gently powdered samples using SIMREF 2.6 [11]. Peak shapes of the x-ray data were fit using the pseudo-Voigt profile containing a mixture of Gaussian and Lorentzian line shapes, as shown in Figure (2.1). The Bragg residuals for $NaAlH_4$ for the pure and Ti-exposed samples were 14% and 6.8%, respectively. Overall refinement residuals, including the silicon peaks are shown in Table (2.2). The definition of the residuals R_p, R_{wp}, R_e, and R_{Bragg}, can be found in the SIMREF technical manual [11]. The lattice constants from the fit to the Ti-exposed sample yielded $a = 5.0238$ Å and $c = 11.3506$ Å. The lattice constants from a pure $NaAlH_4$ crushed single crystal

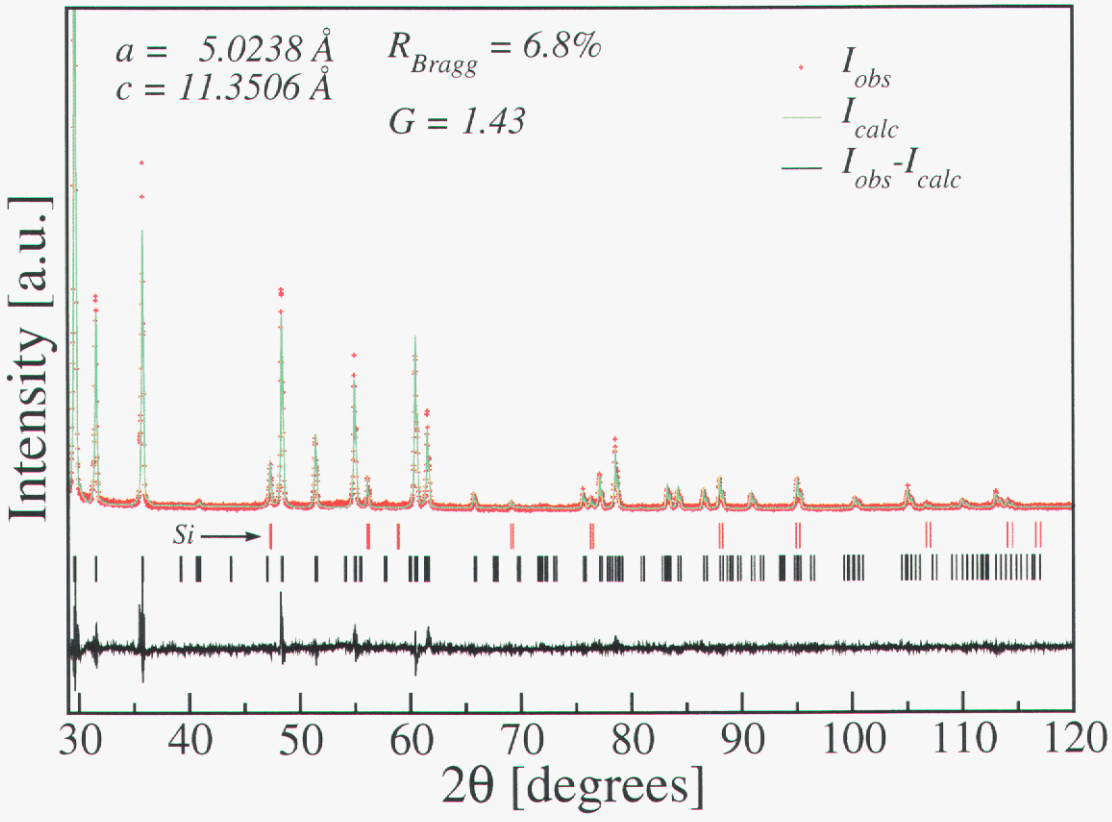

Figure 2.1: Rietveld refinement of Ti-exposed crushed single crystals (S_2). The lattice parameters show no change within 0.0002 Å from pure $NaAlH_4$, suggesting that no titanium is introduced into the lattice with this method of doping.

yeilded $a = 5.0238\,\text{Å}$ and $c = 11.3504\,\text{Å}$, indicating that there is no observable shift in the lattice constants due to the exposure of Ti *by this method.* If we assume that Ti substitution would shift the lattice paramters, therefore Ti appears to be essentially insoluble in $NaAlH_4$. These results are in agreement with total energy calculations indicating that Ti substitution on Na or Al sites is energetically unfavorable in perfect $NaAlH_4$ at realistic chemical potentials [12].

Table 2.2: Lattice parameters and overall refinement residuals for the refinements of pure and Ti-exposed $NaAlH_4$.

Data Set	a [Å]	c [Å]	R_p	R_{wp}	R_{exp}	$(N-P)$	S
pure	5.0238	11.3504	0.143	0.184	0.120	5051	1.59
Ti-exposed	5.0238	11.3506	0.126	0.170	0.120	5049	1.43

Our measurements also suggest that Ti does not substitute in NaH, the final hydride decomposition product in Eq. (2.1). X-ray diffraction of annealed samples of NaH, mechanically milled with $TiCl_3$, show no lattice parameter changes in diffraction data greater than 0.04 %. However, lattice parameter changes of the NaH observed upon mechanical mixing of TiF_3 and NaH were observed, and are consistent with fluorine substitution in the NaH lattice, as the lattice parameter shifts linearly between bulk NaH and bulk NaF, as shown in Figure (2.2). This is in contrast to doping with Cl-containing compounds, where NaCl is evidenced even at small doping levels.

2.4 Compound formation in 33.3 at. % Ti-doped $NaAlH_4$

In order to determine the possible structures in which Ti may be residing, the dopant level was increased to a large enough value that all the available alanate is consumed, leaving only NaCl, and Ti-Al-H reaction products. X-ray diffraction of mechanically milled samples of 33.3 at. % doped material (S_5) indicate that $TiAl_3$ formation is likely [4]. However, the same dopant ratio applied in a solution of THF (S_4) shows no indication of $TiAl_3$. X-ray diffraction in Figure (2.3a) shows that no bulk Ti or $TiAl_3$ is formed in solution mixing of $NaAlH_4$ and $TiCl_3$. The only observed peaks in our experiments correspond to bulk Al, and NaCl. The presence of Ti is clearly indicated in x-ray fluorescence of the solution-mixed sample, despite the absence of any indication of bulk (hcp) Ti or $TiAl_3$ in x-ray diffraction. There is an indication of an amorphous or low coherence length phase in the x-ray spectrum between 15-40 degrees 2θ, shown as a very broad increase in the background intensity in the inset to Figure (2.3b). The Scherrer particle size equation yields a calculated coherence length of about 7 Å from the FWHM of this background intensity.

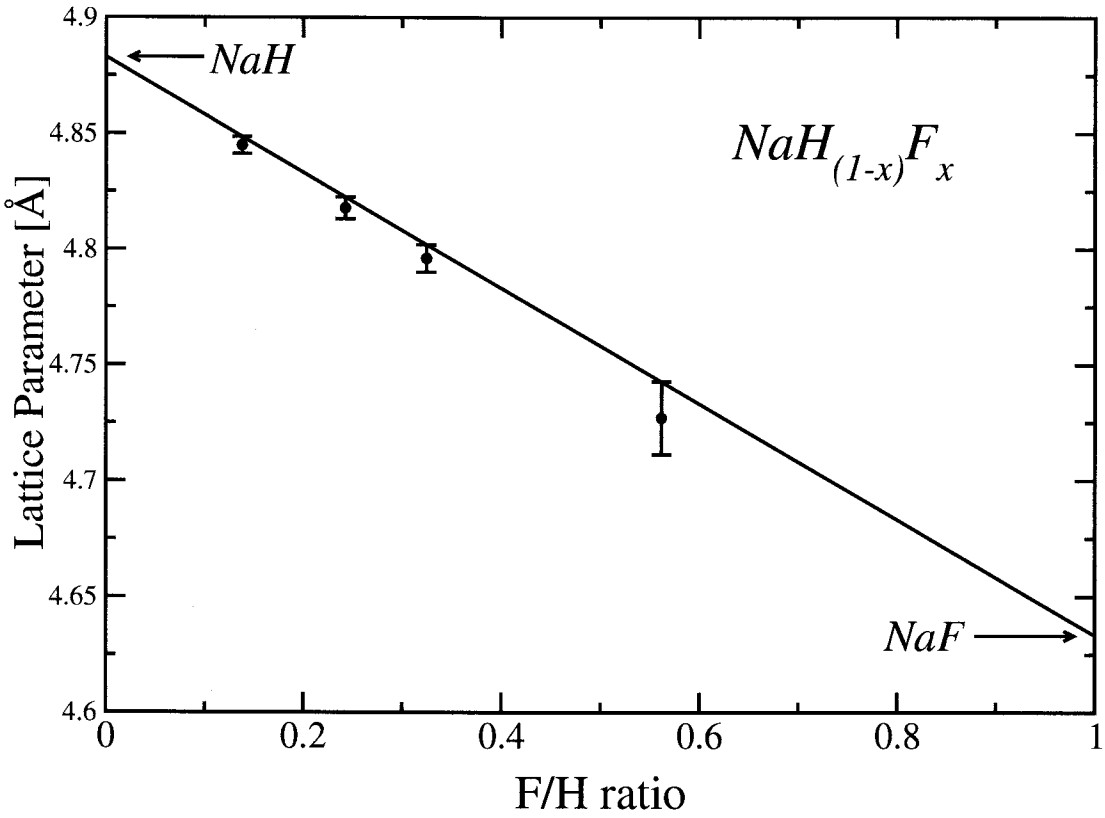

Figure 2.2: Lattice parameter of annealed NaH after mechanical milling with TiF_3, where the F/H ratio is given on the x-axis. The lattice parameter shifts linearly from that of NaH toward NaF with increasing F content.

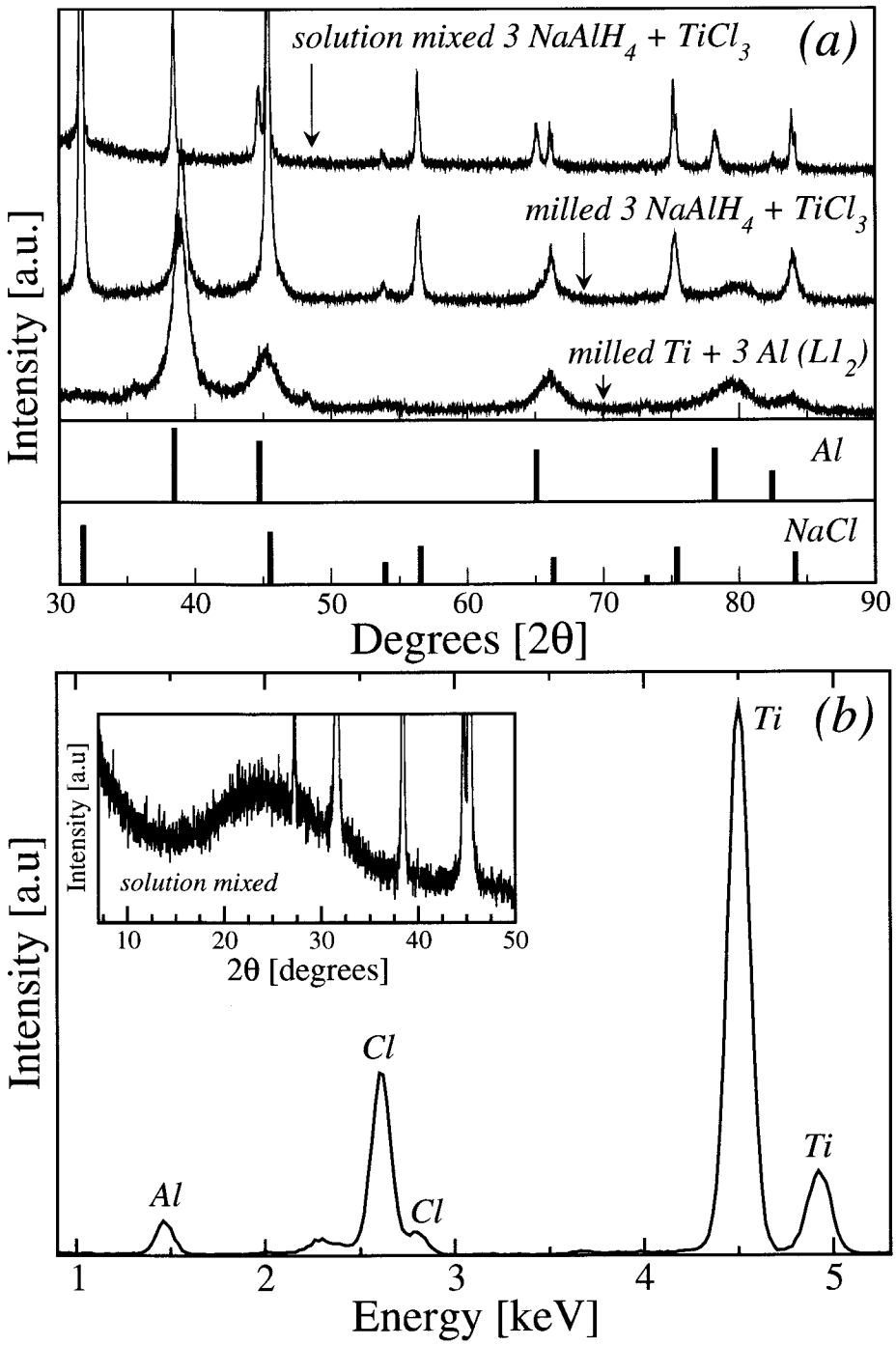

Figure 2.3: X-ray diffraction (a) of THF solution-mixed, and mechanically-milled $3\,NaAlH_4 + TiCl_3$. Metastable $TiAl_3$, in the $L1_2$ structure is shown for reference. Diffraction data shows no Ti-compounds, but the presence of Ti in the material is evidenced by the clear XRF signal (b), which, together with the inset XRD showing a wide peak of intensity at low angle, indicates the presence of Ti in either nano-particle or amorphous compounds.

Some of the possible reactions occurring in the THF solvent include:

$$TiCl_3 + 3\,Na^+ + 3\,(AlH_4)^- \longrightarrow TiAl_3 + 3\,NaCl + 6\,H_2 \quad (2.2)$$

$$TiCl_3 + 3\,Na^+ + 3\,(AlH_4)^- \longrightarrow TiH_2 + 3\,NaCl + 3\,Al + 5\,H_2 \quad (2.3)$$

$$TiCl_3 + 3\,Na^+ + 3\,(AlH_4)^- \longrightarrow [Ti_{1-y}Al_y \cdot 0.5\,THF]_x + 3\,NaCl + (3-y)\,Al + 6\,H_2 \quad (2.4)$$

The free energies of formation for some Ti-Al and Ti-H compounds are shown in Table (2.3). The difference in Gibbs' free energy for reactions (2.2) and (2.3) is about 50 kJ/mol, favoring the formation of $TiAl_3$. Therefore, in the solvent-mixed samples,

Compound	ΔG_f° [kJ/mol]
TiAl	-72
TiH_2	-86
$TiAl_3$	-136
Al_2O_3	-1582
TiO_2	-889

Table 2.3: Formation energies for possible Ti-Al-H compounds.

the Ti may form an unknown $TiAl_xH_y$ compound, or a $Ti_{(1-y)}Al_y$ nano-particle colloid, due to the similarity in the solution reactions used to produce the Ti nano-particles in the work of Bogdanovic and Fichtner [10, 9]. Three experimental results suggest the latter. First, the presence of hydrogen is indicated by proton NMR in the solvent mixed samples, suggesting that residual THF may be present. Second, the sorption kinetics of the 4 at. %-doped samples (S_{3a}) and (S_{3b}), solution-mixed in THF, indicate that mechanical milling of the samples was required for activity, in agreement with the work of Bogdanovic and Fichtner [10, 9]. The sample not milled after evaporating the THF was initially desorbed at 160 °C into a vacuum, releasing 53 % of its reversible hydrogen over a 1.5 hr period. A subsequent absorption showed no hydrogen uptake, over a 2 hr period, at pressures up to 82 bar at a temperature of about 95 °C. In contrast, the sample which was mechanically milled after drying, desorbed about 73 % of its reversible hydrogen over a 1.5 hr period at 160 °C. A subsequent absorption of the milled sample at about 85 °C and 85 bar over 2 hrs indicated an absorption of over 90 % of the hydrogen which was initially desorbed. Finally, x-ray diffraction and ^{27}Al NMR data show bulk Al, not TiAl or $TiAl_3$.

^{27}Al MAS NMR spectra of the four doped $NaAlH_4$ materials are shown in Figure (2.4), with peak positions given in Table (2.4). The spectra for sample (S_2) shown in Figure (2.4a), is characterized by a peak at 94.6 ppm due to $NaAlH_4$. The spectrum of sample (S_{3a}) shown in Figure (2.4b) is characterized by three distinct ^{27}Al NMR resonances: one at 1640 ppm, assigned to metallic aluminum; one at approximately -42.6 ppm, assigned to Na_3AlH_6; and one at 94.2 ppm, assigned to $NaAlH_4$. These assignments were made based on comparisons to pure materials (data not shown), and previous findings on similar materials [5]. The ^{27}Al MAS

spectra for samples (S_4) and (S_5) are shown in Figures (2.4c) and (2.4d), respectively. It is clear from the ^{27}Al MAS NMR spectra that the aluminum speciation is dramatically affected by the processing methods. Sample (S_4) has two distinct peaks: metallic aluminum at 1641 ppm and a series of overlapping resonances at 8.4 ppm, 35.5 ppm, and 63.6 ppm, assigned to six, five, and four coordinate aluminum-oxygen species, respectively, in Al_2O_3 [13]. To confirm that this peak did not represent any AlH_4 species, we performed ^{27}Al $\{^1$H$\}$ MAS NMR experiments and observed no significant narrowing of the Al_2O_3 resonances with decoupling, which we did observe in the $NaAlH_4$ peak for sample (S_2). ^{27}Al MQ MAS was also performed on this sample and shows distinct isotropic quadrupolar shifts that show fairly ordered sites for the different Al_2O_3 species, including 1) octahedral 0–10 ppm, 2) pentacoordinate around 30 ppm, and 3) tetrahedral 40–80 ppm [14]. This indicates a small distribution of quadrupolar coupling, consistent with nano-size or possibly amorphous Al_2O_3.

In X-ray diffraction, the coherence length of crystals is related to the peak width. This means that nano-sized crystals are represented by broad peaks in the background. Since the X-ray diffraction does not show any indication of crystalline Al_2O_3 and the pentacoordinate Al_2O_3 exists in the ^{27}Al MQMAS data, this indicates that Al_2O_3 are in the form of nano-clusters of Al_2O_3 and possess sharp peaks in the ^{27}Al MQ MAS data due to the Al_2O_3 quadrupolar interaction with electric field gradient on the surface of this material [13]. The presence of Al_2O_3 in sample (S_4) may suggest contamination during processing, or strong coordination between the Al and THF molecules.

Table 2.4: ^{27}Al NMR lines in [ppm] of the detected compounds in each sample.

Compound	S_2	S_{3a}	S_4	S_5
$NaAlH_4$	94.6±0.5	94.2±0.5		
Na_3AlH_6		-42.6±0.2		
Al metal		1640.0±0.9	1641.0±0.9	1640.0±0.9
$TiAl_3$				664±0.4
Al_2O_3 (6-fold)			8.4±0.1	
Al_2O_3 (5-fold)			35.5±0.2	
Al_2O_3 (4-fold)			63.6±0.3	

The ^{27}Al NMR spectra of sample (S_5) shown in Figure (2.4d) shows four resonances: two at approximately 10 ppm and 103 ppm, with respective line widths of 19 ppm and 30 ppm, a broad resonance at approximately 664 ppm, and a metallic aluminum resonance at 1640 ppm. The extremely broad line shape of the 664 ppm resonance suggests the presence of some amorphous or nanoclustered $TiAl_3$. Figure (2.5) directly compares the ^{27}Al MAS NMR spectra of pure $TiAl_3$ in the $L1_2$ metastable structure (preparation of this phase is described elsewhere [4]) and (S_5). These line shapes are extremely similar and indicate that there may be $TiAl_3$ in

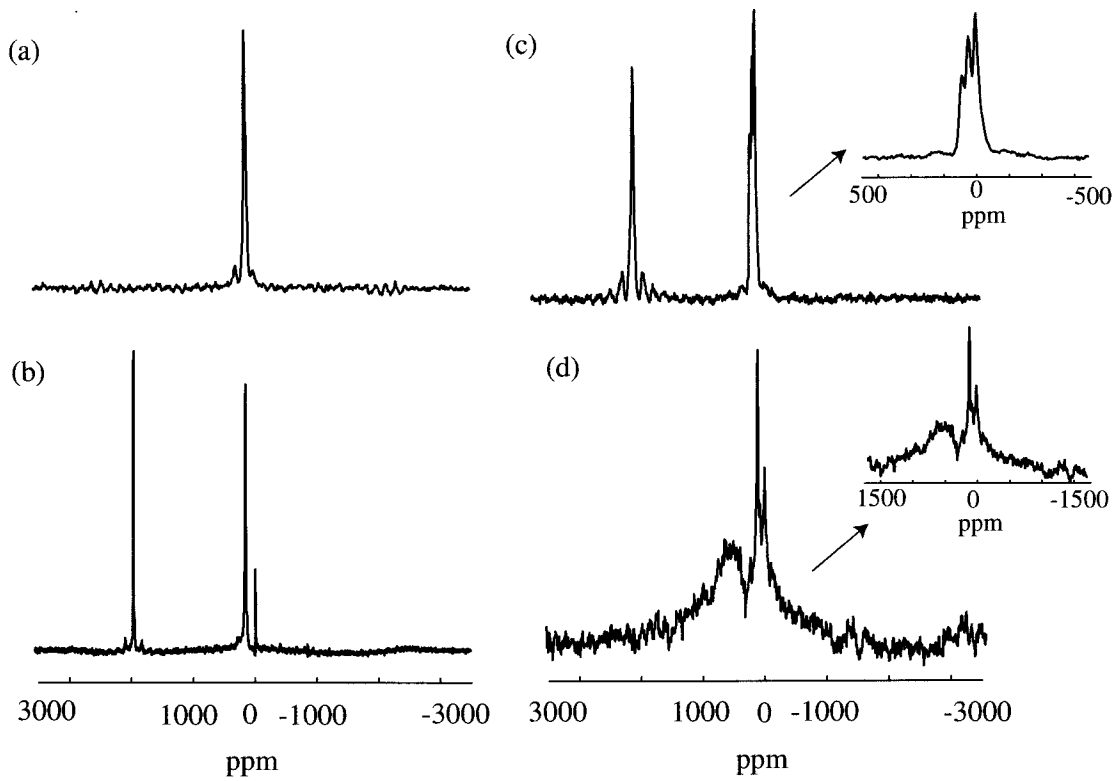

Figure 2.4: ^{27}Al MAS NMR spectra of samples (a) S_2, (b) S_{3a}, (c) S_4, and (d) S_5.

sample (S_5). The differences in line shape might be a result of small differences in the local environments of Al in the $TiAl_3$. This observation also agrees with results from the x-ray diffraction studies above, which show that in (S_5) samples the formation of $TiAl_3$ is likely.

Table 2.5: ^{23}Na NMR lines in [ppm] of the detected compounds in each sample.

Compound	S_2	S_{3a}	S_4	S_5
NaCl		7.2±0.3	7.0±0.3	6.8±0.3
$NaAlH_4$	-9.4±0.3	-9.4±0.3		
Na_3AlH_6		22.9±0.4		

^{23}Na MAS NMR spectra are shown in Figure (2.6), with peak positions given in Table (2.5). Figure (2.6a) shows a spectrum with a peak at -9.4 ppm from sample (S_2), and indicates only the presence of $NaAlH_4$ in this sample. The spectra of sample (S_{3a}) is shown Figure (2.6b), in which three resonances were observed: one at -9.4 ppm due to $NaAlH_4$, one at 22.9 ppm, indicating the presence of Na_3AlH_6, and one at 7.2 ppm, which indicates the presence of NaCl. Spectra from samples (S_4) and (S_5) are not shown, and indicate the presence of only NaCl, as expected. Proton NMR (not shown) also indicates that hydrogen is present in sample (S_4), but this may be due to residual THF, further supporting the possibility of nano-particle formation as discussed above.

2.5 Conclusions

X-ray diffraction of $NaAlH_4$ crystals grown from saturated THF solutions containing $TiCl_3$, and annealing studies of $TiCl_3$-doped NaH, indicate no solubility for Ti in the $NaAlH_4$ or NaH lattices, respectively. Lattice parameter changes observed in NaH in TiF_3 doped samples are shown to be fluorine substitution into the NaH lattice. The reaction products in doped $NaAlH_4$ depend on the method of preparation. Mechanical milling and solution mixing are shown to result in different Ti-compounds. The formation of $TiAl_3$ promoted by mechanical milling, does not appear to form in solution mixed samples, as indicated by x-ray diffraction, and ^{27}Al MAS NMR. The ^{27}Al MAS NMR of THF-solution mixed samples indicates aluminum in bulk and possibly Al_2O_3, which may be consistent with Ti-Al nano-clusters where oxygen in the THF molecule is coordinated with aluminum in a Ti-Al compound or nanocluster. It is also possible that these samples (S_4) are simply very reactive Ti nano-clusters that oxidize during drying, which then forms Al_2O_3. This is in contrast to the solvent-free samples, where NMR indicates that some aluminum is present in the form of $TiAl_3$, also consistent with XRD measurements.

This work suggests that variations in initial hydrogen sorption kinetics are likely due to the very different compound formation resulting from the doping conditions.

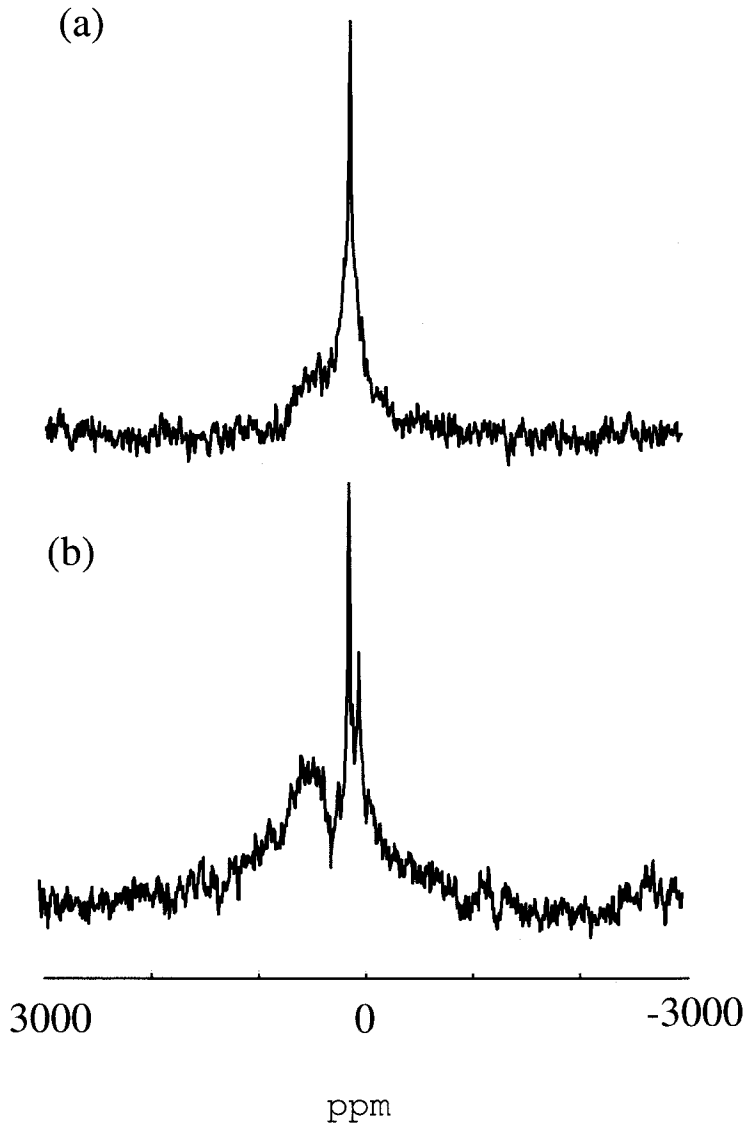

Figure 2.5: ^{27}Al MAS NMR spectra of (a) $TiAl_3$ in the $L1_2$ structure, and (b) sample S_5.

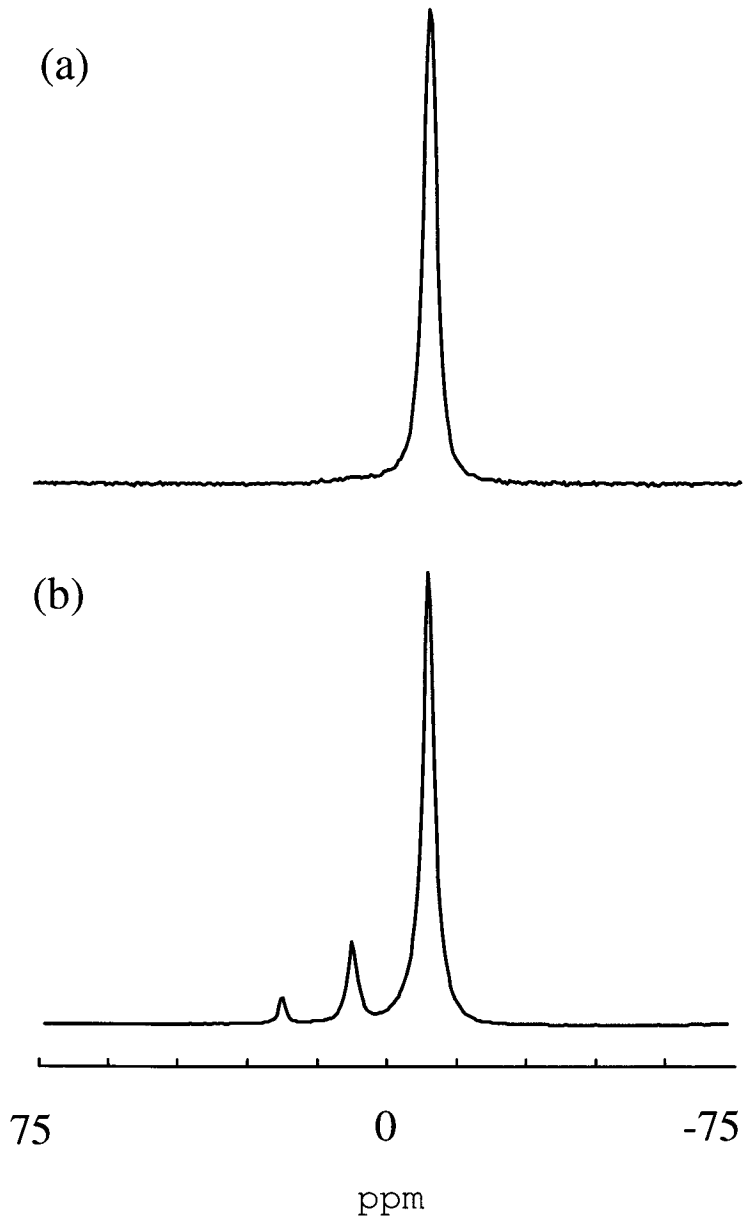

Figure 2.6: ^{23}Na MAS NMR spectra of samples (a) S_2, and (b) S_{3a}.

The fact that sorption rates after many cycles tend to similar values for very many different dopant precursors and doping methods indicates that the initial compounds are likely transient, and may not be important in the ultimate sorption rates in Ti-doped sodium alanates.

ACKNOWLEDGMENTS

This work was funded by the U.S. Department of Energy, Office of Energy Efficiency and Renewable Energy, in the Hydrogen, Fuel Cells & Infrastructure Technologies Program under contract No. DE-AC36-83CH10093, and Sandia National Laboratories through the Laboratory Directed Research and Development program. NMR work was performed under the auspices of the U.S. Department of Energy by University of California, Lawrence Livermore National Laboratory under Contract W-7405-Eng-48. The authors thank V. Ozolins for useful discussions and Ken Stewart for construction of the hydrogen sorption apparatus.

Bibliography

[1] B. Bogdanovic and M. Schwickardi. Ti-doped alkali metal aluminium hydrides as potential novel reversible hydrogen storage materials. *Journal of Alloys and Compounds*, 253-254(1-2):1 – 9, May 1997.

[2] B. Bogdanovic, R.A. Brand, A. Marjanovic, M. Schwickardi, and J. Tolle. Metal-doped sodium aluminium hydrides as potential new hydrogen storage materials. *J. Al. Comp.*, 302(1-2):36 – 58, April 2000.

[3] G. Sandrock, K. Gross, and G. Thomas. *Journal of Alloys and Compounds*, 339:299 – 308, June 2002.

[4] E.H. Majzoub and K.J. Gross. Titanium-halide catalyst-precursors in sodium aluminum hydrides. *Journal of Alloys and Compounds*, 356-357:363 – 7, August 2003.

[5] B. Bogdanovic, M. Felderhoff, M. Germann, M. Hartel, A. Pommerin, F. Schuth, C. Weidenthaler, and B. Zibrowius. *Journal of Alloys and Compounds*, 350:246 – 55, February 2003.

[6] Dalin Sun, T. Kiyobayashi, H.T. Takeshita, N. Kuriyama, and C.M. Jensen. X-ray diffraction studies of titanium and zirconium doped $NaAlH_4$: elucidation of doping induced structural changes and their relationship to enhanced hydrogen storage properties. *Journal of Alloys and Compounds*, 337:L8 – 11, May 2002.

[7] C. Weidenthaler, A. Pommerin, M. Felderhoff, B. Bogdanovic, and F. Schuth. On the state of the titanium and zirconium in ti- or zr-doped naalh4 hydrogen storage material. *PHYSICAL CHEMISTRY CHEMICAL PHYSICS*, 5(22):5149 – 5153, 2003.

[8] K. J. Gross, E. H. Majzoub, and S. W. Spangler. The effects of titanium precursors on hydriding properties of alanates. *Journal of Alloys and Compounds*, 356/357:423 – 8, AUG 2003.

[9] M. Fichtner, O. Fuhr, O. Kircher, and J. Rothe. Small ti clusters for catalysis of hydrogen exchange in naalh4. *NANOTECHNOLOGY*, 14(7):778 – 785, JUL 2003.

[10] B. Bogdanovic, M. Felderhoff, S. Kaskel, A. Pommerin, K. Schlichte, and F. Schuth. Improved hydrogen storage properties of ti-doped sodium alanate using titanium nanoparticles as doping agents. *ADVANCED MATERIALS*, 15(12):1012, JUN 2003.

[11] Ritter H., Ihringer J., Maichle J.K., and Prandl W. *Simultaneous Structure Refinement with Multiple Powder Diffraction Data Sets.* Institute für Kristallographie der Universität Tübingen, Charlottenstr. 33, D-72070 Tübingen, 1998. Version 2.6.

[12] V. Ozolins. Private communication.

[13] C.J. Brinker and G.W. Scherer. *Sol-Gel Science.* Academic Press, 1989.

[14] P. Florian, M. Gervais, A. Douy, D. Massiot, and J. P. Coutures. A multinuclear multiple-field nuclear magnetic resonance study of the ysub 2osub 3-alsub 2osub 3 phase diagram. *Journal of Physical Chemistry B*, 105(2):379 – 91, JAN 2001.

Chapter 3

Lattice dynamics of $NaAlH_4$ from high-temperature single-crystal Raman scattering and *ab initio* calculations: Evidence of highly stable AlH_4^- anions

E.H. Majzoub[1], K.F. McCarty
Sandia National Laboratories
P.O. Box 969, Livermore, California 94551

V. Ozoliņš[2]
Department of Materials Science and Engineering
University of California, Los Angeles, California 90095-1595

Abstract

Polarized Raman scattering on single crystals of $NaAlH_4$ has been used to determine the symmetry properties and frequencies of the Raman-active vibrational modes over the temperature range from 300 to 425 K, i.e., up to the melting point T_{melt}. Significant softening (by up to 6 %) is observed in the modes involving rigid translations of Na^+ cations and translations and librations of AlH_4^-. Surprisingly, the data indicate mode softening of less than 1.5 % for the Al-H stretching and Al-H bending modes of the AlH_4^- anion. These results show that the AlH_4^- anion remains a stable structural entity even near the melting point. First-principles linear re-

[1]Corresponding author. Tel.: +1-925-294-2498; fax:+1-925-294-3410. *E-mail address:* ehmajzo@sandia.gov

[2]Tel.:+1-310-267-5538; fax:+1-310-206-7353. *E-mail address:*vidvuds@seas.ucla.edu

sponse calculations of phonon mode frequencies are in reasonably good agreement with the Raman results. The phonon mode Grüneisen parameters, calculated using the quasiharmonic approximation, are found to be significantly higher for the translational and librational modes than for the Al-H bending and stretching modes, but cannot account quantitatively for the dramatic softening observed near T_{melt} in the former two types of modes, suggesting an essentially anharmonic mechanism. Effect of zero-point vibrations on the calculated lattice parameters is found to be large (expansion by 1.2 and 1.5% in the a and c parameters, respectively), as expected for a compound with many light elements. We discuss the implications of the observed mode softening for the kinetics of hydrogen release and hypothesize that breaking up the AlH_4^- anions is the rate limiting step. The enhanced kinetics of absorption and desorption in Ti-doped $NaAlH_4$ powders is attributed to the effectiveness of Ti in promoting the break-up of the AlH_4^- anions.

3.1 Introduction

Dynamics of hydrogen in solids is a long-standing problems in materials science which provides fascinating opportunities to study the behavior at the boundary between the classical and quantum physics. Hydrogen, being the lightest and the most abundant of all elements, exhibits interesting properties that can be both useful (e.g., efficient solid-state storage) and detrimental (e.g., hydrogen embrittlement) in practical applications. From a theoretical perspective, describing the behavior of hydrogen from the first principles has always been a challenge because the simple classical point-particle treatment is often a poor approximation due to the de-localized nature of the protonic wave function. Experimental studies of hydrogen dynamics are invaluable for calibrating the accuracy of the various *ab initio* computational methods that aim to incorporate the non-classical nature of hydrogen in modern electronic structure studies.

This paper deals with the lattice dynamics of sodium aluminum tetrahydride, $NaAlH_4$, often referred to as sodium alanate. $NaAlH_4$ crystallizes in an ionic structure containing Na^+ cations and AlH_4^- anions, arranged in an ordered manner on the vertices of a tetragonally deformed face-centered cubic lattice. Bonding within the AlH_4^{-1} groups is best characterized as polar covalent (a detailed discussion of the electronic structure and crystal bonding can be found in Refs. [1, 2]). Sodium alanate is a representative of a family of complex hydrides of the $A_n(MH_4)^n$ type, where A is a metal of valence n, and M is a trivalent element, such as B, Al, or Ga.[?] These hydrides have been known for decades, but have attracted relatively little attention until Bogdanovič's *et al.*[3] seminal discovery that, in the presence of transitional metal catalysts, the material can reversibly release and absorb hydrogen at ambient temperatures and pressures. Metal-doped complex hydrides represent a new paradigm for solid-state hydrogen storage, promising a dramatic increase in the reversibly stored hydrogen weight fraction over traditional metal hydrides.

The decomposition reaction proceeds in two steps, first into the sodium aluminum hexahydride, Na_3AlH_6, which further decomposes into NaH:

$$NaAlH_4 \rightleftharpoons \frac{1}{3}Na_3AlH_6 + \frac{2}{3}Al + H_2 \tag{3.1}$$

$$Na_3AlH_6 \rightleftharpoons 3\,NaH + Al + \frac{3}{2}H_2. \tag{3.2}$$

These reactions result in about 5.5 wt. % of available hydrogen, surpassing all other known *inexpensive* materials. The system has reasonable kinetics only upon doping with a few mol. % of transition metals, with Ti the preferred choice.[4] The Ti-halide doped samples begin to decompose at pragmatic rates at temperatures of about 80-90 °C, [5] well below the melting point of the compound at about 180 °C.[6, 7]

The mechanism of enhanced kinetics in Ti-doped samples is not yet understood, remaining one of the most important obstacles towards developing other material/catalyst combinations with improved kinetics and higher hydrogen weight fraction. Numerous authors [8, 9, 10, 11, 12, 13, 14, 5, 15, 1] have performed kinetic and structural measurements on Ti-doped powdered samples, often reaching contradictory conclusions about the role of Ti. Here, we adopt a different approach and ask instead what happens in a sample that is *not* doped with Ti as one approaches and exceeds the thermodynamic transition temperature for the decomposition reactions (3.1)? Surprisingly, the dynamical properties of single-crystal $NaAlH_4$ have not yet been investigated. Adopting this approach, we can characterize the dynamical properties and structural stability of the AlH_4^- anion that is intrinsic to the bulk material, and glean valuable insights into what could be the rate-limiting physical processes associated with reactions (3.1) and (3.2). The stability of the AlH_4^- anion is of particular interest, as it can help to clarify the role of the transition metal dopant, and can be probed directly using Raman spectroscopy.[?]

We have grown single crystals of sodium alanate and performed *in situ* Raman scattering measurements up to, and slightly beyond, the melting temperature of this compound. Use of high-quality single crystals allows us to accurately identify the symmetries of the phonon modes and investigate the temperature-dependence of their frequencies. The Raman results are compared with the predictions of state-of-the-art *ab initio* density functional theory (DFT) linear response calculations of harmonic phonon frequencies and quasi-harmonic Grüneisen parameters. We find that the phonon modes separate neatly into four groups, best described as translational, librational, Al-H bending and Al-H stretching modes, in agreement with previous Raman studies on *powdered* $NaAlH_4$.[16] Of these modes, the former two exhibit dramatic softening in the narrow interval from room temperature to the melting point, indicating the presence of very large anharmonic effects beyond the "normal" softening associated with lattice expansion. In contrast, the high-frequency modes, corresponding to deformations of the AlH_4^{-1} tetrahedra, show a weak temperature-dependence, indicating that the thermal excitation energies available at ambient temperatures are too low to compete with the strong chemical

bonding within these molecular units. Since the decomposition of $NaAlH_4$ requires breaking up of the AlH_4^{-1} units and re-bonding some of them into an octahedral coordination to form Na_3AlH_6, and both of these processes have to happen well below the melting temperature, our results suggest that this break-up is the rate-limiting step in reaction (3.1).

3.2 Methods

3.2.1 Experiments

Single crystal samples of $NaAlH_4$ were grown by solvent evaporation from *Sigma Aldrich* 1 M solutions of $NaAlH_4$ in THF. The crystals were grown in capped vials, of diameter 20 mm, and a height of 50 mm. Typically 10 ml of 1 M solution was used for evaporation.

Multiple nuclei were often observed, and assumed to be due to impurities in the as-received solution, and resulted in the formation of many crystals of dimension 0.1–0.5 mm. The following procedure was employed to produce larger crystals. A vial prepared with solution as above was allowed to evaporate to the saturation point of $NaAlH_4$ in THF, about 3 mols/l.[4] Many crystallites formed in this solution and removed many of the nucleation sites. This supersaturated solution was then gently removed to a clean vial and a previously prepared and selected 0.5–1 mm crystal was placed in the supersaturated solution and used as a seed. Although additional nucleation occurred in the seeded solution, the resulting seed crystal typically grew to around 2 mm in dimension.

Raman data were collected on a Spex model 1877 0.6 m triple spectrometer, using the 514 nm line of a Coherent Innova Ar ion laser, at a power of about 10 mW at the sample. The spectrometer efficiency ratio for horizontal and vertical polarizations was corrected for in the polarized spectra. Spectrometer and filter gratings were 1800 and 600 lines/mm, respectively.

All spectra were collected in 180° backscattering geometry utilizing a microprobe apparatus consisting of a 20× objective to focus the incident light and collect the scattered light. Polarization data are described using Porto notation, such as $z(xy)\bar{z}$, indicating that the incident and scattered light travel along the z and $\bar{z}$ direction, and the incident and scattered polarizations are x and y, respectively. These directions correspond to the laboratory frame with the crystal orientation described below.

The high-temperature *in-situ* cell consisted of a cylindrical platinum sample pan of approximately 7 mm in diameter and 5 mm in depth, with one end open to allow for entry and exit of the laser beam. The platinum pan was enclosed in an alumina cup surrounded by a heating coil. A water-cooled stainless steel housing enclosed the sample holder and had a fused silica window on one end. A constant flow of approximately 3–5 cc/sec of ultra-high purity Ar was maintained through the cell during the *in-situ* measurement. A type-K thermocouple bead was held in

contact with the bottom of the pan, upon which rested the crystal. The temperature measurements were approximate because of non-ideal thermal contact between the sample and the thermocouple or sample pan.

3.2.2 *Ab initio* calculations

Ab initio calculations of phonon spectra were performed using the density functional theory (DFT) linear response method.[17] We used norm conserving pseudopotentials generated according to the Troullier-Martins prescription,[18] including the Louie-Froyen-Cohen[19] nonlinear core correction for Na and Al. Wave functions were expanded in a plane wave basis set with an energy cutoff $E_{\text{cut}} = 680$ eV. A regular $8\times8\times8$ k-point mesh was used for sampling the electronic states in the Brillouin zone of the body-centered tetragonal unit cell of $NaAlH_4$. The structural properties and formation energies calculated with both the local-density approximation (LDA) and the generalized gradient approximation (GGA) have been given in an earlier publication.[1] Born effective charges, $Z^*_{\alpha\beta}(i)$, describing the macroscopic polarization induced by ionic displacements in optical phonons, and the high-frequency dielectric tensor, $\epsilon^{\infty}_{\alpha\beta}$, were calculated using the linear response formalism.[17] Due to the large band gap of $NaAlH_4$ (about 5 eV), the $8 \times 8 \times 8$ k-point mesh was more than sufficient to obtain very accurate dielectric properties. Decreasing the sampling mesh to $6 \times 6 \times 6$ produced negligible (approx. 1%) variations in the calculated $\epsilon^{\infty}_{\alpha\beta}$.

Phonon mode Grüneisen parameters, $\gamma = \frac{\partial \ln \omega}{\partial \ln a}$, where ω is the phonon frequency, were estimated using the quasiharmonic approximation. We considered changes in both the overall volume at $c/a = \text{const}$ and in the c/a ratio at $V = \text{const}$, where c and a are the lattice parameters for this body-centered tetragonal crystal. For each, we took an increase of approximately 2% and subsequently performed a relaxation of hydrogen positions (metal ion positions are fixed by symmetry). Phonon frequencies were calculated on a $4 \times 4 \times 4$ phonon wave vector grid. Using standard expressions for the vibrational free energy, we expressed the latter as a linear function of lattice parameters a and c, and a non-linear interpolating function of the temperature. We also parameterized the total static lattice energy as a function of both a and c. For each temperature, the minimum of the total free energy (static lattice + vibrational) yielded the lattice parameters as functions of T. In principle, a fully consistent quasi-harmonic treatment also requires the evaluation of the Grüneisen parameters corresponding to changes in hydrogen coordinates. However, such a tedious undertaking is expected to matter only for the high-frequency Al-H bond-stretching and H-Al-H bond-bending modes. Since the thermal population of these modes is low even at the melting temperature of the compound, the effects on the lattice parameters and quasiharmonic mode softening are expected to be small.

For $NaAlH_4$, it has been shown that the generalized gradient approximation (GGA) gives noticeably better structural properties and formations energies than the LDA.[1] It is also reasonable to expect that the GGA will give better phonon

frequencies if the calculations are performed at the predicted GGA lattice parameters. Unfortunately, since the GGA is not implemented in our linear response code, we had to resort to frozen phonon calculations using the Vienna Ab-Initio Simulation Package (VASP) developed at at the Institut für Material-physik of the Universität Wien.[20, 21, 22, 23, 24] We obtained all the **q**=0 phonon states using the unit cell of $NaAlH_4$ and calculating all 7 (2 each for Na and Al, and 3 for H) symmetry inequivalent rows of the **q**=0 dynamical matrix. Individual elements, $D^{ij}_{\alpha\beta}$, of the **q**=0 dynamical matrix are proportional to the force acting on the atom i along the Cartesian direction α if the atom j is displaced by a small amount along the direction β, $F^i_\alpha = -\sqrt{M_i M_j} D^{ij}_{\alpha\beta} u^i_\beta$. For each symmetry-inequivalent choice of u^i_β, the forces F^i_α were obtained for a set of 11 evenly distributed displacements around the equilibrium position, from $u^i_\beta = -0.1$ to $+0.1$ with a step of 0.02 Å. The calculated Hellman-Feynman forces were fit using third-order splines, and the linear terms were used to extract $D^{ij}_{\alpha\beta}$. We encountered annoying numerical issues when extracting accurate values of $D^{ij}_{\alpha\beta}$ associated with the movement of Na atoms, caused by small, seemingly random fluctuations in the Hellmann-Feynman forces at the level of 0.02 eV/Å. The origin of these numerical errors is not clear. We estimate that the frequencies of the lowest (translational) phonon modes, listed in Table 3.1, have a numerical uncertainty of approximately $10\,\mathrm{cm}^{-1}$. This uncertainty is small enough so that a meaningful comparison with experimental Raman data is possible. However, we were not able to extract the Grüneisen parameters from GGA frozen phonon calculations for the translational modes as the noise was on the same level as the quasiharmonic softening. In contrast, our linear response LDA results are numerically accurate to a few cm^{-1}, i.e., increasing the plane wave cutoff energy, the number of k-points or the degree of convergence would result in very small changes in the calculated frequencies.

The important question of physical accuracy is much more complex, as there are several effects which are either approximated or not included in these kinds of calculations. Among the latter, use of approximate exchange-correlation functionals (LDA or GGA) and quasi-harmonic treatment of anharmonic vibrational effects are the most serious. Note that the calculations are performed at the predicted equilibrium geometry (obtained from LDA or GGA) for a static *nonvibrating* lattice. Effect of atomic vibrations on the lattice parameters is taken into account via phonon mode Grüneisen parameters, which allow us to evaluate both the $T = 0$ K lattice expansion due to zero-point vibrations and the $T > 0$ coefficient of thermal expansion. Our treatment includes the changes in effective interatomic force constants due to lattice expansion, but neglects intrinsically anharmonic effects, such those associated with phonon-phonon interactions and finite phonon lifetimes. The quasi-harmonic approximation is expected to become increasingly worse upon approaching the melting temperature, which for $NaAlH_4$ is around $T = 180°C$. Since the crystal melts by disintegrating into Na^+ cations and AlH_4^- anions, it is expected that near the melting temperature the translational displacements and rotations of

the AlH_4^- units become very large, and thus the importance of intrinsic anharmonic effects (i.e., of those beyond the simple quasiharmonic lattice expansion) for the low-energy modes should also increase. The magnitude of these effects could be quantified using *ab initio* molecular dynamics (MD) simulations, which we unfortunately found to be impractically time-consuming, and possibly lacking in physical accuracy due to the neglect of the quantum-mechanical nature of hydrogen ions in MD. Further studies based upon a fully quantum-mechanical treatment of the H ions, such as the path integral approach,[?] would help to clarify whether the existing discrepancies between the calculated and measured lattice parameters and phonon frequencies can be attributed to the approximate exchange-correlation, to the approximate treatment of the hydrogen dynamics, or both.

3.3 Results

3.3.1 Mode Assignments from Polarized Raman Spectra

The crystal structure of $NaAlH_4$ is body centered tetragonal with the space group $I4_{1/a}$.[25, 26] The prepared $NaAlH_4$ single crystals were square pyramidal in morphology, with the largest facets being (101) planes. This crystal habit is related to that of scheelite, with prototype structure $CaWO_4$. The scattering geometry had the incident and scattered light along the normal to the (101) facet. The vibrational mode structure of this crystal can be determined from the correlation method,[27] with the following result:

$$\Gamma_{\text{vib}}^{\text{tot}} = 3\,\text{A}_g + 5\,\text{B}_g + 5\,\text{E}_g + 3\,\text{A}_u + 3\,\text{B}_u + 3\,\text{E}_u. \tag{3.3}$$

$NaAlH_4$ is centrosymmetric, therefore all even ("gerade") modes are Raman active, and all odd modes are infrared active, according to the rule of mutual exclusion. The Raman polarizability tensors for the crystal class 4/m C_{4h}, for the irreducible representations A_g, B_g, and E_g, respectively, are

$$A_g : \begin{pmatrix} a & 0 & 0 \\ 0 & a & 0 \\ 0 & 0 & b \end{pmatrix} \quad B_g : \begin{pmatrix} c & d & 0 \\ d & -c & 0 \\ 0 & 0 & 0 \end{pmatrix} \quad E_g : \begin{pmatrix} 0 & 0 & e \\ 0 & 0 & f \\ e & f & 0 \end{pmatrix}. \tag{3.4}$$

The tensors, after transformation to a coordinate system with the [101] direction pointing along the laboratory z-axis (a rotation of the crystal about the laboratory

y-axis by $\phi = 1.1537\,\mathrm{rad}$), become

$$A_g \;:\; \begin{pmatrix} 0.8\,b + 0.2\,a & 0 & 0.4\,a - 0.4\,b \\ 0 & a & 0 \\ 0.4\,a - 0.4\,b & 0 & 0.2\,b + 0.8\,a \end{pmatrix}, \tag{3.5}$$

$$B_g \;:\; \begin{pmatrix} 0.16\,c & 0.41\,d & 0.37\,c \\ 0.41\,d & -c & 0.91\,d \\ 0.37\,c & 0.91\,d & 0.84\,c \end{pmatrix}, \tag{3.6}$$

$$E_g \;:\; \begin{pmatrix} -0.74\,e & -0.91\,f & -0.67\,e \\ -0.91\,f & 0 & 0.41\,f \\ -0.67\,e & 0.41\,f & 0.74\,e \end{pmatrix}. \tag{3.7}$$

While no polarization configuration in this scattering geometry allows a single symmetry to be exclusively allowed, we will show that careful experimental analysis combined with first-principles calculations of phonon frequencies allow us to experimentally identify most of the Raman-active phonons. It can be seen from the transformed polarization tensors in Eqs. (3.5)–(3.7) that A_g modes will have no mixed components (xy or yx). A_g modes represent motion of hydrogen atoms only. Both E_g and B_g modes result in hydrogen atom motion, but differ in the motion of the metal atoms. E_g modes will have no yy component, and correspond to Na and Al motion perpendicular to the c-axis of the crystal. B_g modes can have all components of polarization for this crystal face, and correspond to Na and Al motions parallel to the c-axis.

The class of 4d/5d oxides iso-structural to $CaWO_4$ has been investigated by Porto *et al.* [?], and references therein. The phonon modes of these oxides are well described by "external" modes, where the XO_4^{--} ions are considered rigid structural units, and "internal" modes, in which the the ions undergo molecular-like vibraions about a stationary center of mass. We show that the $NaAlH_4$ crystal can be described in the same manner.

The measured Raman spectra at room temperature are given in Figs. 3.1 and 3.2. The extracted values for the mode frequencies at room temperature are given in Table 3.1. While the vibrational modes corresponding to Al-H stretching, bending, libration of the AlH_4^{-1} anion, and translational modes were determined previously on powdered samples,[16] a polarization analysis of single crystal samples is required for unambiguous mode symmetry identification and to distinguish overlapping vibrational modes. The data peaks were fit to pseudo-Voigt profiles. The fitting errors shown do not represent the instrumental resolution of the spectrometer, which is approximately $1\,\mathrm{cm}^{-1}$. Some of the peak positions are strongly temperature dependent, as shown in the next section.

Translation modes: The four modes of lowest frequency correspond to translational modes. The mode at approximately $117\,\mathrm{cm}^{-1}$ consists of strong contributions from xx, xy, and yx, and essentially no intensity in yy, and was therefore assigned to E_g. Because the next mode, located at about $125\,\mathrm{cm}^{-1}$, has a very diminished

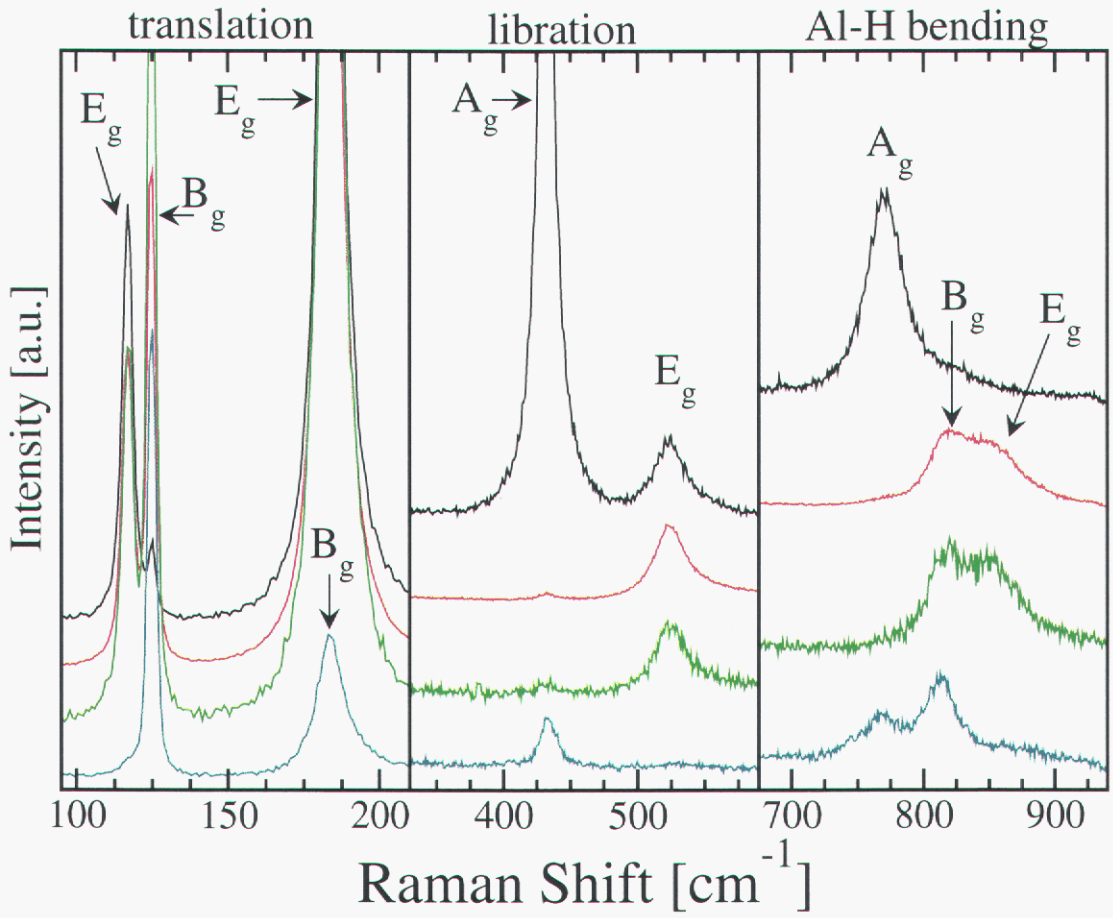

Figure 3.1: Raman spectra from the (101) face of single crystal $NaAlH_4$, showing the bending, and libration modes of the AlH_4^{-1} anion, and the translational modes at the lowest values of the wavenumber. For clarity, the intensity scales are different in the three panels and the spectra are offset. In each panel, the polarizations are xx, xy, yx, and yy, from top to bottom.

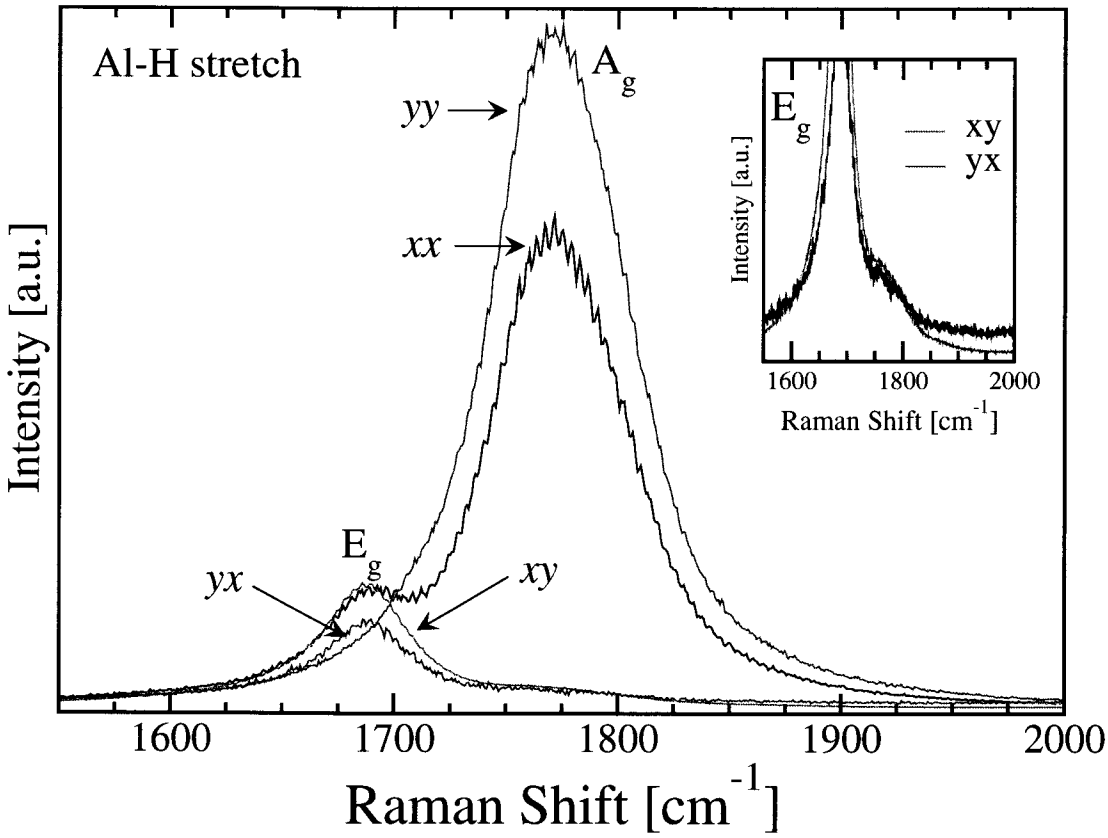

Figure 3.2: Raman spectra from the (101) face of single crystal $NaAlH_4$, showing the Al-H stretching modes. The inset arrow shows the shoulder on the E_g modes in the xy and yx polarizations where the B_g mode may be located.

Table 3.1: Measured Raman mode frequencies from the (101) face in single crystal $NaAlH_4$ in cm^{-1}. Horizontal lines in the table separate, from lowest to highest wavenumber, modes attributed to translation, libration, Al-H bending, and Al-H stretching modes, respectively. All data were taken at temperature of approximately 22.5°C. The fitted peak position errors are shown only when they are greater than or equal to $1\,cm^{-1}$. The last column lists the phonon mode Grüneisen parameters for a uniform change in volume, $\gamma = 3\frac{\partial \ln \omega}{\partial \ln V}$, calculated using the LDA linear response method.

Mode	Polarization				*Ab initio* calculations		
symmetry	xx	xy	yx	yy	LDA	GGA	γ_G
			Translational modes				
E_g	117	117	117	—	135	116	1.4
B_g	125	125	125	125	128	101	0.7
E_g	184	184	184	—	210	191	1.0
$B_g{}^1$	—	—	—	184	220	182	1.7
			Librational modes				
A_g	432.5	—	—	432.5	512	458	0.9
E_g	524	524	525±1	—	614	560	0.8
			Al-H bending modes				
A_g	771	—	—	765±1	759	748	0.5
B_g	—	817±1	815±2	813±1	786	797	0.3
$E_g{}^1$	—	848±3	851±4	—	822	817	0.7
$B_g{}^2$	—	—	—	—	844	850	0.5
			Al-H stretching modes				
E_g	1684	1687	1687	—	1681	1649	0.3
A_g	1774	—	—	1773	1729	1726	0.2
$B_g{}^1$	—	1782	1782±3	—	1706	1673	0.3

xx component relative to the other polarizations, it is assigned to B_g. The peak at $184\,cm^{-1}$ has strong intensity in the xx, xy, and yx polarizations, consistent with an E_g mode. However, the peak at $184\,cm^{-1}$ also contains some intensity in yy polarization, which cannot come from an E_g mode. Analysis shows that the yy intensity is greater than expected from "leakage" of the E_g mode due to misalignment of the crystal. The intensity in the yy polarization of the E_g mode at $117\,cm^{-1}$ is about 24 times weaker than the xx polarization intensity. In contrast, the yy intensity of the $184\,cm^{-1}$ peak is about 9 times weaker than the xx intensity. The large difference in the xx and yy intensity ratios for the two peaks suggest that the $184\,cm^{-1}$ peak contains a B_g mode in addition to the clear E_g mode. We note that this assignment is tentative.

Libration modes: The mode at about $432\,cm^{-1}$ is assigned to A_g. Any intensity in the mixed polarizations is attributed to leakage due to slightly misaligned crystal or polarizer settings. Because there is no intensity in the yy polarization, the mode at about $524\,cm^{-1}$ is clearly E_g.

Al-H bending modes: The peak at about $767\,cm^{-1}$ has strong xx and yy intensity and no intensity in crossed polarization (xy and yx). Therefore it is an A_g mode. The crossed polarization spectra show a broad band around $825\,cm^{-1}$ with at least two peaks. This band must arise from B_g or E_g modes. The peak at about $815\,cm^{-1}$ shows intensity in yy polarization and some intensity in xx polarization, establishing it as a B_g mode. Assigning the intensity near $849\,cm^{-1}$ is problematic – it arises from either a B_g mode with small matrix element c, or an E_g mode with small matrix element e, as shown in Eqs. (3.6) and (3.7). Furthermore, the calculations show that there is a B_g mode and and E_g mode in this vicinity. Because the other B_g modes have strong yy intensity, we tentatively assign the $849\,cm^{-1}$ peak, with its weak yy intensity, to E_g. We note that the peak may contain intensity from the B_g mode.

Al-H stretching modes: The yy component shown in Fig. 3.2 can be fit well by a pseudo-Voigt line shape. The strong yy and xx components at about $1773\,cm^{-1}$ are therefore assigned to A_g. The lack of yy component at about $1683\text{-}1687\,cm^{-1}$ clearly indicates that this mode is E_g. A fit to the peak positions of the remaining intensity under the strong A_g mode, shown in the inset, yields a slightly different Raman shift of about $1781\text{-}1782\,cm^{-1}$, and is assigned to B_g. The B_g assignment here may be incorrect and the intensity in the mixed polarizations the result of mode leakage from slight misorientation of the crystal or polarizers.

3.3.2 High-Temperature Raman Spectra – Structural Stability

Non-polarized spectra were collected for *in-situ* measurements as a function of temperature. The crystal of $NaAlH_4$ used in the *in-situ* measurement was observed to begin decomposing, with surface melting and bubbling, presumably from hydrogen outgassing, when the thermocouple measured about 161 °C, which we refer to as

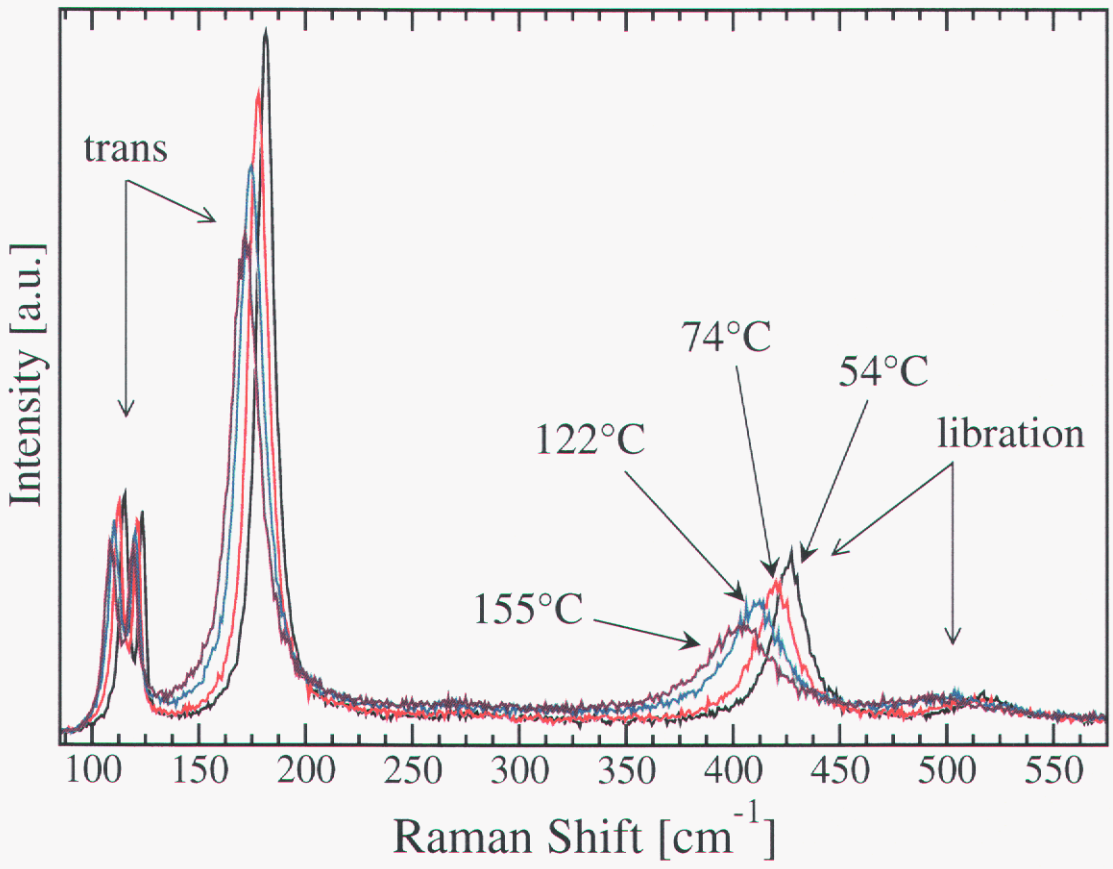

Figure 3.3: Unpolarized Raman spectra from single crystal $NaAlH_4$ at varying temperature, showing softening of the librational and translational modes, indicated by a shift to lower wavenumber.

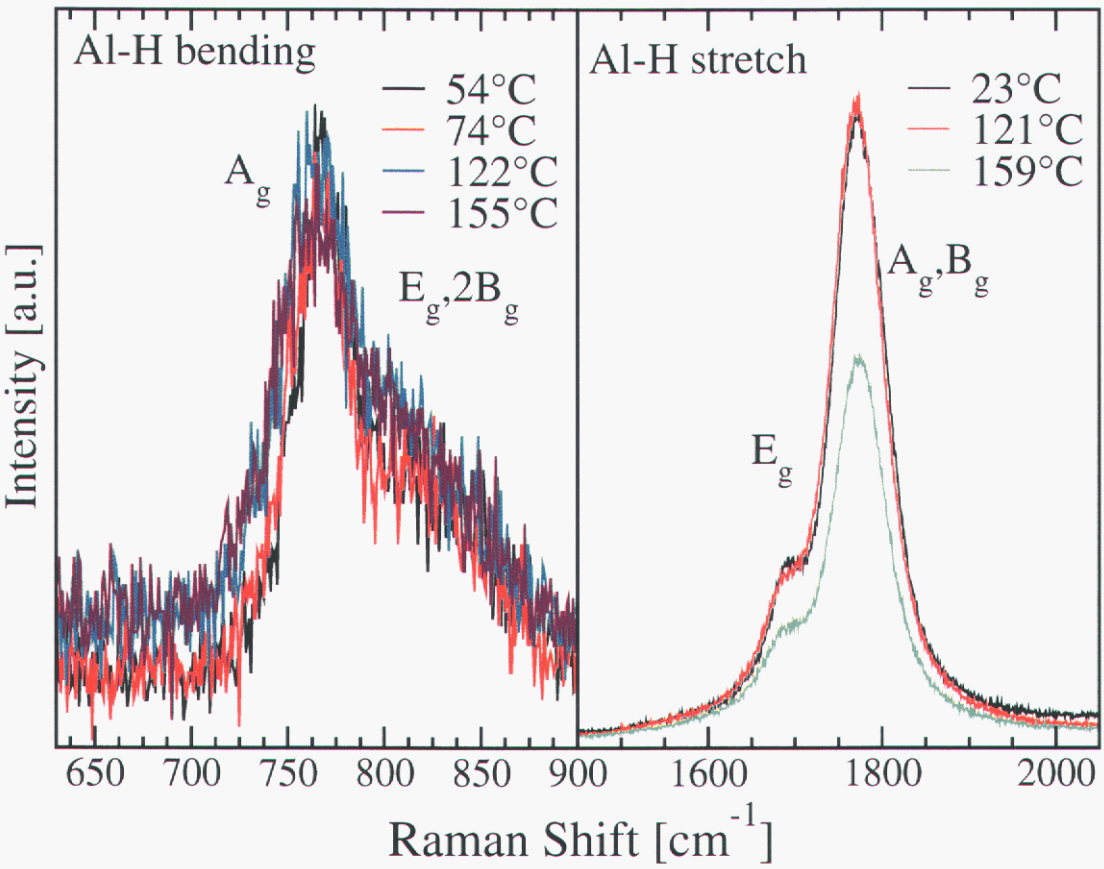

Figure 3.4: Unpolarized Raman spectra from single crystal $NaAlH_4$ at varying temperature, showing only slight softening of the bending and stretching modes of the AlH_4^{-1} anion.

the "apparent" melting temperature. The melting temperature of $NaAlH_4$ by our own differential scanning calorimetry measurements is 180.5±0.5 °C. We believe the difference is due to the flow of argon in our Raman test cell. Results of the *in-situ* measurements are shown in Figures 3.3 and 3.4. Mode softening is evidenced by a shifting of the vibration frequency to lower values of the wavenumber. This indicates that the force constants between atoms involved in these modes are becoming weaker, as a result of lattice expansion and anharmonic effects.

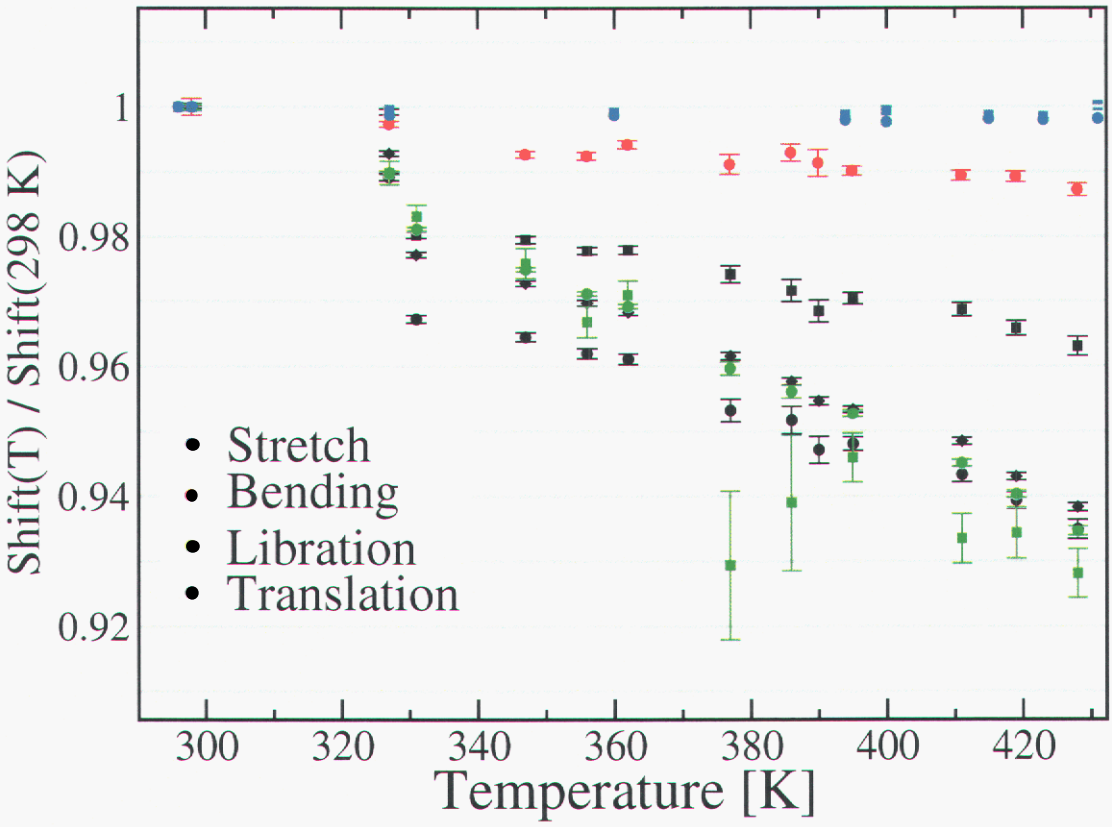

Figure 3.5: Fitted values for the vibrational modes as a function of temperature. The modes are color-coded for each of the groups: translation (black), libration (green), bending (red), and stretching (blue). The bending and stretching modes of the AlH_4^- anion shift less than 2 % from their room temperature values at the melting point of the compound.

The data indicate that the Al-H bending and stretching modes are not softening nearly to the extent observed for the libration and translational modes. Figure 3.5 shows the shifts of fitted peak positions as a function of temperature. In cases where the modes overlapped, such as the A_g and B_g modes at about 1773 cm^{-1}, the peaks observed were fitted to a single pseudo-Voigt profile. The E_g libration modes were difficult to fit and resulted in large error bars; however, their shifting to lower

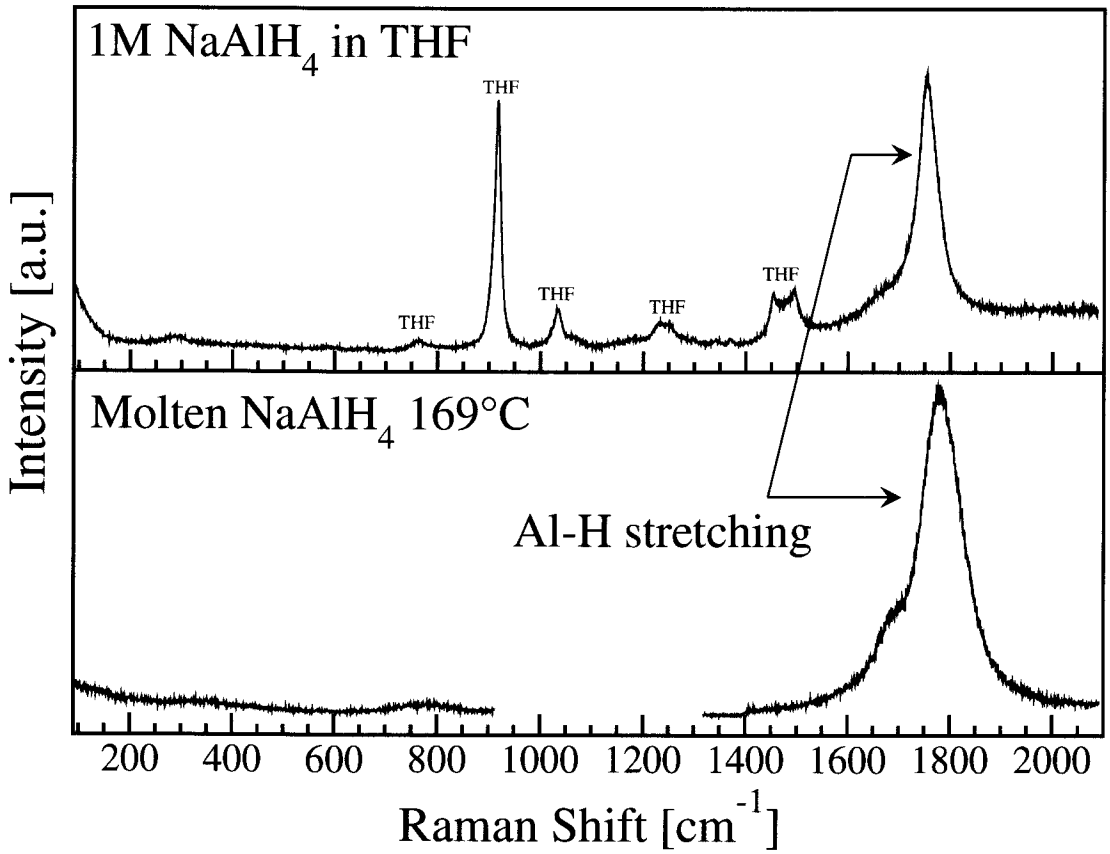

Figure 3.6: The bottom panel is Raman spectra of the surface melt of $NaAlH_4$ at 169°C. The apparent melting temperature of the crystal was 161°C. The AlH_4^- anion is still clearly intact, indicating that the molecular unit is stable in the melt, where the loss of crystal periodicity destroys the translational and librational modes. The top panel illustrates vibrations of the AlH_4^- anion in a 1 M solution of $NaAlH_4$ in tetrahydrofuran (THF) for reference.

wavenumber with temperature increase is clearly visible in Figure 3.3. Note that the Al-H bending and stretching modes shift less than 2 % from their room temperature values up to the melting point of $NaAlH_4$. This suggests that the AlH_4^- anion is a stable structure up to the melting point. In fact, slightly below about 161°C, the Raman modes associated with the crystal lattice completely disappeared while the AlH_4^- anion modes persisted, as shown in Figure 3.6. This observation establishes that AlH_4^- persists as a stable molecular species even after the $NaAlH_4$ lattice is lost.

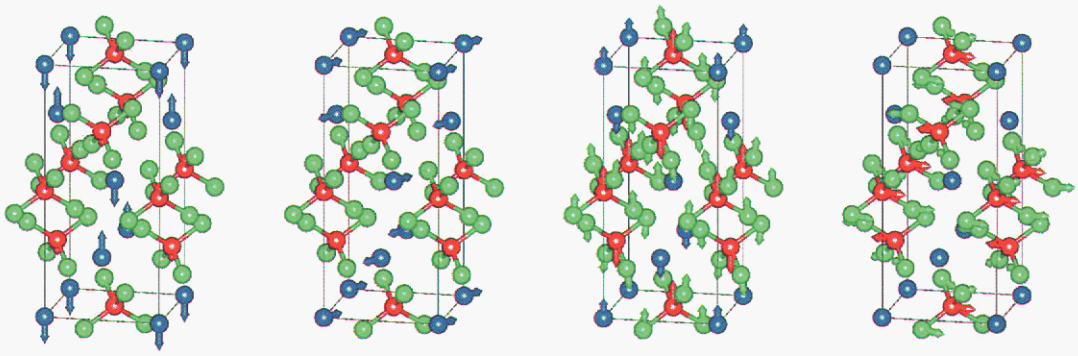

B_g 101 cm^{-1} E_g 116 cm^{-1} B_g 182 cm^{-1} E_g 191 cm^{-1}

Figure 3.7: Translational modes in $NaAlH_4$. Red (Al) atoms are tetrahedrally coordinated with green (H) atoms.

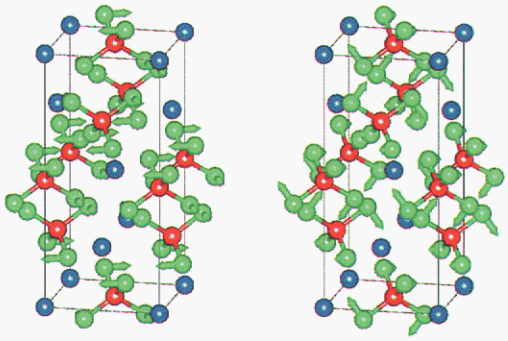

A_g 458 cm^{-1} E_g 560 cm^{-1}

Figure 3.8: Librational modes in $NaAlH_4$.

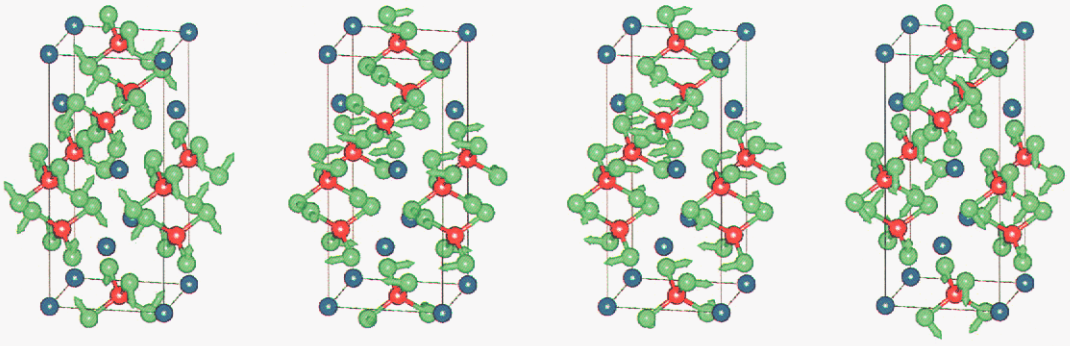

A_g 748 cm^{-1} B_g 797 cm^{-1} E_g 817 cm^{-1} B_g 850 cm^{-1}

Figure 3.9: Al-H bending modes in $NaAlH_4$.

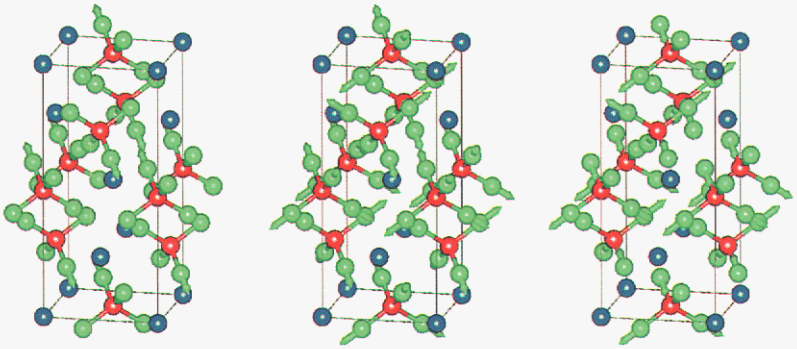

E_g1649 cm^{-1} A_g1726 cm^{-1} B_g1673 cm^{-1}

Figure 3.10: Al-H stretching modes in $NaAlH_4$.

3.3.3 Results of *ab initio* calculations

The calculated phonon frequencies using the LDA and GGA are given in Table 3.1, and the corresponding eigenvectors are shown in Figs. 3.7 to 3.10 below. Each set of phonon frequencies was calculated at the static equilibrium lattice parameters predicted by the LDA and GGA, respectively. Since the latter are several per cent smaller that the experimental values, the calculated LDA frequencies are expected to be somewhat higher than the experimental values, a well-known problem of the LDA which also manifests itself in Table 3.1. Overall, the quantitative agreement between the GGA frequencies and the experimental Raman data is better, but far from perfect. We attribute this to the neglect of thermal expansion and zero-point vibrations in the calculated equilibrium structural properties, as discussed below.

It is evident from Figs. 3.7–3.10 that the separation into four phonon mode groups, translational, librational, Al-H bending and Al-H stretching, is indeed justified. Of particular interest are the former two, since they correspond to low-energy vibrations that were found to exhibit considerable softening upon approaching the melting point. All translational modes in Fig. 3.7 correspond to simple motions of Na ions and AlH_4 groups relative to each other. The librational modes, shown in Fig. 3.8, exhibit rigid rotations of the AlH_4^{-1} tetrahedra along the axis that are either parallel to the tetragonal c direction (A_g mode) or lie within the (xy) plane (E_g mode). The dramatic softening of the translational and librational modes near the melting point, and the absence of any noticeable softening in the Al-H bending and stretching modes shown in Figs. 3.9 and 3.10, point to a melting mechanism where AlH_4^{-1} remains as a stable structural unit up to and beyond T_m. Since any reaction path for dissociating the AlH_4^{-1} unit must necessarily involve a linear combination of the Al-H bending and stretching modes, it is natural to hypothesize that breaking up (or rebuilding) the AlH_4^{-1} units is the reaction bottleneck for hydrogen release (absorption) in $NaAlH_4$. As argued in the following section, the role of Ti catalyst could be to facilitate the break-up of AlH_4^{-1} units and to reform some of them as AlH_6, as required by the two-step reactions Eqs. (3.1) and (3.2).

The calculated dielectric properties are given in Table 3.2. The Born effective charges indicate that $NaAlH_4$ is a highly ionic compound where the Na atoms are completely stripped of their valence electrons, and Al atoms partially so. This further supports the analysis of the bonding charge distribution and electronic band structure presented in Ref. [1], where the Al-H bond was characterized as polar covalent. The calculated anisotropy of the dielectric tensor $\epsilon^{\infty}_{\alpha\beta}$ is mild, which is again consistent with the relatively isotropic shape of the band structure of this compound.

The calculated phonon mode Grüneisen parameters, listed in Table 3.1, show that the low-energy translational and librational modes indeed soften most upon lattice expansion, as expected. In contrast, the Al-H bending and stretching mode Grüneisen parameters are much smaller, indicating that the bonding within the AlH_4^{-1} unit is relatively unaffected by lattice expansion. Furthermore, the magni-

Table 3.2: Born effective charges and dielectric constants for $NaAlH_4$ calculated using the DFT linear response and LDA. Tensors are given in a Cartesian coordinate system where the z axis is pointed along the tetragonal c-direction, Na ion is at $(0, \frac{1}{4}, \frac{1}{8})$, Al ion is at $(\frac{1}{2}, \frac{3}{4}, \frac{1}{8})$, and H ion is at $(0.763, 0.597, 0.460)$ in fractional coordinates.

$$Z_{\alpha\beta}(\mathrm{Na}) \quad \begin{pmatrix} +1.16 & -0.03 & 0 \\ +0.03 & +1.16 & 0 \\ 0 & 0 & +1.04 \end{pmatrix}$$

$$Z_{\alpha\beta}(\mathrm{Al}) \quad \begin{pmatrix} +1.67 & +0.02 & 0 \\ -0.02 & +1.67 & 0 \\ 0 & 0 & +2.12 \end{pmatrix}$$

$$Z_{\alpha\beta}(\mathrm{H}) \quad \begin{pmatrix} -0.73 & -0.05 & +0.06 \\ -0.05 & -0.68 & +0.14 \\ +0.08 & +0.09 & -0.79 \end{pmatrix}$$

ϵ^0_{xx}	10.1
ϵ^0_{zz}	9.2
ϵ^∞_{xx}	3.5
ϵ^∞_{zz}	3.7

tude of the calculated Grüneisen parameters suggests that the observed frequencies would decrease by approximately 1% for each 1% change in the lattice parameter. Using our calculated estimate of the lattice thermal expansion, shown in Fig. 3.11, this would account for only an $\approx$ 0.5% decrease in phonon frequencies over the temperature interval shown in Fig. 3.5. Only the softening of the Al-H bending and stretching modes is consistent with this estimate, while the frequencies of the translational and librational modes show much more dramatic decrease. Therefore, we conclude that the large softening observed in the *in situ* experiment should be attributed to intrinsic anharmonic effects caused by large-amplitude vibrations near the melting point.

When studying compounds with many light atoms per formula unit, it is important to understand the effects of vibrations on the structural properties. This especially intriguing in the light of the results of available theoretical calculations,[1] which have found that the discrepancies between the calculated and experimentally measured lattice parameters are unusually large (with GGA, the values of a and c were predicted to be 0.4 and 2.2% smaller, respectively[1]). We have calculated the effects of zero-point vibrations and thermal expansion as described in Sec. 3.2.2 using the LDA linear response method. We expect that the GGA would lead to insignificant changes in the calculated Grüneisen parameters and thermal expansion

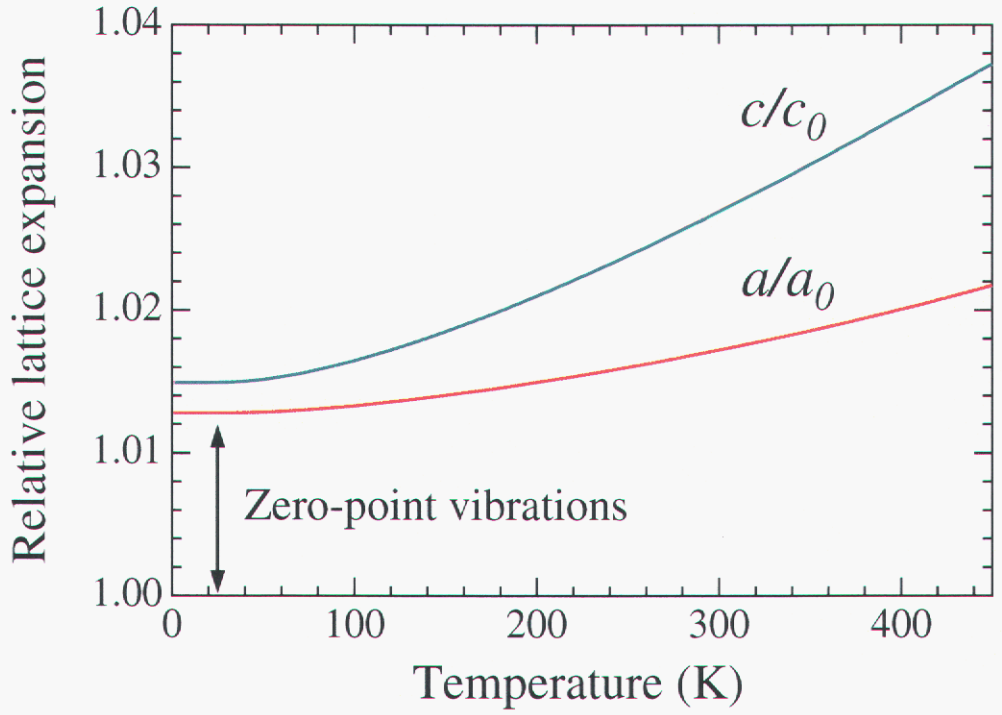

Figure 3.11: Calculated thermal expansion for $NaAlH_4$, expressed as a/a_0, where a_0 is the lattice parameter of a static non-vibrating lattice, neglecting zero-point motion.

coefficients. The results are shown in Fig. 3.11. The lattice parameters have been expressed as a/a_0 and c/c_0, where a_0 and c_0 are the equilibrium lattice parameters of a static nonvibrating lattice at $T = 0$ K, neglecting zero-point motion. It is evident that vibrations have a huge effect on the calculated lattice parameters, increasing the $T = 0$ K values by more than 1%, and changing the room-temperature values of a and c by 1.7 and 2.7%, respectively. The present results indicate that vibrational expansion removes the bulk of the discrepancy between the calculated GGA and measured room-temperature values of c (from 2.2% smaller to 0.7% smaller), although it should be noted that the agreement between the GGA and experimental numbers for the a parameter is actually worsened (it changes from 0.4% smaller to 0.8% larger). Finally, our predictions of the lattice thermal expansion between 300 and 450 K agree well with the x-ray data obtained on powdered samples by Gross *et al.*,[10] who found 0.2 and 1 % increases in the a and c parameters, respectively. These results have obvious implications for other complex hydrides with high hydrogen weight fractions, as the ionic zero-point vibrations are expected to result in sizable changes in the calculated lattice parameters. In fact, dynamical effects may account for most of the previously observed discrepancy between the theoretically calculated and experimentally measured lattice parameters.[1, 2] Since the simple quasiharmonic Grüneisen treatment seems to "over correct" the a parameter, it would be of great interest to apply a computational method with a more accurate theoretical treatment of the quantum nature of the proton. Such a study would allow to estimate the inherent accuracy of the approximate exchange-correlation functionals (LDA and GGA) for complex hydrides.

3.4 Discussion

The phonon modes of single crystal $NaAlH_4$ have been investigated. A full polarization analysis of the spectra unambiguously identifies nine of the 13 Raman active modes. The remaining four mode assignments are tentative. *In-situ* Raman spectra, taken up to the melting point of $NaAlH_4$, indicate significant softening of the translational and vibrational modes. The bending and stretching modes of the AlH_4^- anion are found to soften less than 1.5 %, and indicate that the anion is structurally and dynamically stable up to the melting temperature of the un-doped single crystal. These results suggest an obvious explanation for the very low rate of hydrogen release at temperatures below T_{melt} from un-doped bulk $NaAlH_4$. Since in a typical applications-oriented sample, doped with 4 at. % $TiCl_3$, the observed decomposition temperatures are roughly 80–90°C, or 0.75 T_{melt}, this suggests that the catalytic effect of Ti should involve an interaction with the AlH_4^- anion, and a weakening the Al-H bond strength, resulting in a breakup of the structural unit. Indications that substitutional Ti weakens the Al-H bond, have been offered by the calculations of Íñiguez *et al.*.[?] However, the exact location of catalycally active Ti atoms remains a controversial topic that requires furter study.[8, 5, 12, 28, 15, 1, 29]

Acknowledgments

This work was funded by the U.S. Department of Energy, Office of Energy Efficiency and Renewable Energy, in the Hydrogen, Fuel Cells & Infrastructure Technologies Program under contract No. DE-AC36-83CH10093, and Sandia National Laboratories through the Laboratory Directed Research and Development program. Data were fitted using *fityk* 0.4.2.

Bibliography

[1] V. Ozolins, E.H. Majzoub, and T.J. Udovic. Electronic structure and rietveld refinement parameters of ti-doped sodium alanates. *J. Al. Comp.*, 375:1 – 10, 7 2004.

[2] A. Aguayo and D. J. Singh. Electronic structure of the complex hydride $NaAlH_4$. *Phys. Rev. B*, 69:155103, 2004.

[3] B. Bogdanovic and M. Schwickardi. Ti-doped alkali metal aluminium hydrides as potential novel reversible hydrogen storage materials. *Journal of Alloys and Compounds*, 253-254(1-2):1 – 9, May 1997.

[4] B. Bogdanovic, R.A. Brand, A. Marjanovic, M. Schwickardi, and J. Tolle. Metal-doped sodium aluminium hydrides as potential new hydrogen storage materials. *J. Al. Comp.*, 302(1-2):36 – 58, April 2000.

[5] E.H. Majzoub and K.J. Gross. Titanium-halide catalyst-precursors in sodium aluminum hydrides. *Journal of Alloys and Compounds*, 356-357:363 – 7, August 2003.

[6] Finholt A.E., Barbaras G.D., Barbaras G.K., Urry G., Wartik G., and Schlesinger H.I. *J. Inorg. Nuc. Chem.*, 1(4-5):317 – 325, 1955.

[7] P. Claudy, B. Bonnetot, G. Chahine, and J. M. Letoffe. *Thermochimica Acta*, 38(1):75 – 88, 1980.

[8] G. Sandrock, K. Gross, and G. Thomas. *Journal of Alloys and Compounds*, 339:299 – 308, June 2002.

[9] K.J. Gross, G. Sandrock, and G.J. Thomas. Dynamic in situ x-ray diffraction of catalyzed alanates. *Journal of Alloys and Compounds*, 330-332:691 – 5, January 2002.

[10] K.J. Gross, S. Guthrie, S. Takara, and G. Thomas. In-situ x-ray diffraction study of the decomposition of $NaAlH_4$. *Journal of Alloys and Compounds*, 297(1-2):270 – 81, February 2000.

[11] Dalin Sun, T. Kiyobayashi, H.T. Takeshita, N. Kuriyama, and C.M. Jensen. X-ray diffraction studies of titanium and zirconium doped $NaAlH_4$: elucidation of doping induced structural changes and their relationship to enhanced hydrogen storage properties. *Journal of Alloys and Compounds*, 337:L8 – 11, May 2002.

[12] B. Bogdanovic, M. Felderhoff, M. Germann, M. Hartel, A. Pommerin, F. Schuth, C. Weidenthaler, and B. Zibrowius. *Journal of Alloys and Compounds*, 350:246 – 55, February 2003.

[13] A. Zaluska, L. Zaluski, and J.O. Strom-Olsen. Sodium alanates for reversible hydrogen storage. *Journal of Alloys and Compounds*, 298(1-2):125 – 34, February 2000.

[14] E.H. Majzoub, R.S. Stumpf, S. Spangler, J.L. Herberg, and Maxwell R.S. Compound formation in ti-doped sodium aluminum hydrides. Materials Research Society, December 2003.

[15] C. Weidenthaler, A. Pommerin, M. Felderhoff, B. Bogdanovic, and F. Schuth. On the state of the titanium and zirconium in ti- or zr-doped naalhsub 4 hydrogen storage material. *Physical Chemistry Chemical Physics*, 5(22):5149 – 53, 2003.

[16] J.-C. Bureau, J.-P. Bastide, B. Bonnetot, and H. Eddaoudi. Raman and infrared spectroscopy study of sodium tetrahydridoaluminate, naalh/sub 4/. *Materials Research Bulletin*, 20:93, 1985.

[17] P. Giannozzi, S. de Gironcoli, P. Pavone, and S. Baroni. *Ab initio* calculation of phonon dispersions in semiconductors. *Phys. Rev. B*, 43:7231, 1991.

[18] N. Troullier and J. L. Martins. Efficient pseudopotentials for plane-wave calculations. *Phys. Rev. B*, 43:1993, 1991.

[19] S. Louie, S. Froyen, and M. L. Cohen. *Phys. Rev. B*, 26:1738, 1982.

[20] G. Kresse and J. Hafner. *J. Phys.: Condens. Matt.*, 6:8245, 1994.

[21] G. Kresse and J. Hafner. *Phys. Rev. B*, 47:558, 1993.

[22] G. Kresse. PhD thesis, Technische Universität Wien, 1993.

[23] G. Kresse and J. Furthmüller. *Comput. Mater. Sci.*, 6:15, 1996.

[24] G. Kresse and J. Furthmüller. *Phys. Rev. B*, 54:11169, 1996.

[25] V.K. Bel'skii, B.M. Bulychev, and A.V. Golubeva. A redetermination of the structure of $naalh_4$. *Russ. J. Inorg. Chem.*, 28(10):1528, 1983.

[26] J.W. Lauher, D. Dougherty, and P.J. Herley. Sodium tetrahydroaluminate. *Acta Crystallographica, Section B (Structural Crystallography and Crystal Chemistry)*, B35(pt.6):1454 – 6, June 1979.

[27] W.G. Fateley. *Infrared and Raman selection rules for molecular and lattice vibrations: the correlation method.* Wiley-Interscience, 1972.

[28] J. Graetz, J. J. Reilly, J. Johnson, A. Y. Ignatov, and T. A. Tyson. X-ray absorption study of ti-activated sodium aluminum hydride. *Applied Physics Letters*, 85(3):500 – 2, JUL 2004.

[29] V. Ozolins. To be addressed in an upcoming publication.

This page intentionally left blank

Chapter 4

^{27}Al and ^{1}H MAS NMR and ^{27}Al Multiple Quantum Studies of Ti-doped $NaAlH_4$

Julie L. Herberg[11] , Robert S. Maxwell[1]
[1] Lawrence Livermore National Laboratories
Livermore, CA, 94551 USA

Eric H. Majzoub[2]
[2] Sandia National Laboratories
Livermore, CA, 94551 USA

Abstract

Previous X-ray Diffraction (XRD) and Nuclear Magnetic Resonance (NMR) studies on Ti-doped $NaAlH_4$ revealed the reaction products of two heavily doped (33.3 åt. %) samples. This investigation revealed that nano-crystalline or amorphous Al_2O_3 forms from the possible coordination of aluminum with the oxygen atom of the furan ring system from added tetrahydrofuran (THF) in solvent-mixed samples, and that $TiAl_3$ forms in mechanically-milled samples[1], indicating the importance of understanding the processing conditions of these potentially important hydrogen storage materials. The present paper provides a more sophisticated NMR investigation of the these materials and resolves some unanswered questions. On heavily doped (33.3 åt. %) *solvent-mixed* samples, ^{27}Al Magic Angle Spinning (MAS) NMR ^{27}Al multiple quantum MAS (MQMAS) indicates the presence of an oxide layer of Al_2O_3 on the surfaces of potentially bulk nanocrystalline Ti, nanocrystalline $TiAl_3$, and/or metallic aluminum. The ^{1}H MAS NMR data also indicate the possible coordination of aluminum with oxygen atoms in the THF molecules. In addition, the ^{1}H MAS NMR and ^{1}H spin-lattice relaxation (T_1) measurements are consistent with the presence of TiH_2. These results are in agreement with recent XAFS measure-

ments indicating both Al and H within the first few coordination shells of Ti in the doped alanate.

Keywords: Hydrogen storage; Ti-doped $NaAlH_4$; ^{27}Al MAS NMR; ^{27}Al MQMAS NMR

4.1 Introduction

The development of Ti-doped sodium aluminum hydrides has gained attention because of its large weight percentage of hydrogen (5.5% ideal) compared to interstitual hydrides. The kinetics of the absorption and desorption of H_2 improves dramatically by the addition of transition metal dopants, in the form of Ti-halides such as $TiCl_3$[1, 2]. However, the mechanism of enhanced kinetics due to the Ti-dopant in sodium aluminum hydride is still unknown.

Recently, we reported on Ti-doped sodium aluminum hydrides that were completely-reacted (33.3 åt. %-doped) with $TiCl_3$. These samples were processed in two different ways: one was solvent-mixed and the other was mechanically-milled[1]. The present paper explores the ^{27}Al and ^{1}H solid state NMR results of these fully-reacted samples in more complete detail. We do not address Ti-catalytic activity, but rather the importance of Ti-containing phases during material preparation. These reactions and the resultant products are crucial for understanding the conditions under which these materials can be most effectively doped for large scale applications. The ease of solution doping over mechanical milling is clear, however, the products of the doping process in THF, as presented in this paper, suggest that other solvents may be more suitable for large scale production.

In this paper, we performed ^{27}Al MAS NMR, ^{27}Al MQ MAS NMR, ^{1}H MAS NMR, and ^{1}H spin-lattice relaxation measurements (T_1) on fully-reacted samples that were either dissolved in THF or mechanically-milled. THF is known to coordinate strongly with transition metals in solution, and we show that this results in the formation of Al_2O_3 in heavily doped samples. Our results indicate that Al and H coordinate with the Ti in solution mixed samples, in agreement with recent XAFS studies on lightly doped (a few at. %) $NaAlH_4$ [3].

4.2 Experimental Details

4.2.1 Sample preparation

The samples prepared for this work are listed in Table (4.1). Millimeter sized crystals of $NaAlH_4$ were grown by solvent evaporation from *Sigma Aldrich* 1 M solutions of $NaAlH_4$ in THF, with $TiCl_3$ added to the solution at 4 at. %, with respect to the

Sample	Solution	Ti-precursor	at. % dopant	Form	Milled
S_2	THF	$TiCl_3$	4	crushed crystal	no
S_3	THF	$TiCl_3$	4	fine powder	no
S_4	THF	$TiCl_3$	33	fine powder	no
S_5	none	$TiCl_3$	33	fine powder	yes

Table 4.1: Samples used in this work.

amount of alanate in solution, before the solvent evaporation. The single crystal samples were subsequently crushed in a mortar and pestle for diffraction and NMR analysis. All samples were prepared in an argon glove box. These samples are referred to as (S_2). Rapidly dried 4 at. % doped samples, prepared in THF, resulted in fine powders and are referred to as (S_3). Some samples of (S_3) were also mechanically milled, and are referred to as (S_4). A further explanation of these samples is discussed elsewhere [1].

4.2.2 NMR Measurements

MAS NMR measurements were performed on a Bruker Avance 400WB spectrometer with a magnetic field of 9.4 T. This gives a resonance frequency of 104.25 MHz for ^{27}Al (spin $\frac{5}{2}$) and 400.13 MHz for ^{1}H (spin $\frac{1}{2}$). The samples were packed in 4 mm MAS rotors inside an Ar glove box with oxygen levels below 3 ppm. Spinning rates of 9 kHz and 12 kHz were used. The Free Induction Decay (FID) spectra were taken with a single excitation pulse. For ^{27}Al, a short pulse of 8 degree flip angle of 0.2 μs was used. ^{1}H MAS NMR was taken with a 90 degree pulse width of 4.2 μs. The ^{27}Al spectra were referenced to 0.1M aqueous solutions of $Al(NO_3)_3$ ar 0ppm and the ^{1}H NMR spectra were referenced to tetramethylsilane (TMS) at 0ppm.

The ^{1}H NMR spin-lattice relaxation times (T_1) were measured using a saturation-recovery method, as described by Fukushima[4]. The inspection of the partially recovered longitudinal magnatization was performed by using $\pi/2$(x)-τ-$\pi/2$(y) echo. The T_1 times were determined by fitting $M(\tau)/M_o$ to a multi-exponential growth curve: $(M(\tau)/M_o = \sum_{i=1}^{inf} X_i(1\text{-}exp(-\tau/T_1))$ [4].

^{27}Al MAS NMR resonances are typically broadened by non-negligible second order anisotropic effects[5]. Recent experimental methods, however, have been developed utilizing a combination of MAS and Multiple Quantum evolution which serve to provide high resolution spectra of I=5/2 spins [6]. For the ^{27}Al Multiple Quantum MAS (MQMAS) experiments, a standard two pulse z-filtered pulse sequence was used [7]. The non-selective 148 kHz $\pi/2$ pulse length was 1.75 μs at the power levels used. The conversion pulse was optimized at 2.5 μs and the reconversion pulse optimized to 0.8 μs. The z-filter pulse was 20 μs after the reconversion pulse and was set to 50 μs with 30 dB of additional attenuation on the RF power level. Data was acquired and processed using the states method and the data was shear transformed

in the indirect dimension according to Massiot, et al[7, 8]. The resonance frequency was set to the frequency of $Al(H_20)^{3+}$ (0ppm). The quadrupolar coupling parameters, which include second order quadrupolar effects (SOQE = $C_Q(1+\eta^2/3)^{1/2}$, where C_Q is the quadrupolar coupling constant and η is the asymmetry parameter) and isotropic chemical shifts (δ_{iso}) have been estimated from analysis of the resonance position in the unsheared spectra [9]. C_Q and η were then estimated by fitting the anisotropic line shapes with the DMFIT program[10].

4.3 Results and Discussion

Previous work[1] concluded that Rietveld refinement using powder X-ray diffraction of 4 at. % Ti-doped $NaAlH_4$ shows no observable shift in the lattice constants due to the exposure of Ti, indicating that the Ti does not enter the bulk of the $NaAlH_4$ lattice. A large dopant level was used (33 at. %) in order to fully react the $NaAlH_4$ and yield large amounts of reaction products. These fully-reacted samples would theoretically result in the formation of NaCl, $TiAl_3$, and/or TiH_2, and bulk Al. The fully-reacted (33 at. %-doped) sample that was solvent-mixed with THF (S_4) showed no evidence of bulk Ti or $TiAl_3$ in X-ray diffraction. Further, ^{23}Na MAS NMR studies on this same material confirmed that all of the ^{23}Na in this sample was in the form of NaCl, indicating that the sample was fully-reacted. The present paper determines the nature of the Al-O coordination in solution doped samples.

The ^{27}Al MAS spectrum is shown in Figure (4.1). The ^{27}Al MAS spectrum for this sample shows a peak at 1641 ppm, which represents metallic aluminum, and three overlapping peaks at 8.4 ppm, 35.5 ppm, and 63.6 ppm, which represents six, five, and four coordinate aluminum-oxygen species [11]. To determine that the three overlapping peaks did not represent AlH_4 species, ^{27}Al $\{^1H\}$ MAS NMR was performed. If AlH_4 species were responsible for these resonances, the resulting ^{27}Al NMR spectra would be expected to be broadened significantly due to large Al-H dipole-dipole couplings. This broadening, however, should be removed upon the application of ^1H decoupling during acquisition. In the samples studies here no significant narrowing occurred upon decoupling in the ^{27}Al NMR spectra, strongly indicating that these resonances are due to Al_2O_3 peaks and not to AlH_4.

To gain further insight into the speciation of the ^{27}Al peaks observed in the 0-100 ppm range, we performed a ^{27}Al MQMAS experiment on this sample. The sheared ^{27}Al MQMAS data is shown in Figure (4.2) with the horizontal axis representing the anisotropic dimension and the vertical axis representing the isotropic dimension. Three isotropic resonances were observed with broad anisotropic projections shown in the inset. The 2D lineshapes were not observed to smear as expected when distributions of chemical shift anisotropies of quadupolar coupling exist [12]. The anisotropic projections are all parallel with the horizontal axis and are consistent, within the uncertainty determined by the moderate signal-to-noise, with second order dominated MAS spectra without large distributions of chemical

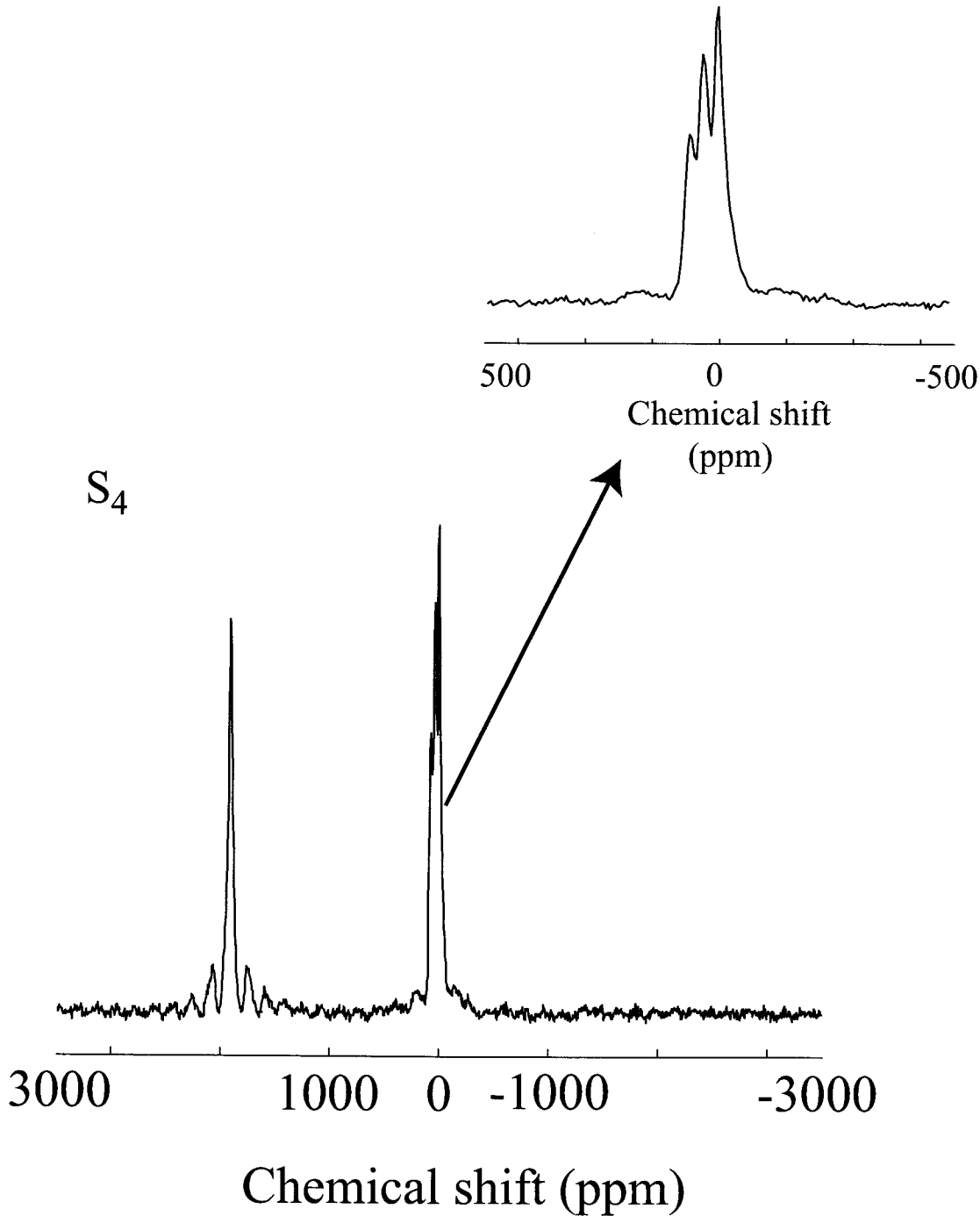

Figure 4.1: ^{27}Al MAS NMR spectra of $3NaAlH_4 + TiCl_3$ that was solution-mixed with THF (S_4). The data was taken with a 8 degree pulse width of 0.2μs and spinning at 12kHz. (Note: This data was previously published elsewhere [1].

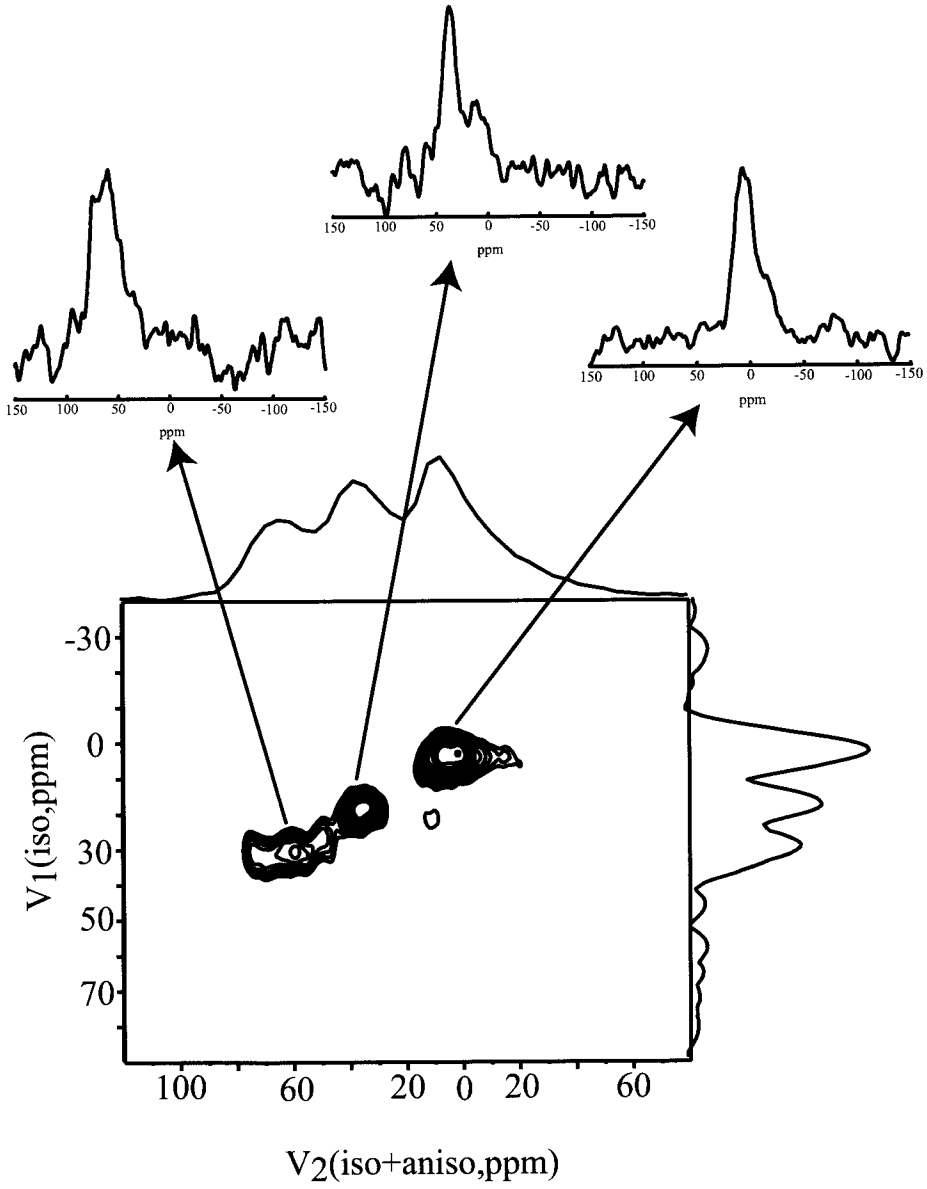

Figure 4.2: The ^{27}Al MQMAS data was taken with a spinning speed of 12kHz on sample S_4. The sheared ^{27}Al MQMAS data is a two-dimensional fourier transform plot of a triple/single-quantum correlation to highlight the isotropic and anisotropic nature of the ^{27}Al nuclei in this material. In this plot, the horizontal dimension represents single quantum coherence or isotropic and anisotropic coherence. The verticle dimension represents multiple quantum dimension and only contains information about isotropic coherences. The quadrupolar shifts for each peak are also presented.

shifts or quadrupole coupling constants. Increased signal to noise spectra were not possible given the reactive nature of these samples with oxygen.

The quadrupolar coupling parameters, which include SOQE, δ_{iso}, C_Q, and η, have been estimated from analysis of the resonance position in the unsheared spectra and fitting in the projections in frequency are shown in Table (4.2) [9]. The quadrupolar coupling parameters are in agreement with other reported values for Al_2O_3 [13, 12].

Species	Chemical Shift(ppm)	SOQE(MHz)	δ_{iso}(ppm)	C_Q(Mhz)	η
Al_2O_3(four-fold)	8.4	5.0	9.4	4.9	0.33
Al_2O_3(five-fold)	35.5	7.6	35.1	7.5	0.20
Al_2O_3(six-fold)	63.6	7.1	66	6.8	0.52

Table 4.2: The quadrupolar coupling parameters, which include second order quadrupolar effects (SOQE = $C_Q(1+\eta^2/3)^{1/2}$, where C_Q is the quadrupolar coupling constant and η is the asymmetry parameter) and isotropic chemical shifts (δ_{iso}) for the Al_2O_3 species determined from the unsheared ^{27}Al 3QMAS NMR spectra.

From the anisotropic chemical shifts and these coupling parameters, we have assigned the resonances in the 100-0 ppm range to 1) octahedral (0 to 10 ppm), 2) pentacoordinate (around 30 ppm), and 3) tetrahedral (40 to 80 ppm) Al-oxide sites[11]. The quadrupolar coupling constants and the fact that there exists no smearing in the ^{27}Al MQMAS data indicate that this system is rather ordered in nature. However, the X-ray Diffraction data shows no evidence of crystalline Al_2O_3. In the X-ray Diffraction data there is evidence of an extremely broad peak that could be attributed to material with a coherence length about 7-10 Å, which is mostly likely due to nanocrystalline Ti and/or $AlTi_3$. Even though the form of the nanocrystalline titanium is unknown, the picture of Ti, $AlTi_3$, and/or metallic aluminum in the bulk with a surrounding layer of amorphous Al_2O_3 on the surface is consistent with the ^{27}Al MQMAS NMR data. This would mean that the rather sharp peaks in the ^{27}Al MQMAS data of the different Al_2O_3 species represent amorphous Al_2O_3. On similar materials, others[14, 15] have found that the presence of pentacoordinate Al_2O_3 in ^{27}Al MQMAS data possibly represents amorphous Al_2O_3, rather than crystalline Al_2O_3 [15]. This conclusion is still widely debated. However, in this case, both the X-ray Diffraction data and the sharp, isotropic peaks of the different forms of Al_2O_3 in the ^{27}Al MQMAS NMR spectrum on the solvent-mixed sample strongly indicate that the ^{27}Al NMR signal arises from nano-crystalline Al_2O_3. The presence of Al_2O_3 in this sample (S_4) indicates the presence of oxygen, which could either come from contamination of the sample during processing, dissociation of THF to produce oxygen that are attached to the aluminum in the form of Al_2O_3, or the coordination of the oxygen atom on the furan ring in THF resulting in a reorientation of the aluminum atoms with the oxygen atom to form Al_2O_3.

Contamination seems unlikely. If contamination occurred, then one would expect to see the same type of contamination in the sample that was ball-milled (S_5) because the authors were careful to treat both these samples in the same manner. In the ^{1}H NMR spectra of sample S_5, there is no evidence of contamination in this sample. This is discussed further in a later section of this paper.

As for the second possibility, THF is one of the most polar ethers and is extremely soluble in water. It is not considered to be readily degradable. For this reason, THF is used as a solvent for polar reagents. However, THF has been known to decompose when exposed to a catalyst, such as organolithiums [16]. Thus, it is not out of the question that this might occur. The possible decomposition products of THF would be CH_2 and OH groups, but to speculate on the ^{1}H NMR chemical shift of these signatures in the presence of titanium is rather difficult and beyond the scope of this paper. We also attempted to perform ^{13}C NMR on this sample, but we were unable to obtain a signal because of the small amount of carbon in this system. The most likely senario of the origin of the oxygen in Al_2O_3 would be the coordination of aluminum on internal surfaces of the metallic aluminum coordinated with oxygen atoms of the heteroatomic furan ring in THF. This same senario has been seen in other metal systems, including aluminum, lithium, and magnesium, where the strong ionic metal-oxygen bond can lead to an sp^2-type lone pair orbital, which can act as a dative bond to a metal center [17, 18]. This possiblity was also predicted by Fichtner et al [19]. From the ^{1}H MAS NMR data, which is shown in Figure (4.3), the origin of the oxygen in the Al_2O_3 cannot be fully determined. However, the ^{1}H MAS NMR data can provide insight into the structure of the protons in sample S_4 that was solvent mixed. THF typically gives signal at 1.72 ppm and 3.58 ppm for ^{1}H MAS NMR spectra[20]. From the ^{1}H MAS NMR spectrum on sample (S_4), the ^{1}H MAS NMR peaks occur at 1.7 ppm, 4.8 ppm, and 8.7 ppm. From a paper examining how THF impacts clathrate hydrates for hydrogen storage, Lee et al.[21] found that they could distinguish between H_2O, H_2 in small cages, H_2 in large cages, and THF through both ^{1}H MAS NMR and Raman Scattering. By comparing these authors' ^{1}H MAS NMR results with our results, we can conclude that ^{1}H NMR peak at 1.7 ppm represents aliphatic protons in the THF that are weakly interacting with the oxygen in THF, the ^{1}H NMR peak at 4.8 ppm represents H_2 in small cages in interstitual sites, and ^{1}H NMR peak at 8.2 ppm most likely represents H_2O. The question here is what happens to the ^{1}H NMR THF peak at 3.58 ppm, which represents the aliphatic protons in the THF that are strongly interacting with the oxygen in THF. It is possible that the location of the ^{1}H NMR THF peak at 3.58 ppm is embedded in the wide linewidth of the ^{1}H MAS NMR peak at 4.8 ppm. If the oxygen from THF is coordinated with the aluminum to form Al_2O_3, then one would expect the ^{1}H NMR THF peak at 3.58 ppm to be slightly shifted, but within the wide linewidth of the ^{1}H MAS NMR peak at 4.8 ppm. This makes the scenario of the origin of the oxygen in Al_2O_3 signal that would occur from the coordination of aluminum with THF highly probable.

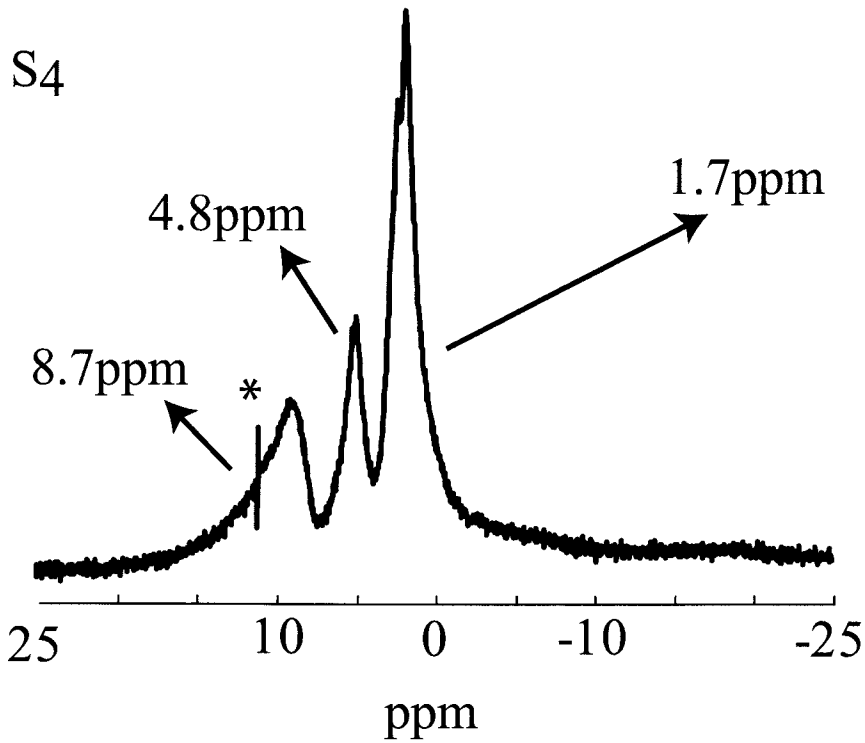

Figure 4.3: ^{1}H MAS NMR spectra of $3NaAlH_4 + TiCl_3$ that was solution-mixed with THF (S_4). The data was taken with a spinning at 12kHz. * indicates an offset signal.

Even though both XRD and NMR showed no evidence of $TiAl_3$ in the sample S_5, and only the presence of metallic aluminum and Al_2O_3, the ^{27}Al MAS NMR data on the mechanically-milled sample (S_5) did show evidence of $TiAl_3$, as shown in Figure (4.4a). There are four resonances: two at approximately 10 ppm and 103 ppm, with respective linewidths of 19 ppm and 30 ppm, a broad resonance at approximately 664 ppm, and a small amount of metallic aluminum at 1640 ppm. Our previous studies compared this signal with a sample of pure $TiAl_3$ in the $L1_2$ metabstable structure. This suggested the existence of $TiAl_3$ in the mechanically-milled sample (S_5)[1]. As indicated by others investigating similar materials[22], a full understanding of the aluminum species in this material is not straight forward. The metallic aluminum signal in the ^{27}Al MAS NMR data on sample (S_5) occurs at 1640 ppm, which is extremely small integrated intensity due to the excitation bandwidth limitations. Most likely, this sample has only a small amount of metallic aluminum. Balema et al. [23] have found that $TiAl_3$ is present in mechanically-milled Ti-doped $LiAlH_4$. Through XRD and ^{27}Al NMR, these authors showed that the ball-milling process leads to transformation of the $TiAl_3$ from a DO_{22} phase into a metastable phase $L1_2$. Quadrupolar interactions, Knight shifts, and spin-lattice relaxation times in $TiAl_3$ can provide information about site occupation and Fermi-surface effects. Since quadrupolar and anisotropic Knight shift effects typically complicates the central transition ($\frac{1}{2} \rightarrow -\frac{1}{2}$), the satellite transitions that are due to quadrupolar broadening from high order transitions can provide further insight into this material. From Figure (4.4) b), which is a ^{27}Al static NMR spectrum of sample S_5; it is apparent that some satellite transitions are present, but to gather further information from this spectrum would be difficult due to the poor signal-to-noise. However, the observed $TiAl_3$ is paramagnetically shifted, which means that paramagetic shielding adds to the overall magnetic field experienced by the nucleus. This is similar to other static ^{27}Al NMR data[24].

While $TiAl_3$ is present in the fully-reacted mechanically milled sample (S_5), the location of the residual hydrogen in this material (indicated by ^1H NMR) is still unknown. For this sample (S_5), the ^1H MAS NMR lineshape is shown in Figure (4.5) is extremely broad. From other studies on Ti-Al-H alloys [25], it has been shown that hydrogen in the form of TiH_2 produces a broad ^1H NMR lineshape. These authors also showed that samples that were contaminated with oxygen and carbon produced a narrow ^1H NMR lineshape superimposed on a broad ^1H NMR lineshape. Therefore, the broad nature of the ^{1} NMR lineshape of sample S_5 is consistent with the presence of TiH_2. The ^1H NMR spin-lattice relaxation (T_1) measurements of samples S_2, S_3, S_4, and S_5 are shown in Figure (4.6). In sample (S_2), which is likely pure $NaAlH_4$, there is only one long T_1 relaxation process. Sample (S_3) also shows only one T_1 relaxation process. However, in samples (S_4) and (S_5) there is likely more than one relaxation process, perhaps indicating that there are three different local environments for the fully-reacted samples. The T_1 values are shown in Table (4.3). These results are similar to Korn et al.[25], who showed through

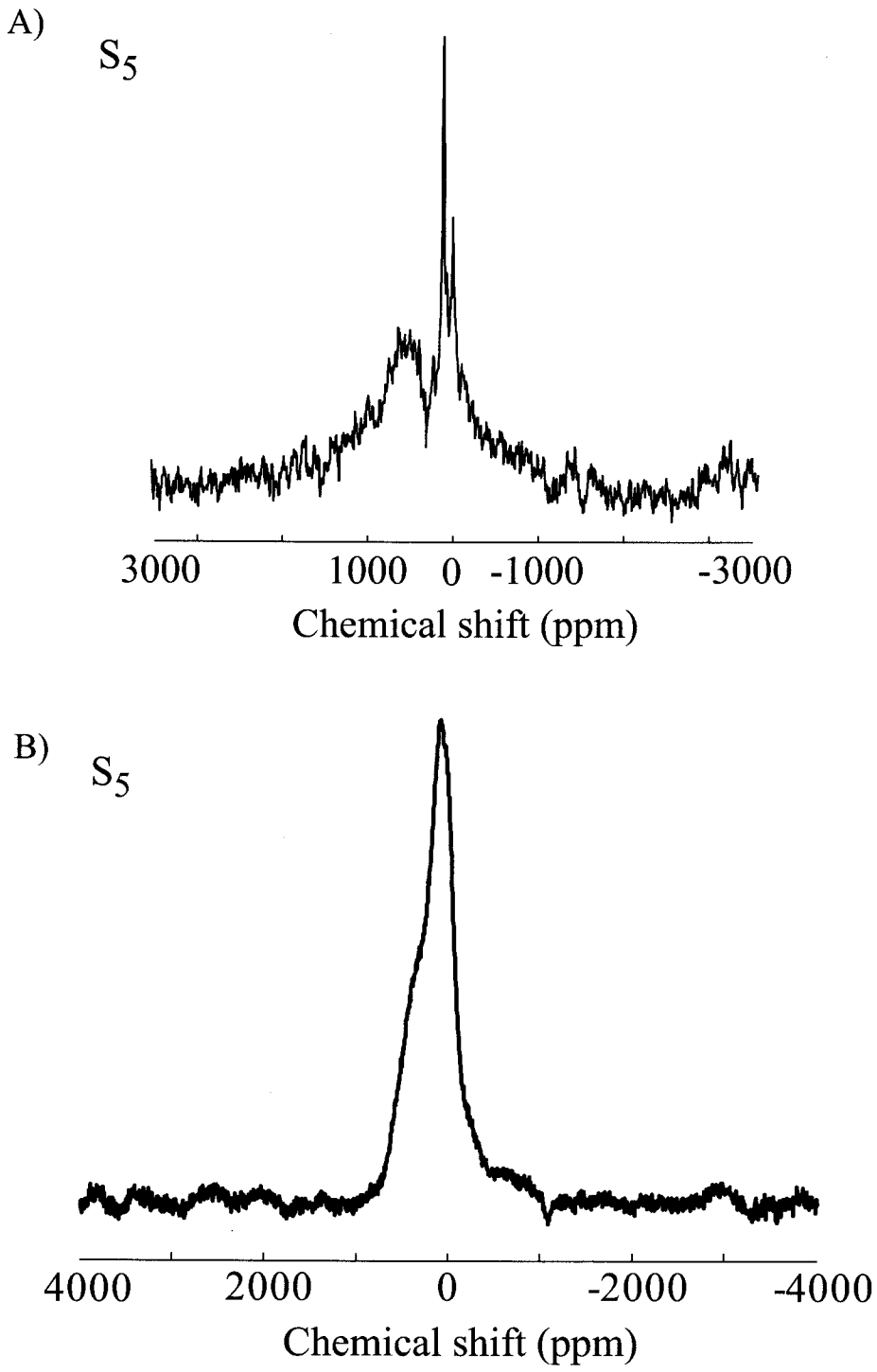

Figure 4.4: ^{27}Al MAS NMR spectra of $3NaAlH_4$ + $TiCl_3$ that was mecannically-milled (S_5). The data was taken with a 8 degree pulse width of 0.2μs. a) spinning at 12kHz (Note: This data was previously published elsewhere. [1]) b) static.

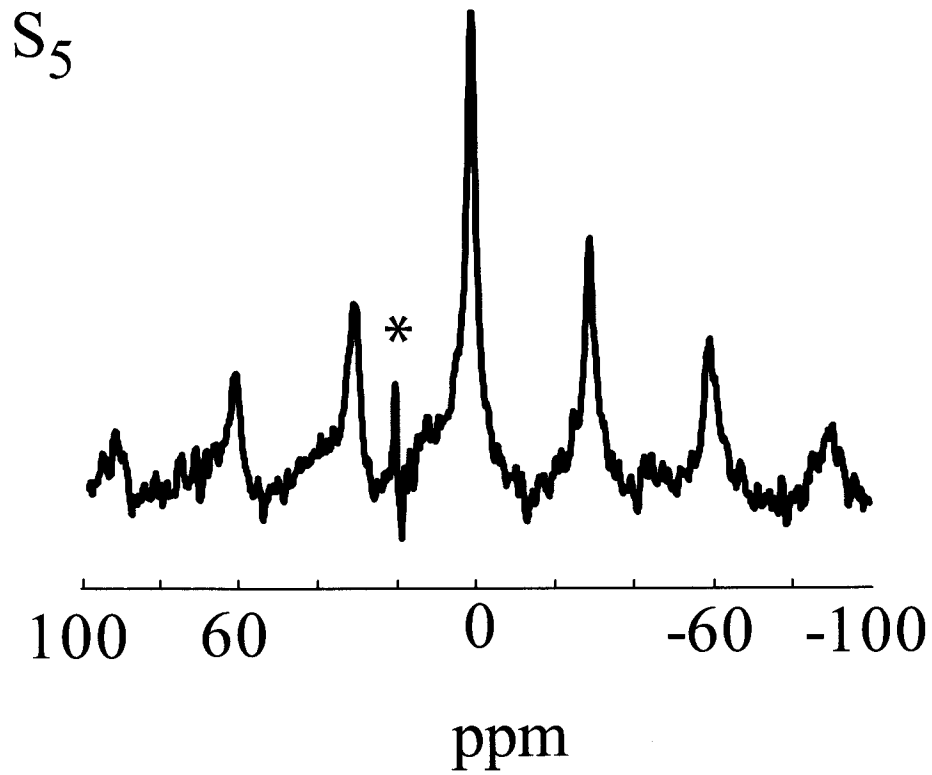

Figure 4.5: ^{1}H MAS NMR spectra of $3NaAlH_4$ + $TiCl_3$ that was mechanically milled(S_5). The data was taken with a spinning at speeds of 12kHz. * indicates an offset signal.

Sample	S_2	S_3	S_4	S_5
$T_{1(1)}$	1.036s	1.935s	1.3036s	2.257s
$T_{1(2)}$			0.246s	0.246s
$T_{1(3)}$			0.009s	0.0401s

Table 4.3: The ^{1}H NMR spin-lattice relaxation (T_1) times for $NaAlH_4$ Ti-doped in different processes.

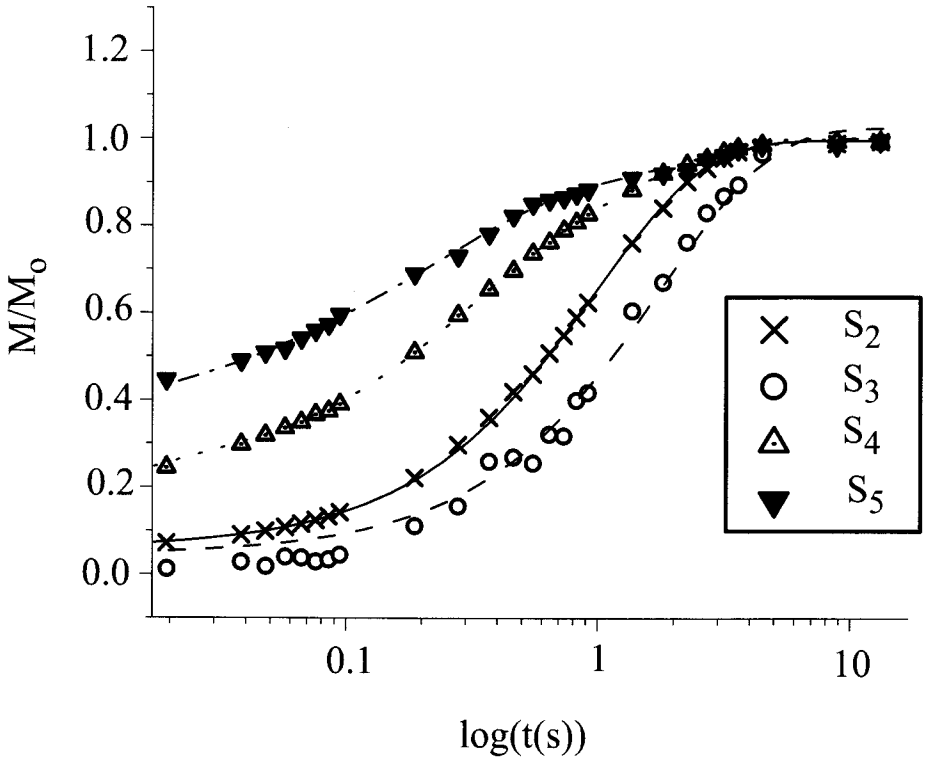

Figure 4.6: ^{1}H spin-lattice relaxation measurements (T_1) of sample S_2, S_3, S_4, and S_5.

^{1}H T_1 NMR measurements that hydrogen in a Ti-Al-H system has at least three different crystallographic environments with different diffusion characteristics. Korn et al. found that one of the T_1 processes would likely be due to TiH_2, which would possess a fast T_1 relaxation rate, since the hydrogen is in contact with the titanium. In fact, Korn et al. indicate a T_1 relaxation time for TiH_2 in the presence of 16.3 at. %of aluminum to be approximately 30-40 ms at room temperature, which is close to the fast T_1 relaxation time of 40.1 ms for S_5. Thus, this fast T_1 relaxation process clearly exists in samples (S_4) and (S_5), but the different hydrogen processes can be distinguished by their different relaxation times. Both the fully-reacted sample that was solvent-mixed (S_4) and the mechanically-milled sample (S_5) has one very fast relaxing ^{1}H NMR T_1 process. Since these samples were fully reacted, the possibility of a Ti-H-Al alloy is rather unlikely, while TiH_2 is likely to remain in these samples.

4.4 Conclusions

Our ^{27}Al MQMAS experiments indicate that fully-reacted THF solvent-mixed samples contain an oxide layer of Al_2O_3, potentially around bulk nanocrystalline Ti, nanocrystalline $TiAl_3$, and/or metallic aluminum. Examination of the ^{1}H MAS NMR data from this sample suggests that the source of oxygen in Al_2O_3 was likely due to the THF molecule being coordinated with aluminum in a Ti-Al compound or nanocluster. These results clearly indicate the extremely different compounds which may result in solvent mixed samples, as opposed to mechanically milled samples, where the ^{27}Al MAS and static NMR studies show the presence of $TiAl_3$. Finally, the ^{1}H MAS NMR and ^{1}H spin-lattice relaxation measurements (T_1) indicate the presence of TiH_2 in fully-reacted mechanically milled sample[26, 27].

Acknowledgements
The authors would like to thank Dr. Robert Bowman, Dr. Sarah C. Chinn, and Dr. Julie Perkins for their insights. This work was funded by the U.S. Department of Energy, Office of Energy Efficiency and Renewable Energy, in the Hydrogen, Fuel Cells & Infrastructure Technologies Program under contract No. DE-AC36-83CH10093, and Sandia National Laboratories through the Laboratory Directed Research and Development program. NMR work was performed under the auspices of the U.S. Department of Energy by University of California, Lawrence Livermore National Laboratory under Contract W-7405-Eng-48.

Bibliography

[1] E. H. Majzoub, J. L. Herberg, R. Stumpf, and R. S. Maxwell. Xrd and nmr investigation of ti-compound formation in solution-doping of sodium aluminum

hydrides: Solubility of ti in $naalh_4$ crystal grown in thf. *Journal of Alloys and Compounds*, 394:265, 2005.

[2] B. Bogdanovic, M. Felderhoff, M. Germann, M. Hartel, A. Pommerin, F. Schuth, C. Weidenthaler, and B. Zibrowius. Investigation of hydrogen discharging and recharging processes of ti-doped $naalh_4$ by x-ray diffraction analysis (xrd) and solid-state nmr spectroscopy. *Journal of Alloys and Compounds*, 350:246–255, 2003.

[3] J. Graetz, J. J. Reilly, J. Johnson, A. Yu. Ignatov, and T. A. Tyson. X-ray absorption study of ti-activated sodium aluminum hydride. *Applied Physics Letters*, 85:500, 2004.

[4] E. Fukushima and S. B. W. Roeder. *Experimental Pulse NMR: A Nuts and Bolts Approach.* Addison-Wesley Publishing Company, Inc., 1981.

[5] C. P. Slichter. *Principles of Nuclear Magnetic Resonance.* Springer-Verlag, 1990.

[6] A. Medek, J. S. Harwood, and L. Frydman. Multiple-quantum magic angle spinning nmr: A new method for study of quadrupolar nuclei in solids. *J. Am. Chem. Soc.*, 117:12779–12787, 1995.

[7] S. Ganapathy, T. K. Das, R. Vetrivel, S. S. Ray, T. Sen, S. Sivasanker, L. Delevoye, C. Fernandez, and J. P. Amoureux. Anisotropic chemical shielding, m-site ordering, and characterization of extraframework cations in ets-10 studied through mas/mq-mas nmr and molecular modeling techniques. *Journal of the American Chemical Society*, 120:4752–4762, 1998.

[8] D. Massiot, B. Touzo, D. Trumeau, J. P. Coutures, J. Virlet, P. Florian, and P. J. Grandinetti. Two-dimensional magic-angle spinning isotropic reconstruction sequences for quadrupolar nuclei. *Solid State Nuclear Magnetic Resonance*, 6:73–83, 1996.

[9] C. Fernandez, J. P. Amoureux, J. M. Chezeau, L. Delmotte, and H. Kessler. ^{27}al nmr characterization of $alpo_4$-14 enhanced resolution and information by mqmas[1] dr. hellmut g. karge on the occasion of his 65th birthday. *Microporous Materials*, 6:331–340, 1996.

[10] D. Massiot, F. Fayon, M. Capron, I. King, S. Le Calve, B. Alonso, J-O. Durand, B. Bujoli, Z. Gan, and G. Hoatson. Modelling one- and two-dimensional solid state nmr spectra. *Magnetic Resonance in Chemistry*, 40:70–76, 2002.

[11] C. J. Brinker and G. W. Scherer. *Sol-gel Science.* Academic Press, 1989.

[12] A. Goldbourt and S. Vega. Signal enhancement in 5qmas spectra of spin-5/2 quadrupolar nuclei. *Journal of Magnetic Resonance*, 154:280–286, 2002.

[13] H. Kraus, R. Prins, and A. P. M. Kentgens. A ^{27}al mqmas and off-resonance nutation nmr investigation of mo-p/γ-al_2o_3 hydrotreateing catalyst precursors. *J. Phys. Chem.*, 100:16336–16345, 1996.

[14] P. Florian, M. Gervais, A. Douy, D. Massiot, and J. P. Coutures. A multi-nuclear multi-field nuclear magnetic resonance study of the y_2o_3-al_2o_3 phase diagram. *J. Phys. Chem. B.*, 105:379–391, 2001.

[15] J. McManus, S. E. Ashbrook, K. J. D. MacKenzie, and S. Wimperis. ^{27}al multiple-quantum mas and ^{27}al ^{1}H cpmas nmr study of amorphous aluminosilicates. *Journal of Non-Crystalline Solids*, 282:278–290, 2000.

[16] J. Clayden and S. A. Yasin. Pathways for decomposition of thf by organolithiums: the role of hmpa. *New. J. Chem.*, 26:191–192, 2002.

[17] H. Sachdev, C. Wagner, C. Preis, V. Huch, and M. Veith. Coordination chemistry of fufurylsilylamides. *J. Chem. Soc. Dalton Trans.*, pages 4709–4713, 2002.

[18] Y.K. Gun'ko, R. Reilly, and V.G. Kessler. A convenient route to anionic and cyclic aluminosiloxanes: crystal structure of [pyh][al$OSiPh_2(OSiPh_2)_2O_2$] and the first tweleve-membered organic aluminosilicate $al_2si_4o_6$ ring. *New J. Chem.*, 25:528–530, 2001.

[19] M. Fichtner, O. Fuhr, O. Kircher, and J. Rothe. Small ti clusters for catalysis of hydrogen exchange in $naalh_4$. *Nanotechnology*, 14:778–785, 2003.

[20] F. Deng, J. Hu, J. Xiong, and Y. Du. Solid-state nmr studies of ^{1}h spin diffusion in adsorbed organic molecules. *Solid State Nuclear Magnetic Resonance*, 2:97–103, 2003.

[21] H. Lee, J. Lee, D. Kim, J. Park, Y. Seo, H. Zeng, I.L. Moudrakovski, C. I. Ratcliffe, and J.A. Ripmeester. Tuning clathrae hydrates for hydrogen storage. *Nature*, 434:743–746, 2005.

[22] J. W. Weinch, V. P. Balema, V. K. Pecharsky, and M. Pruski. Solid-state ^{27}al nmr investigation of thermal decomposition of $lialh_4$. *Journal of Solid State Chemistry*, 177:648–653, 2004.

[23] V. P. Balema, J. W. Wiench, K. W. Dennis, M. Pruski, and V. K. Pecharsky. Titanium catalyzed solid-state transformations in $lialh_4$ during highenergy ball-milling. *Journal of Alloys and Compounds*, 329:108–114, 2001.

[24] C. Lue, S. Chepin, J. Chepin, and J. H. Ross. Nmr study of trialuminide intermetallic. *Physical Review B*, 57(12):33, 1998.

[25] C. Korn, D. Zamir, and Z. Hadari. Nmr study of the influence of aluminum alloying on the titanium-hydrogen system. *Acta Metallurgica*, 22:33–46, 1974.

[26] T. J. Bastow, C. T. Forwood, M. A. Gibson, and M. E. Smith. Local site symmetry and electronic structure of trialuminide and related intermetallic alloys probed by solid-state nmr. *Physical Review B*, 58:2988, 1998.

[27] M. A. Maeland, B. Hauback, H. Fjellvag, and M. Sorby. The structures of hydride phases in the ti_3al/h system. *International Journal of Hydrogen Energy*, 24:163–168, 1999.

This page intentionally left blank

Distribution

1	MS 9052	Anthony McDaniel, 8367
1	MS 9052	Jay Keller, 8367
1	MS 9161	Roland Stumpf, 8761
1	MS 9161	Doug Medlin, 8761
1	MS 9161	Konrad Thuermer, 8761
1	MS 9402	Bob Bastasz, 8772
1	MS 9403	Karl Gross, 8773
1	MS 9403	Jim Wang, 8773
1	MS 9403	Ewa Ronnebro, 8773
1	MS 9403	Weifang Luo, 8773
1	MS 9405	Bob Carling, 8700
1	MS 9409	Daniel Dedrick, 8775
1	MS 9409	Terry Johnson, 8775

2	MS 9018	Central Technical Files, 8945-1
2	MS 0899	Technical Library, 4536
1	MS 0188	D. Chavez, LDRD Office, 1011